ABSTRACT

Title of thesis: PREDICTING LOW PROBABILITY STREAMFLOW USING LIDAR DATA AND HYDRAULIC GEOMETRY

Javier I. Mardones, Master of Science, 2019

Thesis directed by: Professor Kaye L. Brubaker
Department of Civil & Environmental Engineering

Predicting stream flow is essential for safe and economic planning and design of hydraulic structures. This study uses the observed channel cross-section from LiDAR data and physical concepts of shear stress to estimate bankfull discharge (Q_{bf}). Assuming that Q_{bf} is the median of the annual peak flow distribution, a 2-parameter Extreme Value Type I distribution was fitted to predict discharge to a 200-year return period. The method was compared with gauged sites in low-order streams (less than 90-meter bankfull width) resulting in $SE/SY = 1.31$ for Q_{bf} and $SE/SY = 1.90$ for the 200-year return period discharge; model precision is poor. However, the relative bias (-15% to +15%) demonstrates that on average results are similar to gauged data. Relationships between flow and channel geometry assure a quick way to estimate stream data and can serve as a tool used prior to applying conventional hydrologic methods such as flow routing and regional regression equations.

PREDICTING LOW PROBABILITY STREAMFLOW USING LIDAR DATA AND HYDRAULIC GEOMETRY

by

Javier I. Mardones

Thesis submitted to the Faculty of the Graduate School of the
University of Maryland, College Park in partial fulfillment
of the requirements for the degree of
Master of Science
2019

Advisory Committee:
Professor Kaye L. Brubaker, Chair/Advisor
Professor Barton A. Forman
Professor Richard H. McCuen
Professor Karen L. Prestegaard

Acknowledgments

I owe my gratitude to all the people who have made this thesis possible. First and foremost I'd like to thank my advisor, Dr. Kaye Brubaker for giving me an invaluable opportunity to work on challenging and extremely interesting projects over the past two years. She has always made herself available for help and advice and there has never been an occasion when I've knocked on her door and she hasn't given me time.

I would also like to thank my co-advisor, Dr. Karen Prestegaard. Without her extraordinary theoretical ideas and expertise on the subject, this thesis would have been a distant goal. Thanks are due to Dr. Barton Forman and Professor Richard McCuen for agreeing to serve on my thesis committee and for sparing their invaluable time reviewing the manuscript.

I would also like to acknowledge help and support from the writing center, specially to Norine Walker who took her time to review my thesis.

I owe my deepest thanks to my wife who have always stood by me and guided me through my life and career, and have pulled me through against impossible odds at times. Words cannot express the gratitude I owe her.

Thanks y'all!

Table of Contents

List of Tables

List of Figures

List of Abbreviations

AHG	At a Station Hydraulic Geometry
AMHG	At Many Station Hydraulic Geometry
DEM	Digital Elevation Model
DSM	Digital Surface Model
EVTI	Generalized Extreme Value Type I distribution
GIS	Geographic Information System
HG	Hydraulic Geometry
HGM	Hydraulic Geometry Model
iMAP	Maryland's Mapping & GIS Data Portal
LiDAR	Light Detection and Ranging
NIR	Near-Infrared
NWIS	National Water Information System
Q-Q	Quantile-Quantile
US	United States (Country)
USGS	United States Geological Survey

Chapter 1

Introduction

Accurate stream discharge measurements are important for flood risk analysis and many other hydrological studies. Rivers act as a freshwater source for terrestrial life, yet the discharge is often poorly documented since the existing direct observations are inadequate and some observation stations have been interrupted or discontinued (Sichangi et al., 2016). In remote locations it is often difficult to obtain stream flow information because of the difficulty in making the discharge measurements necessary to define rating curves or stage-discharge relationships (Nathanson et al., 2012). For much of the world, river gauge measurements are rare, nonexistent, or proprietary. Even well monitored countries have sparsely distributed networks, thus limiting current understanding of water losses along river courses, habitat changes, and flood risk (Hunger and Döll, 2007; Stahl et al., 2012). This lack of knowledge represents an acute problem, given the possible acceleration of the water cycle due to global warming (Huntington, 2006).

1.1 Importance of a Rapid Estimation Method

There are several ways of predicting river discharge flow at ungauged sites, but those more frequently used consider the use of recurrence interval flow regression equations (watershed geometry) and flow routing (rainfall-runoff). The regression

equations (e.g., McCandless et al. (2003)), while reliable, also depend on geographic properties, making it difficult to reapply the same methodology or equations for different regions. Also, the equations must be updated frequently in order to keep track of recent rainfall events and climate change. Although the regression equation method can be applied very quickly, it is often desirable to be able to obtain an even more rapid estimate of the flood discharge of a particular frequency for a specific site. Rainfall-runoff modeling is difficult and relies on spatially distributed precipitation data, excellent characterization of the physical properties of the watershed and a model of the appropriate runoff processes; for larger watersheds it is actually a rainfall-runoff-routing problem (Beven and Beven, 2001). Therefore, rainfall-runoff modeling works best for calculation of overland flow runoff from simple surfaces in small basins (e.g. small urbanized areas). These hydrologic models are both time-consuming in data collection and often in computation resources (Wharton and Tomlinson, 1999)

Discharge is an integrative measure of the watershed response and rainfall data are usually point data, and runoff modeling requires detailed spatial data to provide accurate responses. Therefore, the use of independent data to estimate river discharge is unsettled from a geomorphologic point of view (e.g., runoff does not affect the amount of rainfall); precipitation and watershed characteristics define the shape of a river (there is not enough involvement the other way around). This results in a model where the output will be constant over the years unless there is a major change in the climate or catchment physiology.

An alternative method is to estimate discharge from dependent variables such

as bankfull properties and critical shear stress values. A model that uses only dependent data has the advantage of not using any roughness or rainfall data as an input. Since the physics and dynamics of the whole system are so complex and hard to track, some assumptions must be made to fully develop even the most reliable method for flow estimation.

Estimating flow using evidence of the last flood magnitudes, which gave shape to the stream, is based on the amount of sediment transported, which is expected to change after the next peak flood (Olsen et al., 1997). But, events of a catastrophic magnitude are rare and usually separated by a long interval of time, so that it is almost impossible for a single person to compare changes brought about by two such events at the same place and to generalize about their effects on the landscape (Gupta and Fox, 1974).

The Manning equation (Manning, 1891) or other similar expressions have been used for more than a century in modeling open channel flow. One often identified drawback of such approaches is their reliance on an empirical coefficient (here, the Manning coefficient) of roughness, which can vary with stream stage (Comiti et al., 2007; López et al., 2007).

The philosophy behind the hydraulic geometry method (HGM) proposed in this study is simple: "A 100-year rainfall does not necessarily cause a 100-year flood". Channel geometry equations that relate discharge to channel width or channel cross section are considered to be the most reliable (Bhatt and Tiwari, 2008). Furthermore, discharge estimates using both effective river width and stage information consistently outperform those using only stage data (Sichangi et al., 2016).

1.2 Goals and Objectives

The goal of this research is to predict low-probability discharge using only the information given by the river cross-section geometry and bed material. This study compares bankfull discharge values obtained from multi-year discharge records at gauged sites with computations of bankfull discharges from hydraulic geometry relations, and sediment transport threshold values. The bankfull discharge is then used as an input to estimate predictions of low probability flow (200-year recurrence interval or less) by applying an Extreme Value Type I (EVTI) distribution with parameters α and β from the method of moments. The study explores the possibility of predicting discharge using only geometric in-site information given by LiDAR data and the equations of Leopold and Maddock (1953) and (Parker, 1978a,b) in hydraulic geometry relationships and Shields number values, respectively, in order to bypass the geographical/location assumptions. This method is not expected to be better than those that already exist, but to be quicker and easier to apply as a screening tool or a prior check for more detailed models.

1.3 Literature Review (Overview)

A review of completed and ongoing research has been conducted to identify current knowledge or methodologies that may be appropriate for predicting low probability discharge on ungauged streams from hydraulic geometry and critical shear stress values.

The study of remotely sensed bankfull discharge based on geometry is not

new; many authors such as Gleason and Smith (2014), and Bhatt and Tiwari (2008) worked with estimation of bankfull discharge or rating curves from remotely sensed data. But the majority of research in this field focuses on large rivers (> 50 meters wide). In contrast to the coarse resolution of satellite observations used for the extraction of hydraulic properties at global scales, high-resolution imagery has been used for decades to produce digital terrain models, for example King et al. (2018) created rating curves from aerial imagery using many hydraulic assumptions. These studies demonstrate the accuracy of extracting digital surface models (DSMs) of river banks from aerial imagery, but stop short of integration with hydraulic modeling to estimate river discharge.

Many authors such as Singh (2003), Bjerklie et al. (2005), and Nathanson et al. (2012) have worked on the estimation of bankfull discharge and predicting flow by applying regression equations which involve regional information. But none of them have applied distribution functions in order to predict discharge.

The theory for estimating bankfull discharge is mainly based on Leopold and Maddock (1953) hydraulic geometry relations and sediment transport threshold Shield's number Parker (1978a,b).

1.3.1 Hydraulic Geometry Relations and Threshold Discharge

At-a-station hydraulic geometry (AHG) theory relates geometric stream features to bankfull discharge by assuming a power-law connection.

$$B_{bf} = aQ_{bf}^{b} \tag{1.1}$$

$$D_{bf} = cQ_{bf}^{f} \tag{1.2}$$

where Q_{bf} is bankfull discharge; B_{bf} and D_{bf} are bankfull width and depth, respectively; and the coefficients and exponents a, b, c, and f are empirical best fit parameters, which were first described by Leopold and Maddock (1953), and are an often-used framework in river remote sensing (Smith et al., 1996; Smith and Pavelsky, 2008; Pavelsky, 2014). At-many-stations hydraulic geometry (AMHG) is a recently discovered geomorphic phenomenon holding that the coefficients and exponents in traditional AHG are stable and predictable for a given river, thus linking individual cross sections to one another along a river (Gleason and Smith, 2014). Using simple geometric relationships, it is possible to use the same equation structure for bankfull section area.

$$A_{bf} = pQ_{bf}^{m} \tag{1.3}$$

where p is the Area-Coefficient ($a \times c$) and m the Area-Exponent ($b + f$). Leopold (1994) stated that most investigations have concluded that the bankfull discharge recurrence intervals ranges from 1.0 to 2.5 years. Also, (Leopold and Maddock,

1953) demonstrated that values of $b = 0.42$ and $f = 0.28$ are suitable for the at-a-station hydraulic geometry equations for a wide range of geographic settings and stream sizes. However, the coefficients (a,c) are related to regional and geographic data. Since these parameters are sensitive to stream geometry, therefore some assumptions and changes in the coefficients can be observed when analyzing the river geomorphology.

1.3.2 Bankfull Sediment Transport Threshold

Geometric relationships do not give too much information on their own, because of the geographical dependence of the parameters. It is also possible to define the bankfull discharge as shear stress threshold in which the momentum of flow is enough to give a temporary stable geometry to the channel bankfull cross-section. Parker (1978a,b) and Paola et al. (1992) developed a simple theory for bankfull characteristics of rivers. The the formulation is based on a resistance equation describing quasi-normal bankfull flow, transport of bed material load at quasi-equilibrium, and a specified bankfull Shields criterion as follows:

$$\tau^*_{bf50} = \frac{\tau_{bf}}{g(\rho_s - \rho)d_{50}} = constant \tag{1.4}$$

$$\tau_{bf} = \rho g R_{bf} S \tag{1.5}$$

where τ^*_{bf50} is the non-dimensional channel-formative Shields number, τ_{bf} is the reach-averaged mean bed shear stress [Pa], ρ and ρ_s are water and grain density values, respectively $[kg/m^3]$, d_{50} is median bed grain size $[m]$, and R_{bf} is the bankfull

hydraulic radius $[m]$.

Paola et al. (1992) proposed the assumption of constant bankfull Shields number in modeling the morphodynamics of streams, Figure 1.1 shows the Shields number against nondimensional discharge, $\hat{Q}$, defined as,

$$\hat{Q} = \frac{Q}{d_{50}^2 \sqrt{\frac{\rho_s - \rho}{\rho} g d_{50}}} \tag{1.6}$$

Despite a considerable amount of scatter, the diagram allows the following approximate estimates of bankfull Shields number for gravel-bed and sand-bed streams based on averages (Parker, 1978a,b; Dade and Friend, 1998).

$$\text{Gravel-Bed:} \quad \tau^*_{bf50} = 0.0487$$

$$\text{Sand-Bed:} \quad \tau^*_{bf50} = 1.86$$

The considerable scatter in the different bankfull dimensionless shear stress values are probably due to differing fractions of wash load versus bed material load, differing amounts and types of floodplain vegetation, or different hydrologic regimes. Also, a threshold for a bankfull section slope around $S^* = 0.001$ for gravel and sand bed streams can be observed and be useful for estimating and differentiating when each shear stress threshold should be used (Figure 1.2).

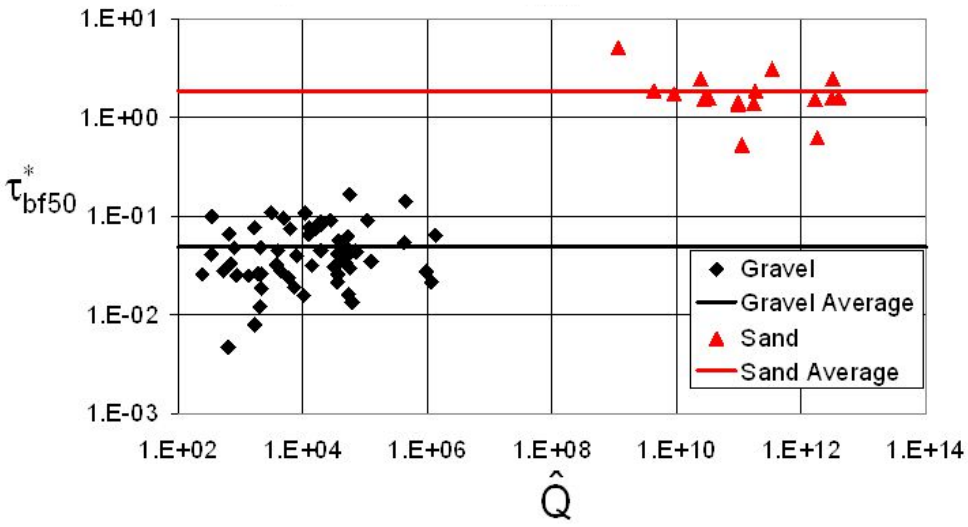

Figure 1.1: Average Shields number (Eq. 1.4) of gravel and sand bed streams (Parker, 2004). $\hat{Q}$ is dimensionless discharge, which is inversely related to median bed particle diameter.

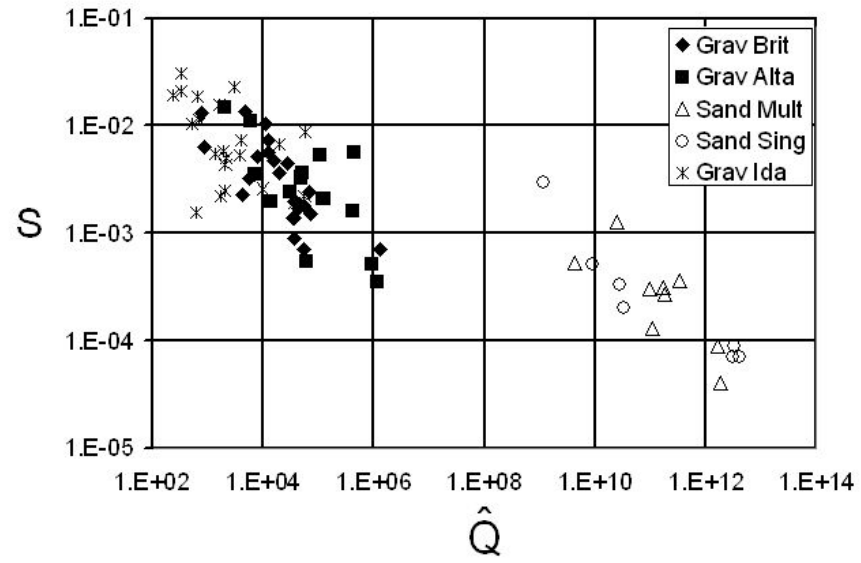

Figure 1.2: Slope of gravel and sand bed streams (Parker, 2004). $\hat{Q}$ is dimensionless discharge, which is inversely related to median bed particle diameter.

The main assumption is that flows less than the bankfull discharge value do not significantly alter the channel shape, consistent with with the concept that many streams are threshold channels at the bankfull stage, and the evolution of river cross-section is towards a quasi-equilibrium bankfull Shields number (Parker, 1978a,b). The main complications would be variable fractions of wash load versus bed material load, variable types of floodplain vegetation, and different hydrologic regimes.

Shear stress and the Shield's number are related to hydraulic geometry through the bankfull section relationship. However, the first approach needs a regional analysis to calibrate the coefficients, and the second approach only works in a bankfull section. Therefore, by combining both approaches it is possible to identify the bankfull section and compute its respective discharge.

1.4 LIDAR to Obtain Stream Morphology Data

Recently, LiDAR scanning techniques have gained popularity for the collection of topographic data and for remote sensing of river channels (Wobus et al., 2006; Snyder, 2009). The main issue in measuring channel cross-sections by LiDAR is that it does not measure elevation through water (i.e., bathymetry) because visible-frequency light is reflected by water). Therefore, most of the key points are measured on top of the stream resulting in water surface elevation data rather than bed elevation, but assumptions and/or different approaches can be undertaken to compensate this issue.

The use of LiDAR-derived data as an input for modeling theoretical rating curves opens a realm of possibility to remotely sense and monitor stream discharge in channels in remote locations. This study serves as a proof-of-concept for the utility of LiDAR-derived channel geometry in a physically based rating curve model.

Chapter 2

Methods

The hydraulic geometry method is intended for application to ungauged sites. The method is applied to gauged sites in the state of Maryland (US) as a test. The procedure consists of:

1. Fit the observed annual peak discharge data to the EVTI distribution, and predict gauge-based discharges for return periods 2, 5, 10, 20, 50, 100, and 200 years (annual exceedance probabilities 0.5, 0.2, 0.1, 0.05, 0.02, 0.01, and 0.005, respectively).

2. Determine bankfull depth and discharge from the LiDAR cross-section data.

3. Use the bankfull discharge to find the parameters of the hydraulic geometry-based EVTI distribution.

4. Compare the gauge- and LiDAR-derived bankfull discharge.

5. Predict to 200-year discharges based on hydraulic geometry.

6. Compare the HGM and gauge-based to 200-year discharges.

Figure 2.1 gives an overview of the methodology used in the study. The following sections describe the steps.

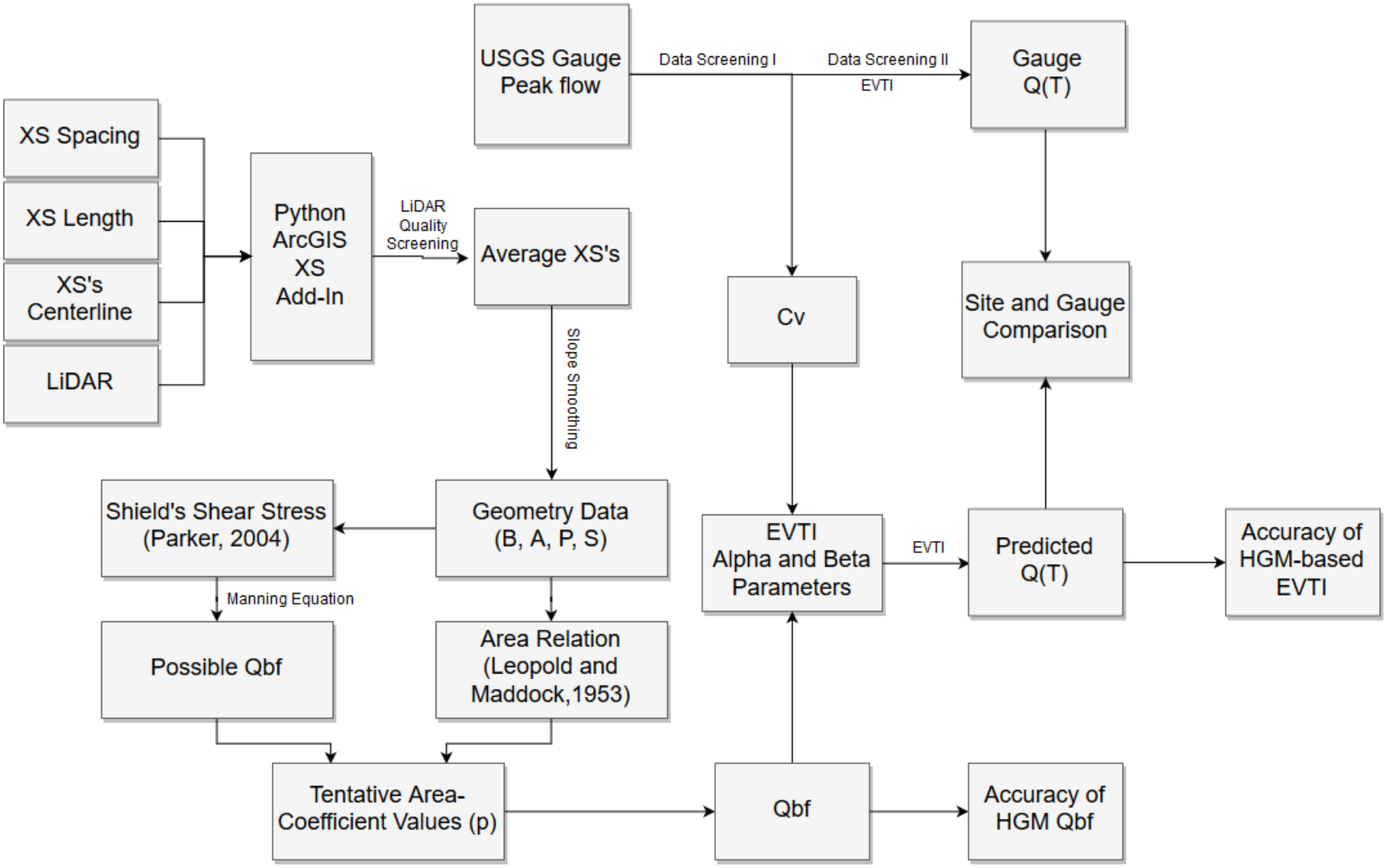

Figure 2.1: HGM method

2.1 Observed Data (Gauges) Filtering

Peak annual streamflow data were obtained from the USGS (2019) database (only for stations in the state of Maryland), for a total of 275 stations. An Extreme Value Type I (EVTI) distribution (Gumbel) was applied to each gauge that had more than 30 years of recorded data. Using 30 years or more of data for each station will allow a prediction of low probability flow with a good confidence level (Rossi et al., 1984). The EVTI parameters were estimated using the method of moments.

This screening was complemented by testing and correlating (Q-Q plots) the EVTI results (population) to ensure it has a good fit. A two-sample correlation coefficient was computed to ensure goodness of fit (Q-Q plot), as an example Figure 2.2 shows the correlation coefficients for one site. As a criterion, only the sites that had a Pearson correlation coefficient greater than 0.96 were retained for further analysis. This filtering process retained a total of 30 stations with extrapolated low probability flow (Return periods of 2, 5, 10, 20, 50, 100, and 200) to be compared with the Hydraulic Geometry Method. Table 2.1 shows the selected gauges and their statistical properties.

2.2 Cross-Section Geometry Data

To extract geometry information LiDAR data were downloaded from the iMAP service of the state of Maryland (MD-iMAP, 2019). The data were collected between 2011 and 2019 at different point densities, depending on county; publicly available

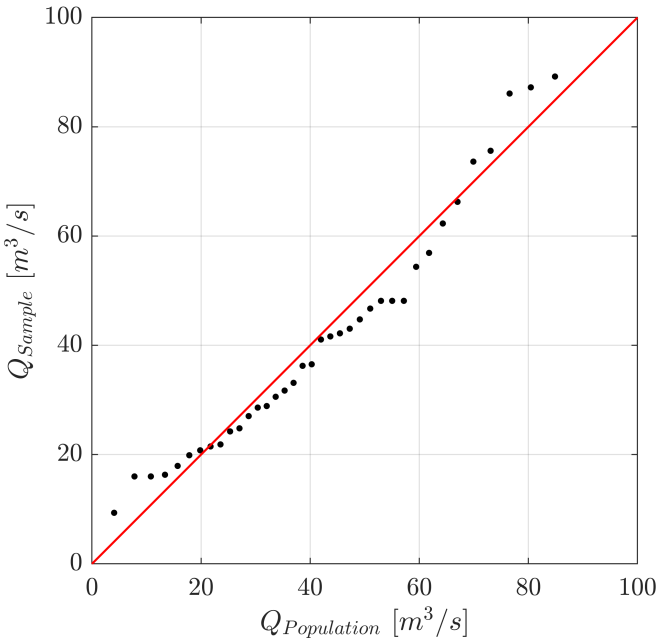

Figure 2.2: Q-Q Plot for Site #6 with a r=0.9856

Table 2.1: Gauge data properties for annual peak discharge

Site #	Record Length (years)	$\bar{x}$ $[m^3/s]$	s $[m^3/s]$	Median $[m^3/s]$	C_V [-]
1	66	23.88	13.87	19.71	0.58
2	64	4.87	3.14	3.92	0.64
3	43	10.88	10.32	7.08	0.95
4	70	70.96	48.61	58.62	0.69
5	91	120.45	67.46	102.22	0.56
6	43	49.28	34.00	41.63	0.69
7	51	89.17	58.55	63.15	0.66
8	74	75.32	43.58	60.88	0.58
9	31	5.13	4.95	3.34	0.97
10	36	38.82	20.96	31.57	0.54
11	42	28.50	24.33	16.98	0.85
12	77	94.05	68.40	75.89	0.73
13	51	27.72	15.46	27.04	0.56
14	35	26.12	15.09	21.69	0.58
15	35	45.96	30.79	32.00	0.67
16	39	43.27	20.22	40.21	0.47
17	63	108.95	67.33	87.78	0.62
18	69	87.25	45.25	77.87	0.52
19	91	254.15	138.06	210.11	0.54
20	54	3.72	2.89	2.96	0.78
21	90	92.12	63.90	73.34	0.69
22	70	93.55	70.40	60.74	0.75
23	77	272.86	112.43	254.29	0.41
24	43	27.96	16.61	26.45	0.59
25	30	41.21	24.01	31.15	0.58
26	76	138.82	71.98	112.42	0.52
27	94	196.38	81.98	187.17	0.42

Note: $C_V = \bar{x}/s$

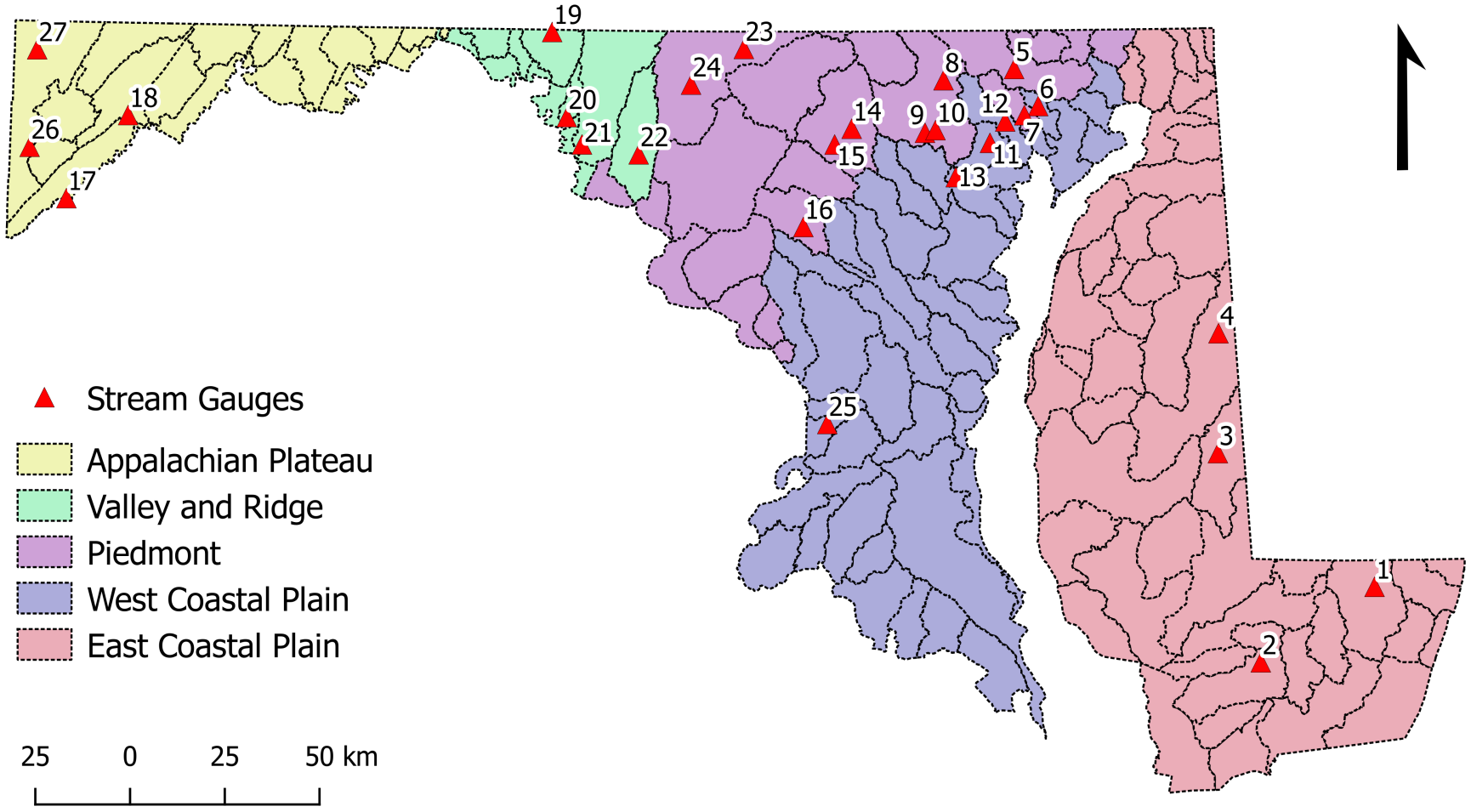

Figure 2.3: Sites and gauges locations

for each county they are provided in 1-m or finer resolution gridded elevation. The data are offered in many geographical location classifications (key points, ground, bridge deck, etc.). Since this research is interested only in river cross-section, the LiDAR data were obtained for ground and water classifications.

One of the issues with LiDAR is that key points in the measurements may have a significant amount of noise, caused by vegetation and/or structures in the ground. This issue can be compensated by applying a tolerance criterion for the elevation. To ensure a smooth fit of the average cross-section a tolerance difference of 3 meters between each sequentially data key point was applied.

Other issue, as mentioned before, is that LiDAR does not give bathymetry information, therefore, many of the key points are measured on top of the stream resulting in water surface elevation data. It is assumed that LiDAR measurements were done in low flow conditions. Considering low-probability, high volume discharge, baseflow is relatively unimportant from a flow magnitude point of view, therefore baseflow will not be considered part of the flow and the LiDAR-derived water surface is treated as stream bed for this research. An analysis of computed bankfull data would indicate how important it is to allow for the baseflow of the streams to impact the bankfull discharge predictions, since wider streams have more baseflow influence on the bathymetry.

A straight centerline must be applied to define the perpendicular cross-sections. This centerline must be done through the stream lowest points (inverts) across the cross-sections. It is important that the centerline has significant length in order to be representative, but also short enough to avoid meandering. A 50- or 100-meter

centerline was assumed to be representative for estimating slope for an average cross-section with 5 meters of spacing; the centerline slope will be assumed the same as the water surface slope for this length. Within the reached sampled, channel cross-sections were extracted every 5 meters; the use of this interval is a compromise between the attempt to obtain as much a continuous record of variation in channel form as possible, and that necessary to cover representative portions of the stream (given that natural channels have heterogeneity, i.e. riffles, pools, etc.). The length of each cross-section should be enough to extract all of the information from the, yet unknown, bankfull depth. To assure full coverage of all of the streams, a 200-meter line of perpendicular cross-sections to each side of the centerline was extracted from the LiDAR on each cross-section and site, as shown in Figure 2.7 for site #5.

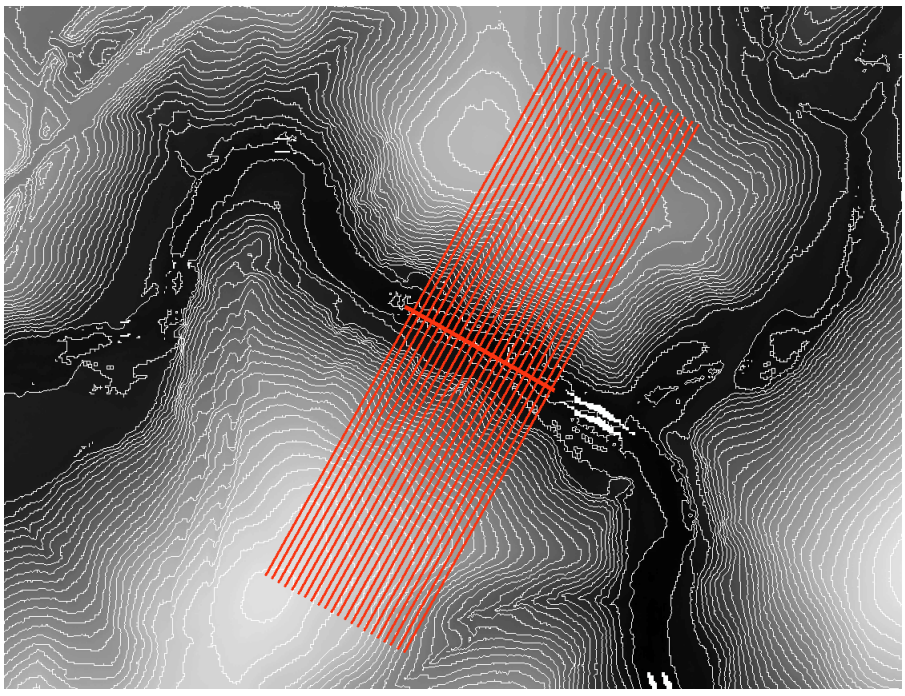

Figure 2.4: Centerline and cross-section lines drawn on LiDAR elevation grid (Site #12)

To ensure a good prediction, LiDAR data were reviewed before applying the method. This review was accomplished by observing a consistent trend of points towards a smooth average cross section. If this condition was not satisfied then the site was discarded for the purpose of this research, as shown in Figure 2.5.

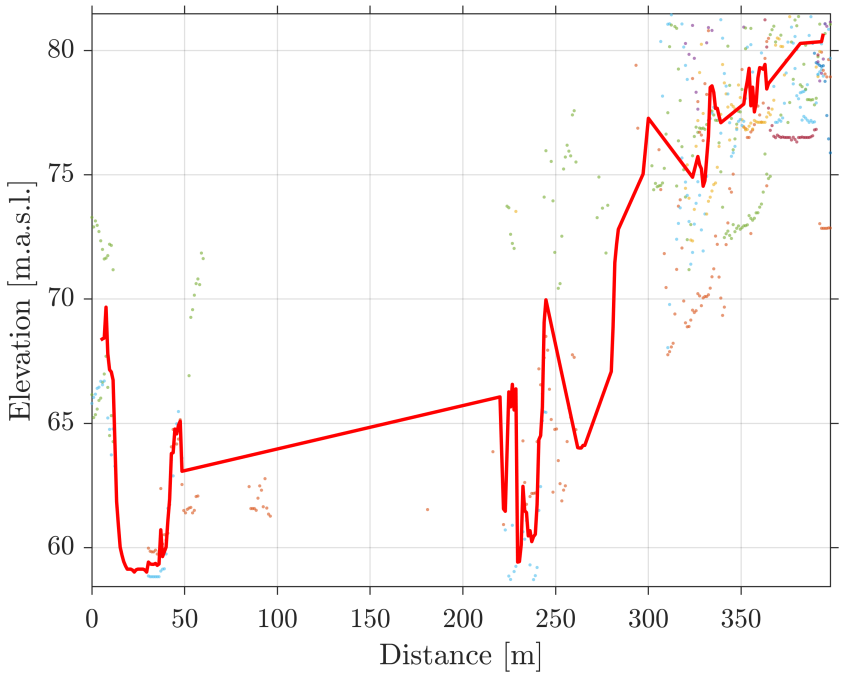

Figure 2.5: Example of unacceptable LiDAR data cross-section near gauge Hydrologic Unit 01646550. Note: Station was discarded.

Geometric properties were estimated from the cross-sections, such as: $S(L)$, $B(d)$, $A(d)$, $P(d)$, and $D(d)$, where d is any depth of the cross-section measuring from the assumed channel invert; (at this point in the analysis, any d could potentially be identified as bankfull depth), and L is the length of the centerline, which is determined by inspection of the LiDAR DEM to be representative of the reach containing the gauge (between 50 and 200 meters).

An average cross-section was computed by taking the mean of each LiDAR

point on the same pixel location distance on the reach. Places where the elevation decreased compared to the previous point (counting from the lowest elevation in the channel) were filled for each cross-section to ensure model stability and avoid irrational drops in discharge while increasing the depth (Figure 2.7).

The representative slope of the cross-section was computed by taking the moving average (with a period of a fifth of the length of the centerline) of the invert for each cross-section along the centerline. This method ensures a smooth stream line without being affected by LiDAR noise effects. The smoothed slope values were averaged to obtain a single slope, S, for each site. As an example, Figure 2.6 displays the effects of the smoothing process.

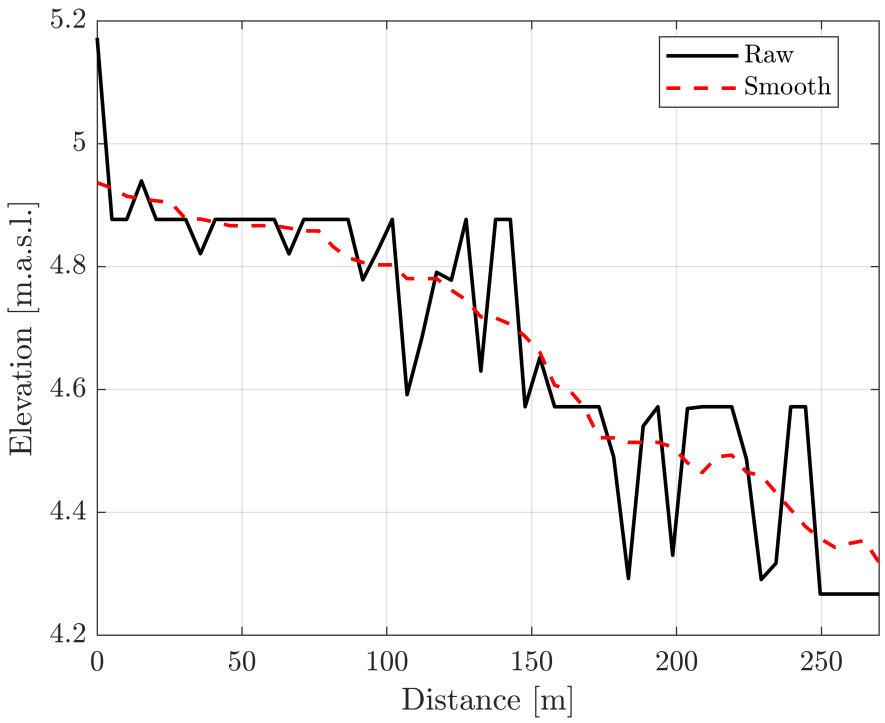

Figure 2.6: Longitudinal profile of cross-section invert elevation (Site #3), showing smoothing

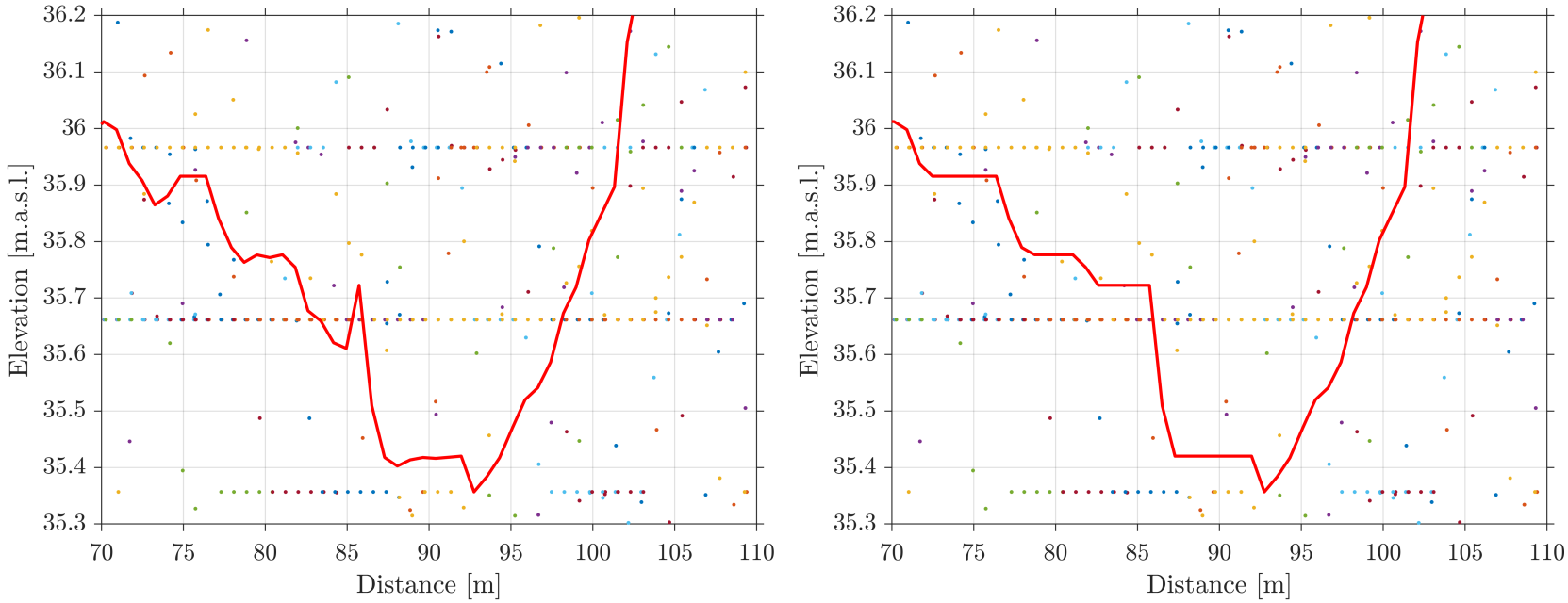

Figure 2.7: Average cross-section and LiDAR data (Site #21) showing filling of dips. Left is not filled, Right is filled.

2.3 Identifying Bankfull Shear Stress Discharge

The bankfull discharge is interpreted as a threshold on sediment stability (Carling, 1988); therefore, a stable channel would be defined by flows smaller than the threshold. The stability factor is a function of bankfull cross-section characteristics and bedload composition. For gravel-bed the Shield's shear stress is significantly lower than for sand-bed because sediment transport is easier on sand (Parker et al., 2007). Also, the stability factor can be translated to a nondimensional shear stress (bankfull Shields number: Eqns. 1.4, 1.5). With cross-section data, estimating shear stress is easy to do and does not need a lot of computational resources. The hydraulic radius is defined as the area divided by the wetted perimeter of the flow cross section. However, for a bankfull hydraulic radius, it is necessary to know before-hand the bankfull depth, since the bankfull depth dictates all cross-section parameters. For a range of possible channel depths, shear stress, $\tau_{bf}^{'}$ and bankfull discharge $q_{bf}^{'}$, can be computed as if that depth were the bankfull depth; each depth is thus a tentative bankfull depth ($d_{bf}^{'}$); further testing identifies which depth satisfies all requirements (equations) to be identified as the section's unique bankfull depth, $d_{bf}^{'}$. As an example, Figures 2.8 and 2.9 illustrate the relation between these parameters. Channel depth is increased from invert to 2.0 m in increments of 0.1 meters; f and $\tau_{bf}^{'}$ and $q_{bf}^{'}$ are calculated at each tentative bankfull depth, $d_{bf}^{'}$. The bankfull depth is assumed to not be higher than 2 meters (in order to avoid changes in elevation due to roads or similar infrastructures).

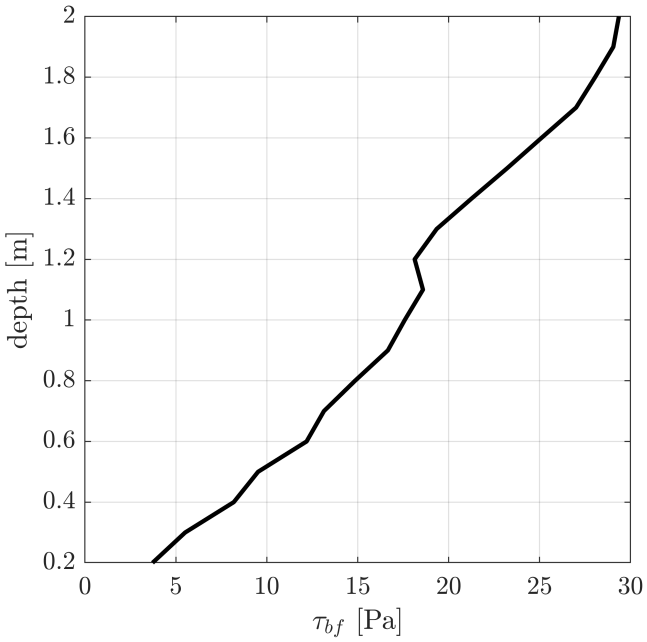

Figure 2.8: Depth vs. tentative bankfull shear stress computed for each depth assuming each depth as bankfull (Site #6)

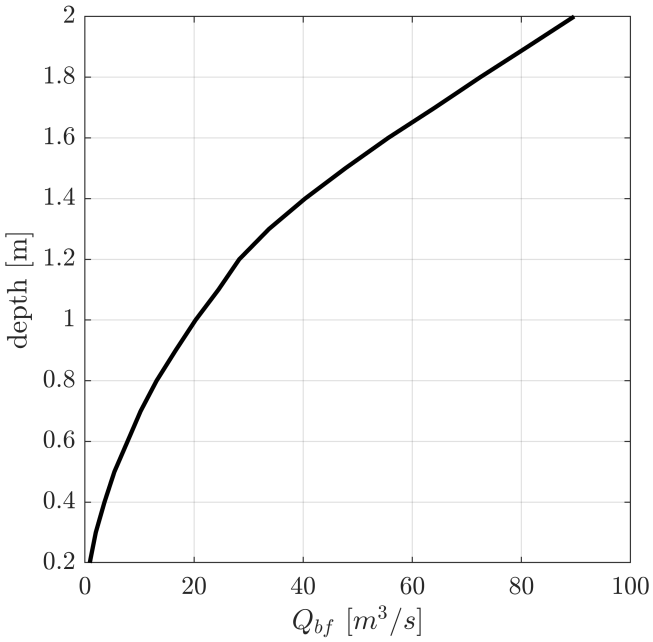

Figure 2.9: Depth vs. tentative bankfull discharge computed for each depth assuming each depth as bankfull (Site #6)

A bed-slope approach was used to estimate bedload sediment size using (Parker, 2004) diagram (Figure 1.2). The nondimensional bankfull shear stress estimation with bedload information implies a median grain size (d_{50}). With grain size information a Manning coefficient can be estimated using one (or more) of many Manning-diameter relations (Kim et al., 2010), like the ones shown in Table 2.2. These equations are most accurate when water is sufficiently deep that stream bed composition creates elements with roughness height much less than depth, analogous to the ϵ/D relationship in pipe flow (Kim et al., 2010). In this case the average of the three respective equations (Eq. 2.1) was used as the characteristic Manning coefficient. Once the Manning coefficient has been estimated it is possible to apply the Manning equation to the stream cross-section using a tentative bankfull depth, d'_{bf}.

$$n = \frac{n_1 + n_2 + n_3}{3} \tag{2.1}$$

where n_i are the different estimates of roughness from Table 2.2.

Table 2.2: Equations to determining Manning's roughness coefficient from grain size

Author	Equation
Strickler (1923)	$n_1 = 0.047 d_{50}^{1/6}$
Keulegan (1938)	$n_2 = 0.039 d_{50}^{1/6}$
Bray (1979)	$n_3 = 0.0495 d_{50}^{0.16}$

2.4 Identifying The Bankfull Section Through Hydraulic Geometry

In order to find the true bankfull discharge from the tentative values, a second approach was used by applying AHG relationships. Physically, it is expected that the relationship between discharge and area (Eq. 1.3) changes when flow in a given channel increases from in-bank to out-of-bank. The depth at which a recognizable change occurs is the bankfull depth. Area curves are generated using exponent values (m in Eq. 1.3) from the literature, and calculating the coefficient (p in Eq. 1.3) for each depth using the tentative bankfull discharge calculated as described in Section 2.3. The bankfull depth is identified as the point in the curve where p changes most rapidly (greatest slope). This method is less biased than visually inspecting each cross-section, and it's assured that the bankfull extracted data will all have the same definition. Values of the exponents $b = 0.42$ (Eq. 1.1) and $f = 0.28$ (Eq. 1.2) from the literature was used for this model, further analysis will be conducted in order to estimate the effect of this assumption.

Combining the HG and the shear stress approaches, is essentially finding two unknowns (bankfull discharge and depth) from two equations (AHG and critical shear stress), which can be solved by defining a bankfull section for an identified area with coefficient values from the Area-Coefficient plots (channel breakpoint from baseflow to floodplain). The area coefficient, p, is calculated for each tentative bankfull depth, d'_{bf}, analyzed in Section 3.4. A slope analysis of this curve will help identify the bankfull discharge that satisfies both approaches. The incremental value (0.1 meters) is also consistent to identify correctly the floodplain when estimating

the bankfull breakpoint; using a smaller value could cause to retrieve changes into the error range of the LiDAR data and, therefore, wrong bankfull section identification. As an example Figure 2.10 shows the maximum slope in the Area-Coefficient diagram.

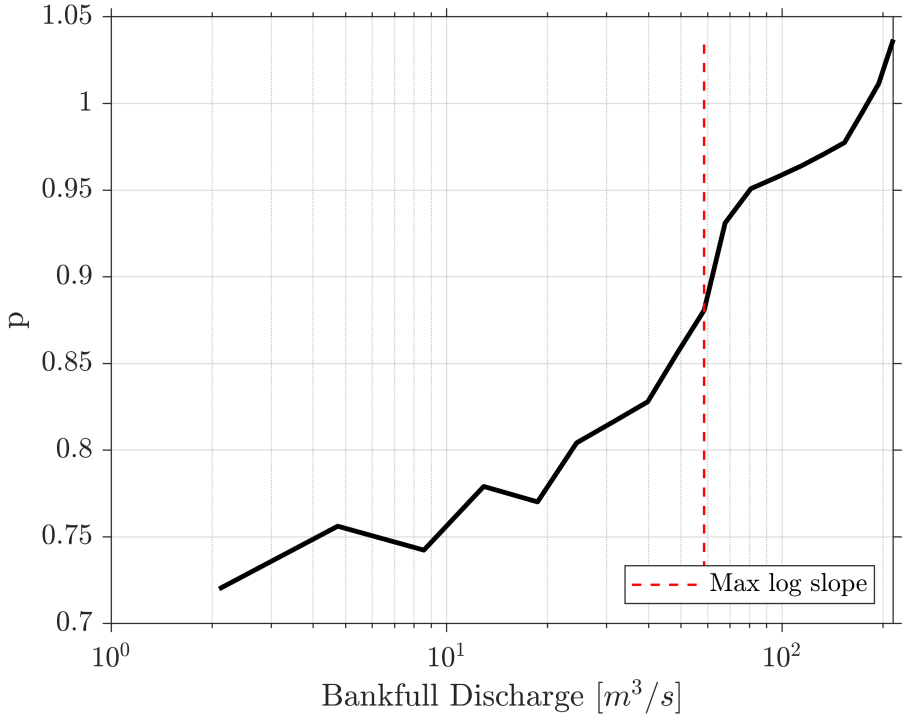

Figure 2.10: Area-coefficient value (Site #6) computed for each tentative bankfull discharge.

A curve of Area-Coefficients p and tentative bankfull discharge were analyzed to identify the steepest slope (slope breakpoint) in the curve (abrupt change). The slope was calculated by using the log values of the discharge.

$$Slope\,breakpoint \quad = \quad max \left\{ \frac{p^{i+1} - p^i}{log(q_{bf}^{i+1}) - log(q_{bf}^i)} \right\} \tag{2.2}$$

Each HG-derived bankfull flow value can be compared to the gauge-based 2-year

return period discharge. Overall accuracy of the method is evaluated by calculating statistics of all the analyzed locations: systematic error (mean error) and non-systematic error (SE/SY). Many authors identify bankfull discharge as a 2-year return period (Leopold, 1994).

2.5 Low Probability Prediction/Extrapolation

The previous method will result in a computed bankfull discharge. Continuing to assume that Q_{bf} represents the 2-year return period, the calculated Q_{bf} is assumed to represent the median annual peak value in estimating the parameters of the HG-based EVTI. To estimate the two parameters of the $EVTI(\alpha, \beta)$, an additional sample moment is required. The coefficient of variation (C_V) of annual peak flows can be used to estimate the standard deviation of the population. The average C_V values of all the Maryland gauges with a record of 15 years or more was computed (Table 3.1), and was assumed to represent the population. The EVTI parameters were estimated using the median and the assumed C_V.

$$C_V = \frac{s}{\bar{x}} \tag{2.3}$$

$$\alpha = \bar{x} - \gamma\beta \tag{2.4}$$

$$\beta = s\frac{\sqrt{6}}{\pi} \tag{2.5}$$

$$Q_{bf} = \alpha - \beta ln(ln(2)) \tag{2.6}$$

Having defined the EVTI distribution with the α and β parameters, it is

possible to extrapolate the assumed 2-year return period discharge (bankfull) to a 200-year return period. These HG-based predictions can be compared to extrapolated gauge-based data with the EVTI parameters estimated by Method of Moments from observed data. A SE/SY (non-systematic error) value was computed comparing gauge-based and HG-based Q_T at all study sites for selected return periods, T, to analyze the results consistency. Also, an individual analysis was made for each site using a frequency-discharge plot. These plots will show the mean relative error (MRE) of the model and observed discharges, as shown as an example in Figure 2.11.

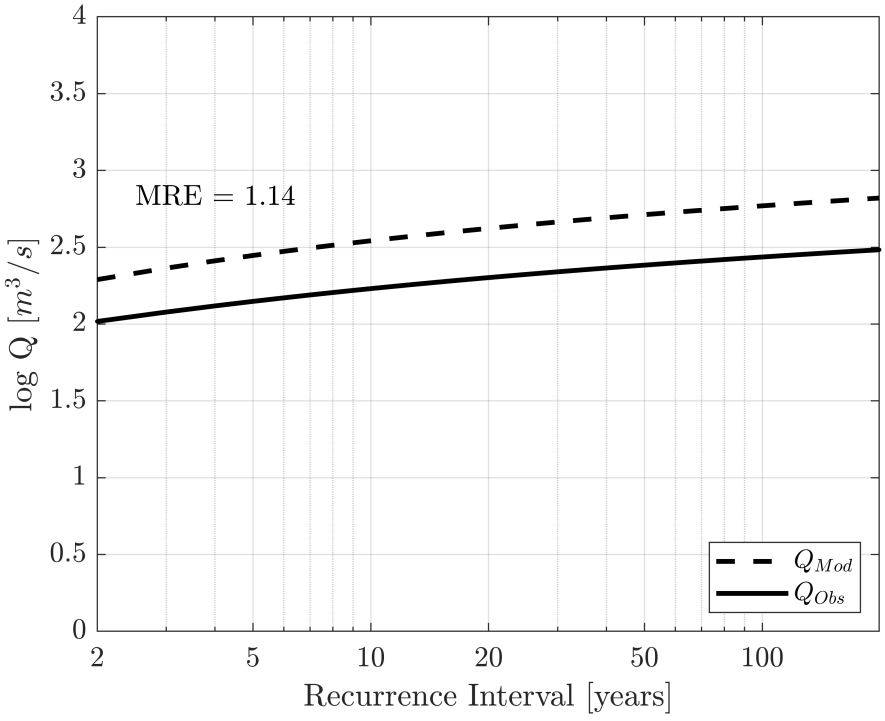

Figure 2.11: Model and observation frequency curves (Site #7). Note: Q_{Mod}: EVTI parameters estimates from HGM bankfull Q and assumed C_V. Q_{Obs} EVTI parameter estimated from annual peak data. MRE=Mean Relative Error

2.6 Effects of Assumptions on Model Accuracy

A number of quantities are assumed in the analysis; it is important to assess how the assumptions affects the model results: the area exponent (Eq. 1.3), bankfull return period, and C_V of annual peak flow (Eq. 2.3). For the area-exponent m, values can range from 0.5 to 1.0 (Singh, 2003). According to the literature bankfull return period usually ranges between 1.5 and 2.5 years (Leopold, 1994). For C_V, a range according to the observed standard deviation, $s(C_V)$, was analyzed. The analysis for these values will show the impact on the accuracy between the gauge-based and HG-based EVTI (since the C_V assumption does not affect the bankfull estimation).

$$0.5 < m < 1.0 \tag{2.7}$$

$$1.5 < T_{bf} < 2.5 \tag{2.8}$$

$$C_V' = \overline{C_V} \pm std(C_V) \tag{2.9}$$

Chapter 3

Results

3.1 Average Cross-Section

Average cross-sections were estimated using the available elevation LiDAR data set. LiDAR data on some gauges had a significant amount of noise due to vegetation and structures near the stream, therefore, four of them were discarded from the sample. A total of 27 sites were left for analysis. Table 3.2 shows bankfull values according to the Area-Coefficient method (Sections 2.3-2.4).

3.2 Area-Coefficient Bankfull Identification

Table 3.1 shows the computed bankfull values (HGM). Sites with bankfull width >90 meters showed greater relative error (RE) than the low-order streams. This can be mainly because of the baseflow covering substantial part of the bathymetry, changing the accuracy of the predictions.

$$RE = \frac{Q_{Mod} - Q_{Obs}}{Q_{Obs}} \tag{3.1}$$

$$MRE = \frac{1}{N} \sum \frac{Q_{Mod} - Q_{Obs}}{Q_{Obs}} \tag{3.2}$$

Table 3.1: HGM and observed bankfull discharge

Site #	Model Q_{bf} [m^3/s]	Observed Q_{bf} [m^3/s]	RE
1	6.83	21.60	-68%
2	2.68	4.36	-39%
3*	332.24	9.19	+3515%
4*	197.97	62.98	+214%
5	23.24	109.37	-79%
6	24.47	43.69	-44%
7	137.83	79.55	+73%
8	75.31	68.16	+10%
9	1.36	4.32	-68%
10	44.19	35.37	+25%
11	6.66	24.50	-73%
12	73.36	82.81	-11%
13	61.47	25.18	+144%
14	1.27	23.64	-95%
15	13.72	40.90	-66%
16	272.69	97.89	+179%
17	119.94	79.82	+50%
18*	194.05	231.47	-16%
19*	218.98	3.24	+6655%
20	11.65	81.62	-86%
21	17.04	81.99	-79%
22*	402.88	254.39	+58%
23	2.02	25.23	-92%
24	55.36	115.91	-52%
25	35.27	37.27	-5%
26	138.82	127.00	+9%
27	53.20	182.91	-71%

Note: Model values correspond to discharge in the Area-Coefficient breakpoint. Observed values come from the EVTI for a 2-year return period.
* High-order streams exluded from further analysis.

Table 3.2: Computed bankfull geometry by hydraulic geometry method

Site #	Hydrologic Unit	USGS Gauge Name	B [m]	D [m]	S [-]	A [m^2]
1	01485000	Pocomoke River Near Willards	28.8	0.5	0.0001	559.0
2	01486000	Manokin Branch Near Princess Anne	16.7	0.5	0.0001	458.4
3	01489000	Faulkner Branch At Federalsburg	109.9	1.8	0.0033	164.3
4	01491000	Choptank River Near Greensboro	139.4	1.9	0.0005	122.1
5	01580000	Deer Creek At Rocks	18.6	1.2	0.0008	32.7
6	01581500	Bynum Run At Bel Air	23.1	1.1	0.0027	44.5
7	01581700	Winters Run Near Benson	30.8	1.9	0.0086	44.8
8	01582000	Little Falls At Blue Mount	39.3	1.5	0.0029	60.3
9	01583580	Baisman Run At Broadmoor	6.2	0.2	0.0310	31.7
10	01583600	Beaverdam Run At Cockeysville	38.6	1.7	0.0001	76.5
11	01584050	Long Green Creek At Glen Arm	10.7	0.5	0.0242	39.1
12	01584500	Little Gunpowder Falls At Laurel Brook	28.6	1.9	0.0016	41.6
13	01585200	West Branch Herring Run At Idlewylde	19.1	1.7	0.0109	25.7
14	01586210	Beaver Run Near Finksburg	15.1	0.2	0.0029	121.1
15	01586610	Morgan Run Near Louisville	43.8	0.5	0.0022	120.6
16	01595000	North Branch Potomac River At Steyer	71.3	1.9	0.0010	99.9
17	01597500	Savage Riv Bl Savage Riv Dam Near Bloomington	86.7	1.2	0.0046	150.7
18	01614500	Conococheague Creek At Fairview	164.2	1.3	0.0001	287.5
19	01617800	Marsh Run At Grimes	103.8	1.9	0.0025	122.8
20	01619500	Antietam Creek Near Sharpsburg	70.0	0.4	0.0001	203.7
21	01637500	Catoctin Creek Near Middletown	47.3	0.8	0.0003	122.8
22	01639000	Monocacy River At Bridgeport	161.4	1.9	0.0005	201.8
23	01641000	Hunting Creek At Jimtown	18.8	0.3	0.0001	588.2
24	01649500	Northeast Branch Anacostia River At Riverdale	20.4	1.8	0.0053	26.3
25	01653500	Henson Creek At Oxon Hill	22.1	1.3	0.0052	102.6
26	03075500	Youghiogheny River Near Oakland	83.0	1.0	0.0145	154.2
27	03076500	Youghiogheny River At Friendsville	58.9	0.4	0.0521	215.2

Note: B: Bankfull width, D: Bankfull Depth, S: Slope, A: Bankfull Area

3.3 C_V values on gauged sites

Consistency on the observed sites was found for the coefficient of variation of the annual peak discharge (Figure 3.1) for gauges with more than 15 annual measurements on record. The C_V values (N = 146) averaged 0.85 (s = 0.37) showing a low variability in the gauges annual flow. The mean value was used to compute the model EVTI parameters.

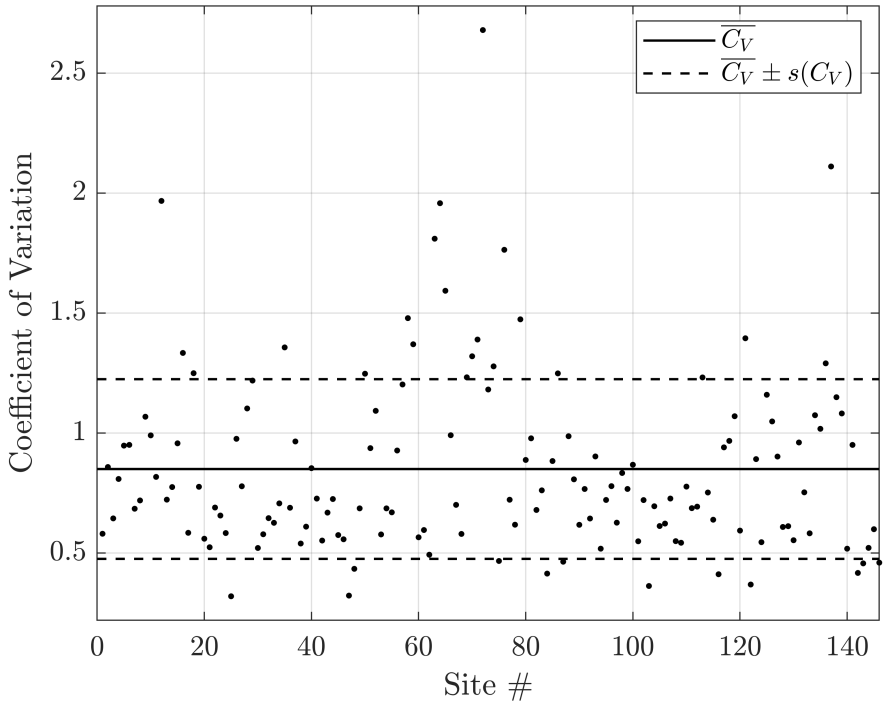

Figure 3.1: Coefficient of variation (C_V) of annual peak flow for all gauges (N=146)

3.4 Model Accuracy

For the accuracy measures a Relative Mean Error (RME) and Root Mean Squared Error (RRMSE) were computed. The model error is defined as:

$$E = Q_{bf,m} - Q_{bf,g} \tag{3.3}$$

where m indicates the HGM, and g indicates gauge data (observed). Relative mean error (bias) is average error divided by measured (gauge) average, as follows:

$$RME = \frac{\frac{\sum E}{n}}{\frac{\sum Q_{bf,g}}{n}} = \frac{\bar{E}}{\overline{Q_{bf,g}}} \tag{3.4}$$

Relative Root Mean Square Error (RRMSE) is the square root of mean squared error, divided by the standard deviation of the measured (gauge) average, or the non-systematic error (SE/SY):

$$RMSE = \sqrt{\frac{\sum E^2}{df}} \tag{3.5}$$

$$RRMSE = \frac{RMSE}{s(Q_{bf,g})} = SE/SY \tag{3.6}$$

where *df* is degrees of freedom for the mean squared error calculation (equal to number of observation/model pairs).

3.4.1 Bankfull Discharge

Bankfull depth and discharge were modeled at 27 sites and compared to Q (2-year) from in-situ gauge data with an absolute mean relative error of 467% (median of 73%), shown in (Table 3.1). The maximum percent errors occurred at sites #3 and #19, with the HGM overpredicting by two orders of magnitude. The sources of these errors are discussed later.

However, this strategy takes into account various morphological classes of streams and assumes negligible baseflow discharge. When considering only the narrower streams (low-order sites), the mean relative mean error (absolute value) for the same properties lowers to a mean of 80%, and a median of 71% (Table 3.1).

On the other hand, a calculation of model error (N=27), resulted in a non-systematic error (SE/SY) value of 1.52 (Figure 3.2). When not considering the wider streams (N=22), the same value improves to 1.31 (Figure 3.3). These results show that stream size does not improve the overall accuracy of the model, even though there is an improvement in the relative bias (RME) from 29% to -15%.

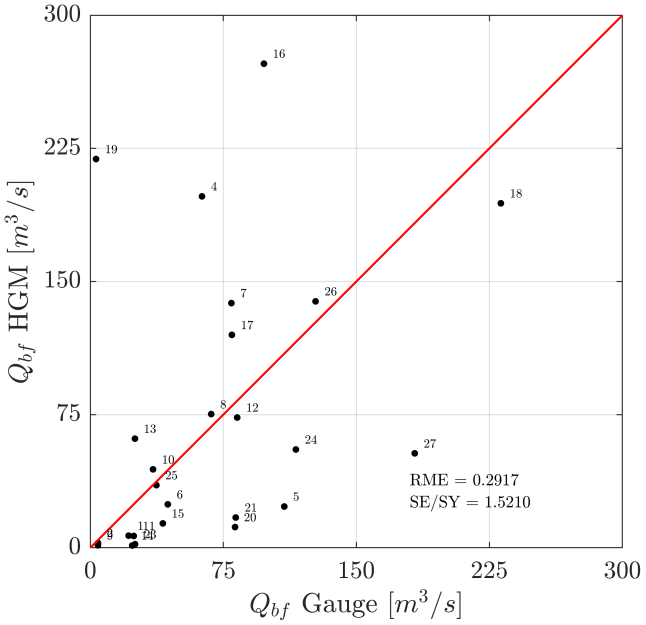

Figure 3.2: Computed and gauged bankfull discharge for all streams (N=27). Note: The label on each point is the Site # shown in Table 3.1

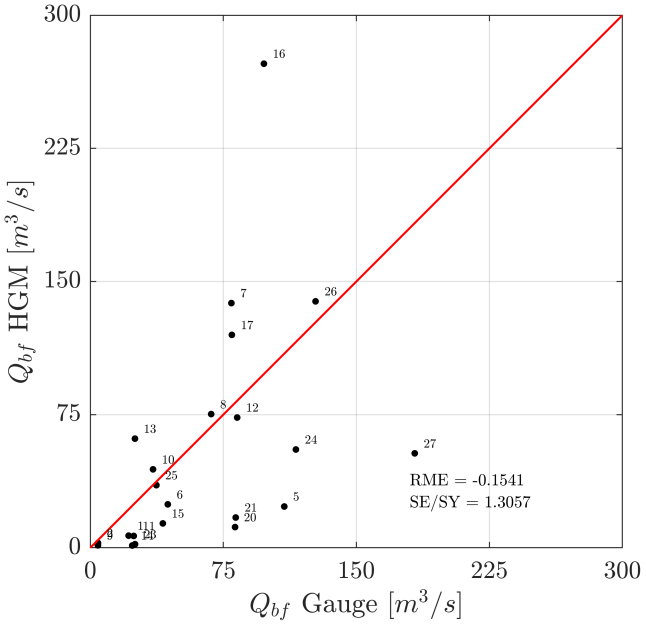

Figure 3.3: Computed and gauged bankfull discharge for low-order streams as defined by bankfull Width (N=22). Note: The label on each point is the Site # shown in Table 3.1

3.4.2 Predicted Discharge

The area-coefficients (Section 2.4) for identified bankfull sections were used to compute annual exceeding probability discharges for both gauged and predicted data. This approach identifies the geometry relevance on the parameter p, useful to identify breakpoints in the tetntative values.

Figure 3.4 displays the prediction results. The model showed poor SE/SY values but with consistent bias results in low-order streams. The extrapolation from the bankfull flow was computed for a maximum recurrence interval of 200 years, with a SE/SY value ranging between 1.57 and 1.90, indicating poor accuracy between predicted HGM and observed gauged data with a tendency to overpredict the discharges (Table 3.3). Even though the bias is low and remains below 15%, the accuracy of the predictions is poor for low-order streams. These is explained by a loss of precision when extrapolating to lower probability discharges, as seen in Figure 3.4.

Table 3.3: Model accuracy: Bankfull discharge (2-year) from HGM, other return periods from EVTI

T $[years]$	All Streams			Low-Order Streams		
	RME	RMSE $[m^3/s]$	RRMSE SE/SY	RME	RMSE $[m^3/s]$	RRMSE SE/SY
2	0.29	99.91	1.52	−0.15	59.14	1.31
5	0.56	192.68	2.03	0.00	105.11	1.57
10	0.65	255.67	2.23	0.06	137.05	1.68
20	0.71	316.46	2.37	0.09	168.08	1.75
50	0.76	395.41	2.50	0.12	208.52	1.82
100	0.79	454.68	2.57	0.14	238.95	1.86
200	0.82	513.79	2.63	0.15	269.33	1.90

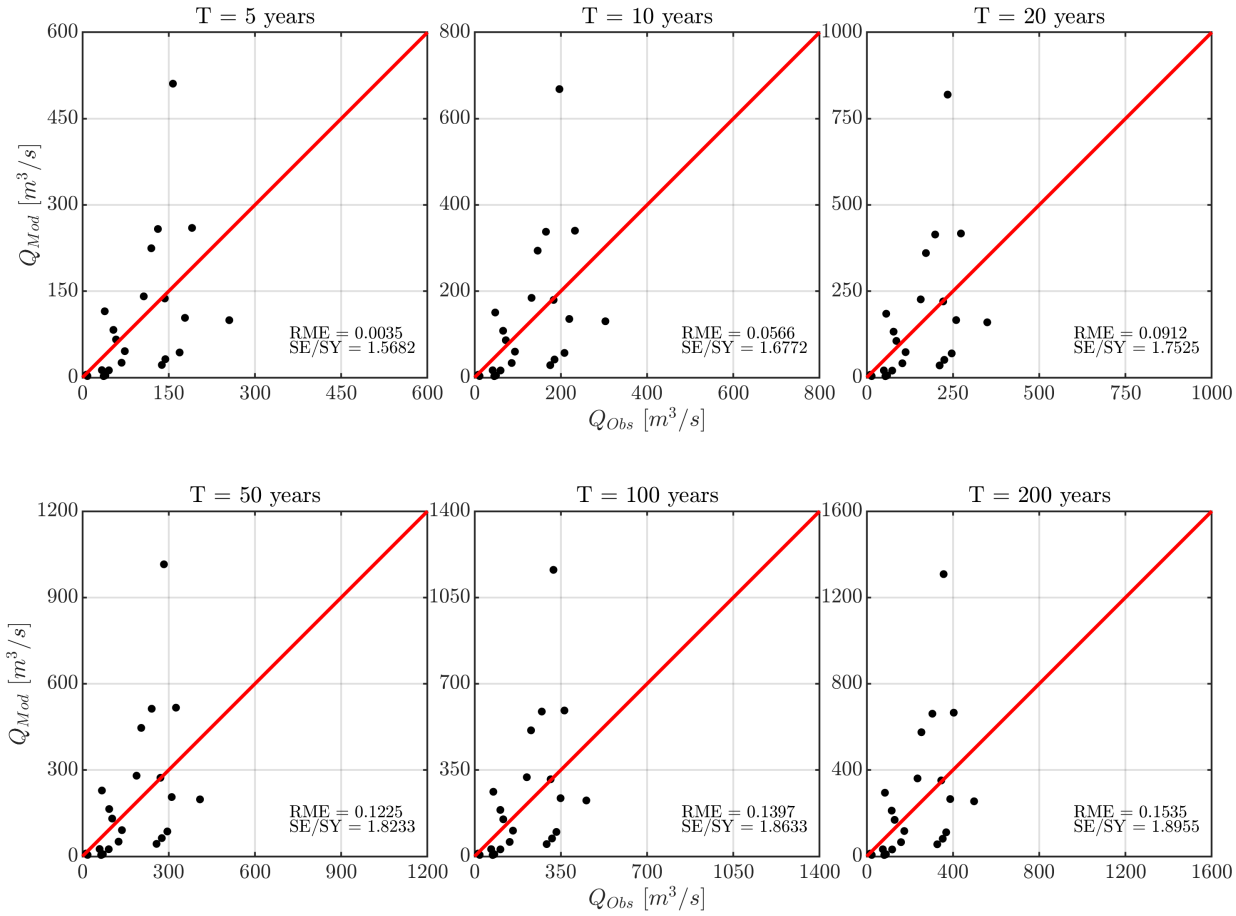

Figure 3.4: Discharge predictions for various return periods from gauge-based (Obs) and model-based (Mod) EVTI (low-order streams only, N=22)

3.5 Effect of Area-Exponent Assumption on Model Bias

When considering a constant Area-Exponent m (Eq. 1.3) and non-dimensional shear stress values, the error of the assumptions is introduced in the sole Area-Coefficient value. An analysis on the exponential value in the AHG equation shows that even though the exponential values change drastically, the steepest slope in the Area-Coefficient curve still shows the bankfull section with low bias for Area-Exponent (m) values between 0.5 and 0.8, which is in the range recommended by the literature (Figure 3.5). However, when moving away from those values the model accuracy drops in terms of both bias and precision.

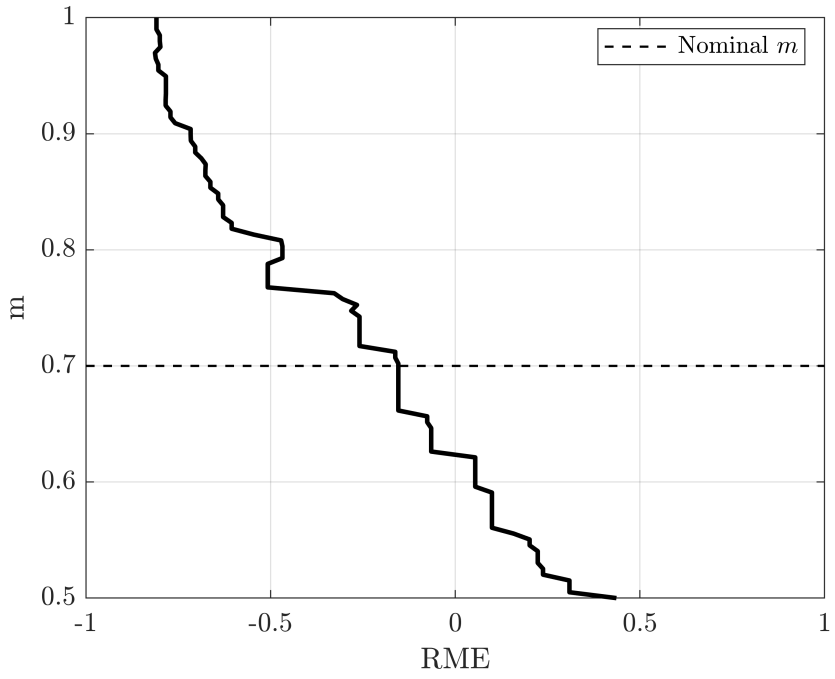

Figure 3.5: Area-exponent assumption effect on model bias (Relative Mean Error). Note: Nominal value of 0.70 (Leopold and Maddock, 1953) added for reference.

3.6 C_V Effect on Model Bias

A constant C_V was used to estimate the parameters for EVTI. An analysis on the effect of this assumption showed that (inside the standard deviation values of the C_V) the results are still acceptable. For each of the 22 locations analyzed, the relative mean error between the model-based and gauge-based EVTI was calculated (return periods from 2 to 200 by 1 year). The average of the 22 RME values lay in the range between -50% and +50% (Figure 3.6). This analysis could also explain that the variation between sites is not regional, and values between the previous range are valid for every site. Also, the lower the C_V assumed value the model tends to underpredict the results, this could explain a relationship between the variation in flow measurement and cross-section data.

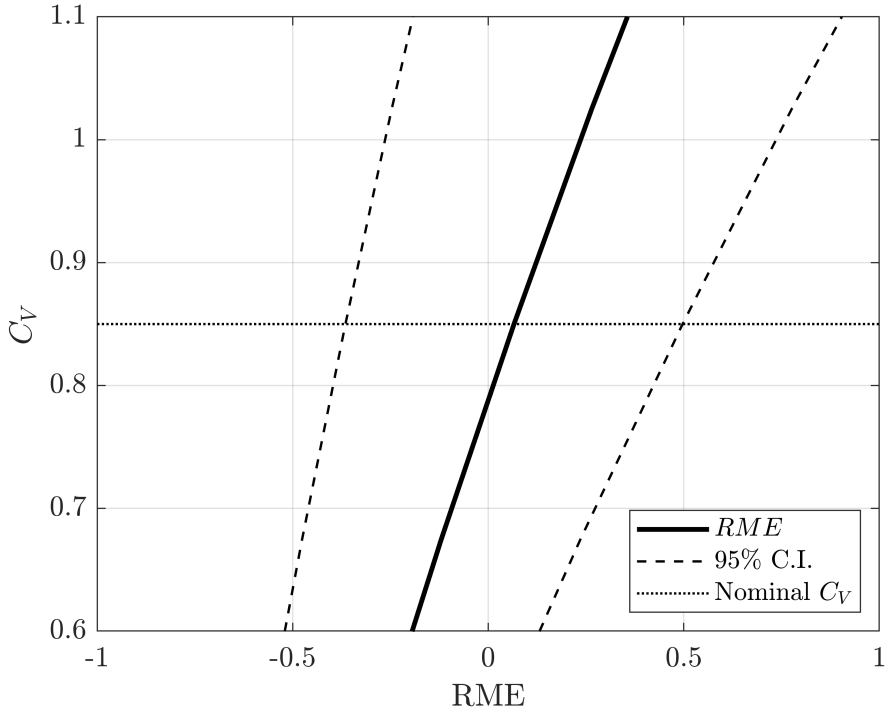

Figure 3.6: C_V value assumption effect on model bias. Note: Nominal value of 0.85 added for reference.

3.7 Effects of Bankfull Discharge Assumption on Model Bias

Assuming a bankfull discharge of 2-year return period is considered appropriate within the literature. The assumed bankfull return period ranged between 1.2 and 2.5 years. The relative mean error for various return periods between the model and the observed data (N=22) do change considerably. From 1.8 to 2.2 years of assumed bankfull return period the relative mean error ranges between -25% and +25%; values outside of this range are not recommended. Figure 3.7 displays the different bias values for each return period prediction when assuming a different bankfull return period (i.e., changing Eq. 2.5).

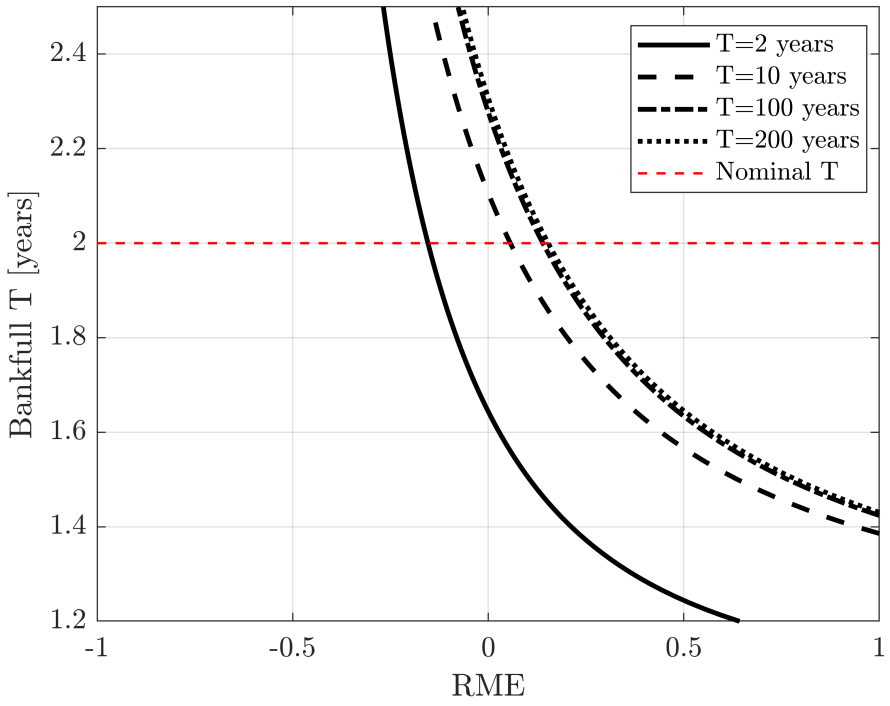

Figure 3.7: Bankfull return period assumptions effect on model bias. Note: Nominal value of T=2 years added for reference.

Chapter 4

Conclusions

4.1 Overview

The HGM discharge retrieval method advanced here yields reasonably unbiased retrievals of river discharge when derived solely from LiDAR data. The results show a non-systematic error ranging from 1.3 to 1.9, for both bankfull and predicted discharges, meaning that the precision is poor and gets worse for lower probability flows.

Users seeking to use this method in ungauged basins should adopt the assumptions described through this research, and carefully analyze the different recurrence interval outputs, as little variation in some of the assumptions can result in major deviations from the observed data. It is important to note that the reaches used for the model must remain mass conserved and free of tributaries or outflows, and users should avoid choosing reaches near receiving waters, confluences, and hydrologic controls (as these conditions can impact the cross section averaging and bankfull data). Rivers narrower than 90 meters are likely to be well retrieved from LiDAR data and are less susceptible to negligible baseflow assumptions. The recommended geomorphic criteria (low-order) is essential to implement a remote sensing elevation dataset into the model without bathymetric information, since otherwise when considering all the streams (low- and high-order) the accuracy for bankfull discharge is

worse.

This method can serve as a tool used prior to applying conventional hydrologic methods such as flow routing and regional regression equations, with values ranging between -50% and +50% compared with gauged streams. The HGM can easily give predictions to 200-year return period discharges in those streams where the bankfull cross-section is well defined and baseflow is not significant (in order to retrieve accurate topographic data).

A method that does not rely on roughness parameters and rainfall events changes the perspective as to how hydrologists estimate and predict discharge; this work aids to understand non-conventional and dynamic flow geomorphology. By considering all of the previous limitations, further research is needed to understand better the use of hydraulic geometry relations and the use of dependent data for hydrologic modeling.

4.2 Discussion and Limitations

The method is simple to apply, but it has a major cost. The large number of assumptions invokes unavoidable errors which have to be clarified in order to correctly use the HGM.

Bankfull section dynamics make this problem very hard to solve. It is very probable that the natural flow of the stream would dynamically change the shape of the bankfull cross section. When using dependent data for estimating discharge, one major assumption is that the bank is in equilibrium with the flow. Also, it is

possible for the streams' cross-sections to change in time due to human involvement. This dynamic change is not measured in this research, but it has to be taken into account when comparing sites having many years of data and/or urban development upstream. On the other hand, some tidal influence of low elevation streams can change the stream bed by deposition of fine particles.

When assuming negligible baseflow, the model is using water surface as bathymetry. This approach can work for channels with smaller sections and considerable low baseflow (as shown). But for bigger streams, the theory would not work unless bathymetric data is used. Fortunately, there are techniques that can potentially overcome this problem. For instance, the HawkEye technique (bathymetric LiDAR) uses a combination of NIR and green light that can provide both terrestrial and bathymetric topographic information (Bailly et al., 2010); however, this technique has a coarser resolution, which may limit potential usefulness, especially in small streams. Maybe using a merged approach between both datasets can have better estimates for low-order streams.

Gravel and sand bed distinction, only from slope, based on the concept that steeper flows transport more mass. This approach can be improved by considering other methods. For example a Rouse suspended sediment profile (Dietrich, 1982) can be used to categorize the stream bed, focusing on the predominant sediment size above the convergence point. Also, a region-based assumption of bed material is often correct since it reflects insight on ongoing sediment transport. Also, some considerations must be taken into account when implementing Strickler-type equations. These equations are recommended to use in wide-shallow channels where the

hydraulic radius can be replaced by the mean depth, and are not suitable when the bedform effect is predominant (Yen, 1992). Other major factor not taken into account is the presence of vegetation, which can be included to improve the Manning coefficient equations.

Averaging the cross-sections could change the characteristic section of the stream. This way the bias in the measurements of the LiDAR key points is reduced, but it also takes into account trends in elevation that can be caused by natural channel expansion or contraction. Also, using arbitrary cross sections can create some human bias by mistakenly choosing some wrong centerlines that are meandering or misaligned compared to the actual stream line. This latter concern can drastically change the average slope value and cause wrong site data retrieval. Also, the cross-section averaging method used in this research uses a fill-in function to improve the channel geometry configuration, but this can change the geometry parameters of the model by reducing the active section of the stream. To compensate for LiDAR error it is suggested to do a manual inspection of the sites and measure in-situ a representative cross-section.

This approach might also be beneficial in cases where stream morphology is changing over time and, thus, frequent updates of the rating curves are necessary (Nathanson et al., 2012). However, airborne LiDAR scanning today is still quite expensive. The high cost might be partially compensated for by the ease with which rating curves and stream monitoring could be performed even at remote locations using the methodology outlined in this study.

Using the abrupt change method certainly reduces the human bias of observing

and selecting a bankfull section, but it also must be used correctly. The increment depth used for each iteration in the calculation can lead to estimating the Area-Coefficient slope with very close or far away points. Therefore, an incremental depth value must be chosen that resembles the data length of the average cross section.

Correctly selecting and using the appropriate centerline and assumptions, respectively, can change drastically the outcome of the method. However, the approach used in this research demonstrate how using only in-situ remote sensed measurements it is possible to estimate and predict low probability discharge values to some extent. Finally, further research can be done by using a better elevation dataset, one that could read bathymetry, and by selecting more gauge data sites.

Appendix A

Streamflow and LiDAR Data

This appendix includes information about the data used as an input for this method. This information includes LiDAR data and USGS gauge information along with the data screening process. Also, the matlab and python code used in the process is attached at the end of the appendix.

A.1 Gauged Sites Data

The data was obtained from the NWIS. The data was retrieved on 2019-02-13 17:56:41 EST.

Some of the this data that may not have received NWIS Director's approval. Any such data values are qualified as provisional and are subject to revision. Provisional data are released on the condition that neither the USGS nor the United States Government may be held liable for any damages resulting from its use.

Table A.1: Gauge Data

#	Hydrologic Unit	Gauge Name	State	Years of Data	N
1	01484719	Bassett Creek Near Ironshire	MD	2003 - 2012	10
2	01485000	Pocomoke River Near Willards	MD	1950 - 2017	66
3	01485500	Nassawango Creek Near Snow Hill	MD	1950 - 2017	68
4	01486000	Manokin Branch Near Princess Anne	MD	1951 - 2016	64
5	01486100	Andrews Branch Near Delmar	MD	1967 - 1976	10
6	01486500	Beaverdam Creek Near Salisbury	MD	1930 - 2017	60
7	01489000	Faulkner Branch At Federalsburg	MD	1950 - 2011	43
8	01489500	Rewastico Creek Near Hebron	MD	1950 - 1960	9
9	01490000	Chicamacomico River Near Salem	MD	1951 - 2016	47
10	01490800	Oldtown Branch At Goldsboro	MD	1967 - 1976	10
11	01491000	Choptank River Near Greensboro	MD	1948 - 2017	70
12	01491050	Spring Branch Near Greensboro	MD	1967 - 1976	10

Continued on next page

#	Hydrologic Unit	Gauge Name	State	Years of Data	N (years)
13	01491500	Tuckahoe Creek Near Ruthsburg	MD	1951 - 2017	22
14	01492000	Beaverdam Branch At Matthews	MD	1950 - 2011	34
15	01492050	Gravel Run At Beulah	MD	1966 - 1975	11
16	01492500	Sallie Harris Creek Near Carmichael	MD	1952 - 2017	47
17	01492550	Mill Creek Near Skipton	MD	1966 - 1976	11
18	01493000	Unicorn Branch Near Millington	MD	1948 - 2017	69
19	01493112	Chesterville Branch Near Crumpton	MD	1996 - 2017	13
20	01493500	Morgan Creek Near Kennedyville	MD	1951 - 2017	66
21	01494000	Southeast Creek At Church Hill	MD	1952 - 1965	14
22	01494150	Three Bridges Branch At Centreville	MD	2007 - 2017	11
23	01494500	Jacobs Creek Near Sassafras	MD	1952 - 1956	5
24	01495000	Big Elk Creek At Elk Mills	MD	1884 - 2017	86
25	01495500	Little Elk Creek At Childs	MD	1949 - 1999	12
26	01495800	Long Creek Near Chesapeake City	MD	1979 - 1981	3
27	01496000	Northeast Creek At Leslie	MD	1949 - 1999	37
28	01496080	Northeast River Tributary Near Charlestown	MD	1967 - 1975	10
29	01496200	Principio Creek Near Principio Furnace	MD	1967 - 1999	27
30	01577940	Broad Creek Tributary At Whiteford	MD	1971 - 1985	16
31	01578310	Susquehanna River At Conowingo	MD	1968 - 2017	50
32	01578475	Octoraro Creek Near Richardsmere	MD	2006 - 2017	12
33	01578500	Octoraro Creek Near Rising Sun	MD	1884 - 1999	44
34	01578800	Basin Run At West Nottingham	MD	1967 - 1976	10
35	01579000	Basin Run At Liberty Grove	MD	1949 - 1999	23
36	01580000	Deer Creek At Rocks	MD	1926 - 2017	91
37	01580200	Deer Creek Near Kalmia	MD	1967 - 1977	11
38	01580520	Deer Creek Near Darlington	MD	2000 - 2017	18
39	01580700	Swan Creek At Swan Creek	MD	2008 - 2017	10
40	01581000	Bynum Run Near Bel Air	MD	1951 - 1955	5
41	01581500	Bynum Run At Bel Air	MD	1945 - 2017	43
42	01581649	James Run Near Belcamp	MD	2004 - 2017	13
43	01581657	Cranberry Rn At Aberdeen	MD	1988 - 1988	2
44	01581658	Cranberry Run At Perryman	MD	1987 - 1988	3
45	01581690	Bear Cabin Branch Near Bel Air	MD	2009 - 2009	1
46	01581700	Winters Run Near Benson	MD	1967 - 2017	51
47	01581750	Winters Run Hd Of Otter Pt Creek Near Bel Air	MD	2006 - 2017	5
48	01581752	Plumtree Run Near Bel Air	MD	2002 - 2017	16
49	01581757	Otter Point Creek Near Edgewood	MD	2000 - 2017	18
50	01581810	Gunpowder Falls At Hoffmanville	MD	2001 - 2017	17
51	01581830	Grave Run Near Beckleysville	MD	2000 - 2017	18
52	01581870	Georges Run Near Beckleysville	MD	2000 - 2017	18
53	01581920	Gunpowder Falls Near Parkton	MD	2000 - 2017	18
54	01581940	Mingo Branch Near Hereford	MD	2000 - 2009	10
55	01581960	Beetree Run At Bentley Springs	MD	2000 - 2017	18
56	01582000	Little Falls At Blue Mount	MD	1933 - 2017	74
57	01582500	Gunpowder Falls At Glencoe	MD	1978 - 2017	38
58	01582510	Piney Creek Near Hereford	MD	1966 - 1979	14
59	01583000	Slade Run Near Glyndon	MD	1948 - 2011	36
60	01583100	Piney Run At Dover	MD	1982 - 2017	28
61	01583495	Western Run Tributary At Western Run	MD	1967 - 1976	10
62	01583500	Western Run At Western Run	MD	1945 - 2017	73
63	01583570	Pond Branch At Oregon Ridge	MD	1984 - 2017	22
64	01583580	Baisman Run At Broadmoor	MD	1965 - 2017	31
65	01583600	Beaverdam Run At Cockeysville	MD	1956 - 2017	36
66	01583800	Long Quarter Branch At Lutherville	MD	2014 - 2017	4
67	01583980	Minebank Run At Loch Raven	MD	1997 - 2004	9

Continued on next page

#	Hydrologic Unit	Gauge Name	State	Years of Data	N (years)
68	01584000	Gunpowder Falls Near Carney	MD	1950 - 1964	15
69	01584050	Long Green Creek At Glen Arm	MD	1976 - 2017	42
70	01584500	Little Gunpowder Falls At Laurel Brook	MD	1926 - 2017	77
71	01585075	Foster Branch Near Joppatowne	MD	2015 - 2017	2
72	01585090	Whitemarsh Run Near Fullerton	MD	1995 - 2017	23
73	01585095	North Fork Whitemarsh Run Near White Marsh	MD	1992 - 2009	17
74	01585100	Whitemarsh Run At White Marsh	MD	1960 - 2017	56
75	01585104	Honeygo Run Near White Marsh	MD	2000 - 2017	18
76	01585105	Honeygo Run At White Marsh	MD	1991 - 1993	3
77	01585107	Windlass Run Near White Marsh	MD	1992 - 1993	2
78	01585140	West Branch Canal Cr At Aberdeen Proving Groun	MD	2000 - 2000	1
79	01585200	West Branch Herring Run At Idlewylde	MD	1958 - 2017	51
80	01585219	Herring Run At Sinclair Lane At Baltimore	MD	2014 - 2017	4
81	01585225	Moores Run Trib. Near Todd Ave At Baltimore	MD	1997 - 2017	21
82	01585230	Moores Run At Radecke Ave At Baltimore	MD	1997 - 2017	21
83	01585300	Stemmers Run At Rossville	MD	1960 - 1989	29
84	01585400	Brien Run At Stemmers Run	MD	1959 - 1986	29
85	01585500	Cranberry Branch Near Westminster	MD	1949 - 2017	69
86	01586000	North Branch Patapsco River At Cedarhurst	MD	1946 - 2017	72
87	01586210	Beaver Run Near Finksburg	MD	1983 - 2017	35
88	01586500	North Branch Patapsco River Near Reisterstown	MD	1928 - 1952	26
89	01586610	Morgan Run Near Louisville	MD	1983 - 2017	35
90	01587000	North Branch Patapsco Riv Near Marriottsville	MD	1929 - 1960	31
91	01587050	Haymeadow Branch Tributary At Poplar Springs	MD	1966 - 1976	11
92	01587500	South Branch Patapsco River At Henryton	MD	1949 - 1979	32
93	01588000	Piney Run Near Sykesville	MD	1932 - 1974	43
94	01588500	Patapsco River At Woodstock	MD	1897 - 1908	10
95	01589000	Patapsco River At Hollofield	MD	1933 - 2017	61
96	01589025	Patapsco River Near Catonsville	MD	2011 - 2017	7
97	01589035	Patapsco River Near Elkridge	MD	2011 - 2017	7
98	01589100	East Branch Herbert Run At Arbutus	MD	1956 - 2017	52
99	01589180	Gwynns Falls At Glyndon	MD	1999 - 2017	19
100	01589197	Gwynns Falls Near Delight	MD	1999 - 2017	19
101	01589200	Gwynns Falls Near Owings Mills	MD	1959 - 1975	17
102	01589238	Gwynns Falls Tributary At Mcdonogh	MD	1999 - 2017	18
103	01589240	Gwynns Falls At Mcdonogh	MD	1958 - 1984	21
104	01589290	Scotts Level Branch At Rockdale	MD	2006 - 2017	12
105	01589300	Gwynns Falls At Villa Nova	MD	1956 - 2017	54
106	01589305	Powder Mill Run Near Lochearn	MD	2006 - 2017	12
107	01589312	Dead Run Near Catonsville	MD	2008 - 2017	10
108	01589315	Dead Run At Woodlawn	MD	2008 - 2017	10
109	01589316	Dead Run Tributary Near Woodlawn	MD	2008 - 2017	10
110	01589317	Tributary To Dead Run Tributary At Woodlawn	MD	2008 - 2017	10
111	01589320	Dead Run Tributary At Woodlawn	MD	2008 - 2017	10
112	01589330	Dead Run At Franklintown	MD	1960 - 2017	47
113	01589340	Rognel Hgts Storm Sewer Outfall At Baltimore	MD	1999 - 2010	12
114	01589351	Maidens Choice Run At Wilkens Ave At Baltimore	MD	2001 - 2005	4
115	01589352	Gwynns Falls At Washington Blvd At Baltimore	MD	1999 - 2017	19
116	01589440	Jones Falls At Sorrento	MD	1958 - 2017	52
117	01589464	Stony Run At Ridgemede Road At Baltimore	MD	2004 - 2015	12
118	01589478	Jones Falls At Maryland Ave At Baltimore	MD	1981 - 2004	7
119	01589480	Jones Falls Near Mouth At Baltimore	MD	1981 - 1982	2
120	01589500	Sawmill Creek At Glen Burnie	MD	1933 - 2017	49
121	01589501	Sawmill Creek Tributary At Bwi Near Ferndale	MD	1995 - 2003	8
122	01589512	Sawmill Creek At Crain Hwy At Glen Burnie	MD	1984 - 1994	6

Continued on next page

#	Hydrologic Unit	Gauge Name	State	Years of Data	N (years)
123	01589522	Marley Creek At Harundale	MD	1984 - 1985	2
124	01589795	South Fork Jabez Branch At Millersville	MD	1990 - 2017	22
125	01590000	North River Near Annapolis	MD	1932 - 1973	43
126	01590500	Bacon Ridge Branch At Chesterfield	MD	1944 - 1990	35
127	01591000	Patuxent River Near Unity	MD	1945 - 2017	73
128	01591350	Cattail Creek Near Cooksville	MD	1978 - 1981	4
129	01591400	Cattail Creek Near Glenwood	MD	1979 - 2017	39
130	01591500	Cattail Creek At Roxbury Mills	MD	1945 - 1956	12
131	01591610	Patuxent River Below Brighton Dam Near Brighto	MD	1972 - 2017	38
132	01591700	Hawlings River Near Sandy Spring	MD	1979 - 2017	39
133	01592000	Patuxent River Near Burtonsville	MD	1911 - 1944	34
134	01592500	Patuxent Riv Near Laurel	MD	1945 - 2017	73
135	01593350	Little Patuxent River Trib. At Guilford Downs	MD	1966 - 1976	11
136	01593370	L Pax Riv Trib Above Wilde Lake At Columbia	MD	2013 - 2017	5
137	01593450	L Pax Riv Trib Above Lake Elkhorn Nr Guilford	MD	2013 - 2017	5
138	01593500	Little Patuxent River At Guilford	MD	1933 - 2017	85
139	01593710	Middle Patuxent River Near Simpsonville	MD	1986 - 1995	9
140	01594000	Little Patuxent River At Savage	MD	1933 - 2017	68
141	01594400	Dorsey Run Near Jessup	MD	1949 - 2009	20
142	01594440	Patuxent River Near Bowie	MD	1972 - 2017	41
143	01594445	Mill Branch Near Mitchellville	MD	1966 - 1976	11
144	01594500	Western Branch Near Largo	MD	1950 - 1974	25
145	01594526	Western Branch At Upper Marlboro	MD	1985 - 2017	29
146	01594600	Cocktown Creek Near Huntingtown	MD	1958 - 1976	19
147	01594670	Hunting Creek Near Huntingtown	MD	1989 - 1998	10
148	01594710	Killpeck Creek At Huntersville	MD	1986 - 1996	12
149	01594800	St Leonard Creek Near St Leonard	MD	1958 - 2003	14
150	01594930	Laurel Run At Dobbin Rd Near Wilson	MD	1980 - 2004	26
151	01594934	South Fork Sand Run Near Wilson	MD	1980 - 1985	7
152	01594936	North Fork Sand Run Near Wilson	MD	1980 - 2007	28
153	01594950	Mcmillan F Near Fort Pendleton	MD	1987 - 2017	31
154	01594963	Nydegger Run Near Gorman	MD	2013 - 2016	4
155	01595000	North Branch Potomac River At Steyer	MD	1954 - 2017	63
156	01595500	North Branch Potomac River At Kitzmiller	MD	1950 - 2017	67
157	01596005	Savage River Near Frostburg	MD	1971 - 1985	14
158	01596050	Savage River Near Avilton	MD	2013 - 2016	4
159	01596500	Savage River Near Barton	MD	1948 - 2017	69
160	01597000	Crabtree Creek Near Swanton	MD	1949 - 2016	36
161	01597500	Savage Riv Bl Savage Riv Dam Near Bloomington	MD	1949 - 2017	69
162	01598000	Savage River At Bloomington	MD	1924 - 1950	25
163	01598500	North Branch Potomac River At Luke	MD	1900 - 2017	77
164	01598650	Sand Spring Run At Frostburg	MD	2006 - 2008	2
165	01599000	Georges Creek At Franklin	MD	1924 - 2017	88
166	01601100	Wills Creek At Ellerslie	MD	2012 - 2015	3
167	01601420	Hoffman Drainage Tunnel At Clarysville	MD	2016 - 2017	2
168	01601500	Wills Creek Near Cumberland	MD	1924 - 2017	89
169	01603000	North Branch Potomac River Near Cumberland	MD	1889 - 2017	90
170	01609000	Town Creek Near Oldtown	MD	1928 - 2017	38
171	01609500	Sawpit Run Near Oldtown	MD	1948 - 1975	25
172	01610000	Potomac River At Paw Paw	WV	1877 - 2017	84
173	01610105	Pratt Hollow Tr At Pratt	MD	1971 - 1986	15
174	01610150	Bear Creek At Forest Park	MD	1965 - 1983	18
175	01610155	Sideling Hill Creek Near Bellegrove	MD	1968 - 2017	29
176	01612500	Little Tonoloway Creek Near Hancock	MD	1948 - 1964	17
177	01613000	Potomac River At Hancock	MD	1889 - 2017	88

Continued on next page

#	Hydrologic Unit	Gauge Name	State	Years of Data	N (years)
178	01613095	Tonoloway Creek Near Hancock	MD	2006 - 2017	12
179	01613150	Ditch Run Near Hancock	MD	1965 - 1985	22
180	01613160	Potomac River Tributary Near Hancock	MD	1965 - 1976	12
181	01613525	Licking Creek At Pectonville	MD	2005 - 2017	13
182	01614500	Conococheague Creek At Fairview	MD	1889 - 2017	91
183	01617800	Marsh Run At Grimes	MD	1964 - 2017	54
184	01619000	Antietam Creek Near Waynesboro	PA	1949 - 2017	32
185	01619320	Alb. Powell Fish Hatchery Sp. At Beaver Creek	MD	1989 - 1998	10
186	01619475	Dog Creek Tributary Near Locust Grove	MD	1966 - 1976	11
187	01619500	Antietam Creek Near Sharpsburg	MD	1928 - 2017	90
188	01636845	Little Catoctin Creek Near Rosemont	MD	2017 - 2017	1
189	01636846	Little Catoctin Creek At Rosemont	MD	2017 - 2017	1
190	01637000	Little Catoctin Creek At Harmony	MD	1948 - 1976	30
191	01637500	Catoctin Creek Near Middletown	MD	1948 - 2017	70
192	01637600	Hollow Road Creek Near Middletown	MD	1965 - 1976	11
193	01638500	Potomac River At Point Of Rocks	MD	1889 - 2017	124
194	01639000	Monocacy River At Bridgeport	MD	1933 - 2017	77
195	01639095	Piney Creek Tributary At Taneytown	MD	1967 - 1976	10
196	01639140	Piney Creek Near Taneytown	MD	1990 - 2002	12
197	01639375	Toms Creek At Emmitsburg	MD	1986 - 1996	6
198	01639500	Big Pipe Creek At Bruceville	MD	1948 - 2017	70
199	01640000	Little Pipe Creek At Avondale	MD	1948 - 1979	31
200	01640500	Owens Creek At Lantz	MD	1932 - 1984	53
201	01640700	Owens Creek Tributary Near Rocky Ridge	MD	1967 - 1976	11
202	01640965	Hunting Creek Near Foxville	MD	1982 - 1993	13
203	01640970	Hunting Creek Tributary Near Foxville	MD	1982 - 1990	10
204	01640975	Hunting Creek Near Thurmont	MD	1983 - 1985	4
205	01640980	Bear Branch Near Thurmont	MD	1990 - 1995	5
206	01641000	Hunting Creek At Jimtown	MD	1950 - 1991	43
207	01641500	Fishing Creek Near Lewistown	MD	1948 - 2011	39
208	01641510	Fishing Creek Tributary Near Lewistown	MD	1988 - 1995	8
209	01642000	Monocacy River Near Frederick	MD	1889 - 1929	35
210	01642190	Monocacy River At Monocacy Blvd At Frederick	MD	2003 - 2017	14
211	01642400	Dollyhyde Creek At Libertytown	MD	1967 - 1976	10
212	01642438	Linganore Creek Near Libertytown	MD	2008 - 2010	3
213	01642500	Linganore Creek Near Frederick	MD	1933 - 1982	50
214	01643000	Monocacy River At Jug Bridge Near Frederick	MD	1889 - 2017	89
215	01643395	Soper Branch At Hyattstown	MD	2004 - 2017	14
216	01643495	Bennett Creek Tributary At Park Mills	MD	1992 - 1993	2
217	01643500	Bennett Creek At Park Mills	MD	1948 - 2017	68
218	01644371	Little Seneca Creek Tributary Near Clarksburg	MD	2004 - 2017	14
219	01644372	Little Seneca Creek Tributary At Brink	MD	2005 - 2017	13
220	01644375	Little Seneca Creek Tributary Near Germantown	MD	2004 - 2017	14
221	01644380	Cabin Branch Near Boyds	MD	2004 - 2017	14
222	01644388	Tenmile Creek Near Clarksburg	MD	2014 - 2017	4
223	01644390	Tenmile Creek Near Boyds	MD	2011 - 2017	7
224	01644420	Bucklodge Branch Tributary Near Barnesville	MD	1967 - 1976	10
225	01644500	Great Seneca Creek Near Gaithersburg	MD	1926 - 1929	5
226	01644600	Great Seneca Creek Near Quince Orchard	MD	1998 - 2009	12
227	01645000	Seneca Creek At Dawsonville	MD	1931 - 2017	87
228	01645200	Watts Branch At Rockville	MD	1958 - 1987	30
229	01646500	Potomac River Near Wash, Dc Little Falls Pump	TA	1931 - 2017	87
230	01646550	Little Falls Branch Near Bethesda	MD	1945 - 1984	40
231	01647685	Williamsburg Run Near Olney	MD	1967 - 1974	8
232	01647720	North Branch Rock Creek Near Norbeck	MD	1967 - 1977	11

Continued on next page

#	Hydrologic Unit	Gauge Name	State	Years of Data	N (years)
233	01647725	Manor Run Near Norbeck	MD	1967 - 1974	8
234	01647740	North Branch Rock Creek Near Rockville	MD	1968 - 1977	10
235	01647850	Turkey Branch Near Rockville	MD	2007 - 2017	11
236	01649150	Paint Branch Tributary Near Colesville	MD	2006 - 2017	11
237	01649190	Paint Branch Near College Park	MD	2008 - 2017	10
238	01649500	Northeast Branch Anacostia River At Riverdale	MD	1933 - 2017	80
239	01650050	Nw Branch Anacostia River At Norwood	MD	1967 - 1976	10
240	01650085	Nursery Run At Cloverly	MD	1967 - 1976	10
241	01650190	Batchellors Run At Oakdale	MD	1967 - 1976	10
242	01650450	Bel Pre Creek At Layhill	MD	1967 - 1974	8
243	01650500	Northwest Branch Anacostia River Nr Colesville	MD	1924 - 2017	80
244	01650800	Sligo Creek Near Takoma Park	MD	2009 - 2017	9
245	01651000	Northwest Br Anacostia River Nr Hyattsville	MD	1933 - 2017	80
246	01653500	Henson Creek At Oxon Hill	MD	1948 - 1978	30
247	01653600	Piscataway Creek At Piscataway	MD	1966 - 2017	51
248	01658000	Mattawoman Creek Near Pomonkey	MD	1950 - 2017	54
249	01660900	Wolf Den Branch Near Cedarville	MD	1967 - 1979	14
250	01660920	Zekiah Swamp Run Near Newtown	MD	1984 - 2017	33
251	01660930	Clark Rn Nr Bel Alton	MD	1966 - 1976	11
252	01661000	Chaptico Creek At Chaptico	MD	1948 - 1972	25
253	01661050	St Clement Creek Near Clements	MD	1969 - 2017	48
254	01661430	Glebe Branch At Valley Lee	MD	1968 - 1978	11
255	01661500	St Marys River At Great Mills	MD	1947 - 2017	70
256	03075450	Little Youghiogheny River Trib. At Deer Park	MD	1965 - 1975	12
257	03075500	Youghiogheny River Near Oakland	MD	1936 - 2017	77
258	03075600	Toliver Run Tributary Near Hoyes Run	MD	1965 - 1985	22
259	03075800	Poland Run Near Swanton	MD	2008 - 2012	5
260	03075825	North Glade Run Near Swanton	MD	2017 - 2017	1
261	03075850	Arrowhead Run At Thayerville	MD	2017 - 2017	1
262	03075905	Cherry Creek At State Park Road Near Mchenry	MD	2008 - 2017	9
263	03076100	Youghiogheny River At Hoyes	MD	2011 - 2017	7
264	03076500	Youghiogheny River At Friendsville	MD	1899 - 2017	94
265	03076505	Youghiogheny River Tributary Near Friendsville	MD	1965 - 1975	12
266	03076600	Bear Creek At Friendsville	MD	1965 - 2017	53
267	03076700	Buffalo Run Near Friendsville	MD	2013 - 2016	4
268	03076800	Mill Run At Mineral Spring	MD	2013 - 2016	4
269	03077700	North Branch Casselman River Trib. At Foxtown	MD	1965 - 1975	12
270	03077940	South Branch Casselman River Near Bittinger	MD	1977 - 1981	5
271	03078000	Casselman River At Grantsville	MD	1948 - 2017	69
272	14847130	Birch Branch At Showell	MD	2000 - 2017	18
273	15817530	Wheel Creek Near Abingdon	MD	2010 - 2017	8
274	15839797	Minebank Run Near Glen Arm	MD	2002 - 2017	16
275	15893510	Gwynns Run At Baltimore	MD	2001 - 2004	3

A.2 LiDAR Data

LiDAR data has been downloaded from the iMAP service of the state of Maryland, publicly available for each county at acceptable resolution (less than 1m x 1m). The data is offered in many classifications, like keypoints, ground, bridge deck, etc. For this research, ground and water classifications were used.

Ground classification routine removes any non-ground points and generate an accurate ground surface. The ground routine consists of three main parameters (building size, iteration angle, and iteration distance); by adjusting these parameters and running several iterations of this routine a ground surface is developed. The water classification routine selects ground points within the water breakline polygons and automatically classifies them as water. This hydrologic breaklines are collected to define as what is called the hydro-flattening phase. Since LiDAR does not collect bathymetry points, the ground points in the stream bed are actually water surface points. These points can be defined as baseflow and will be overwrited with the so called "water" points (flat base flow elevation) for this research. The average cross section was extracted and plotted along with the LiDAR elevation keypoints.

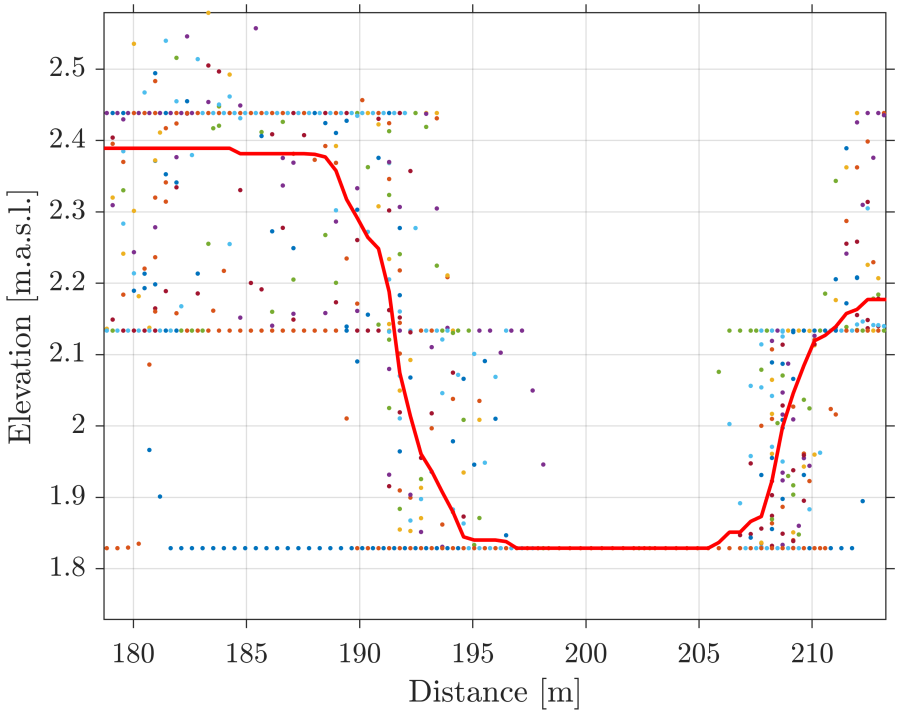

Figure A.1: Average Cross-Section Site #1

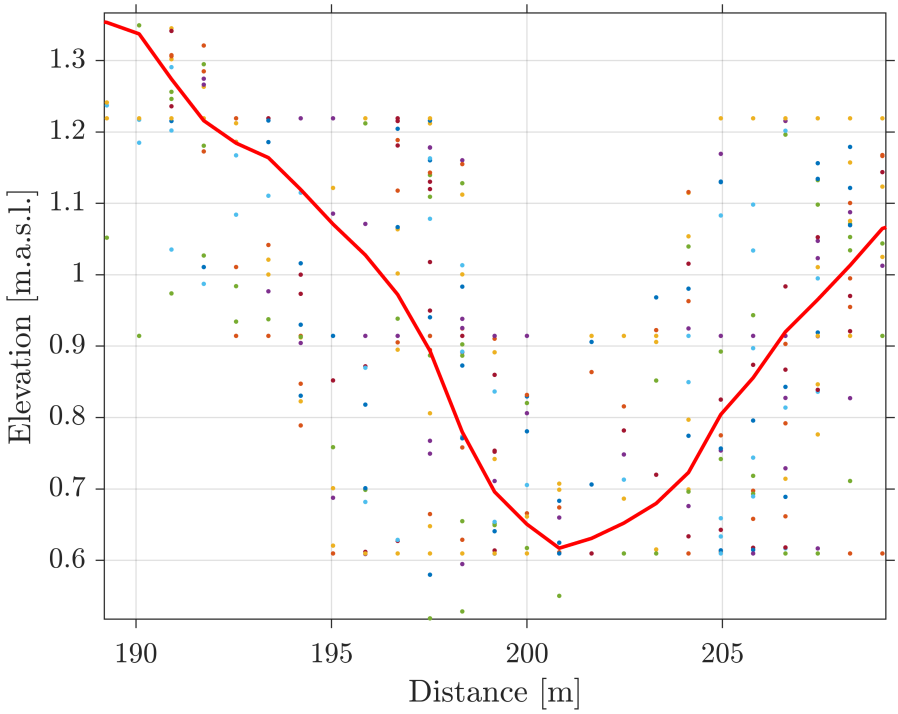

Figure A.2: Average Cross-Section Site #2

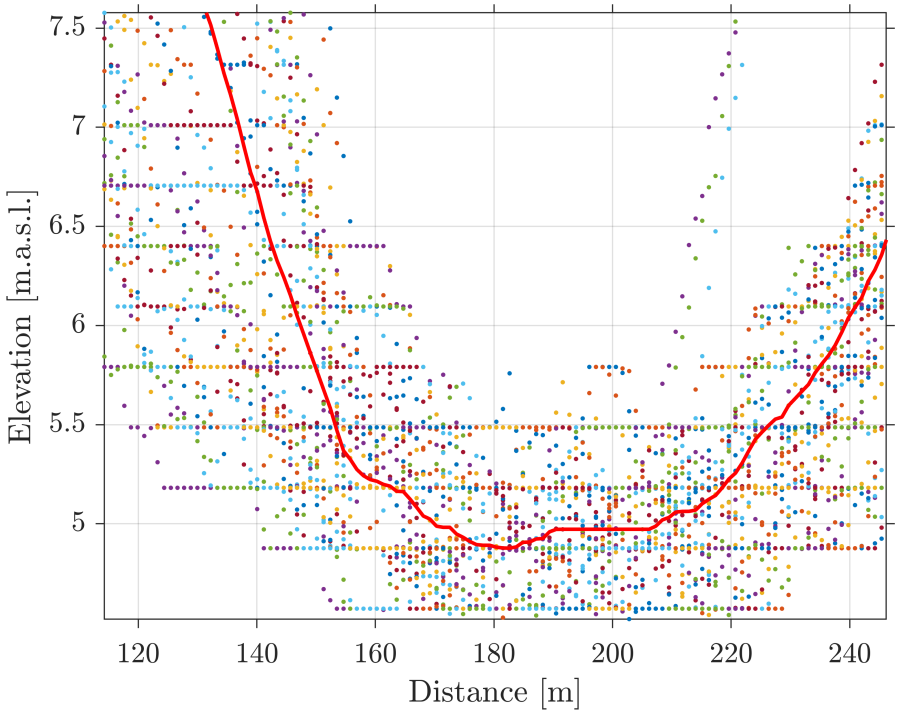

Figure A.3: Average Cross-Section Site #3

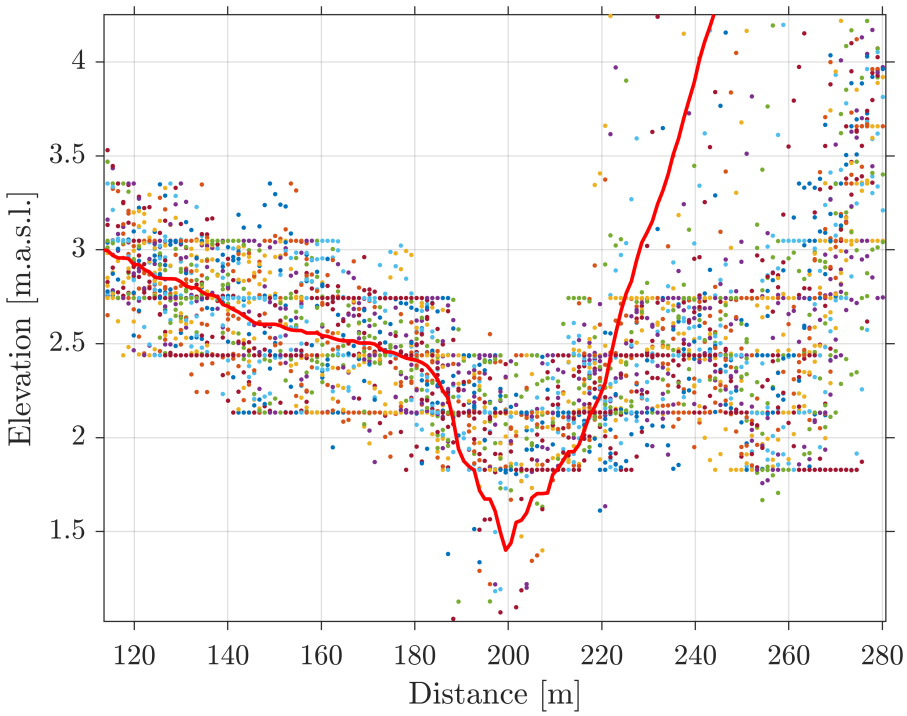

Figure A.4: Average Cross-Section Site #4

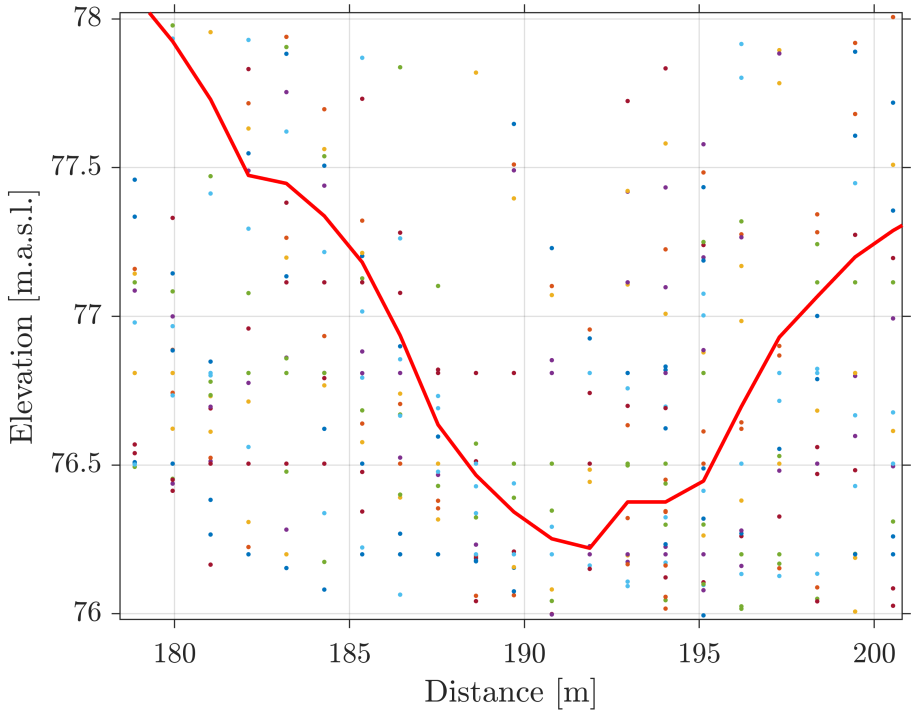

Figure A.5: Average Cross-Section Site #5

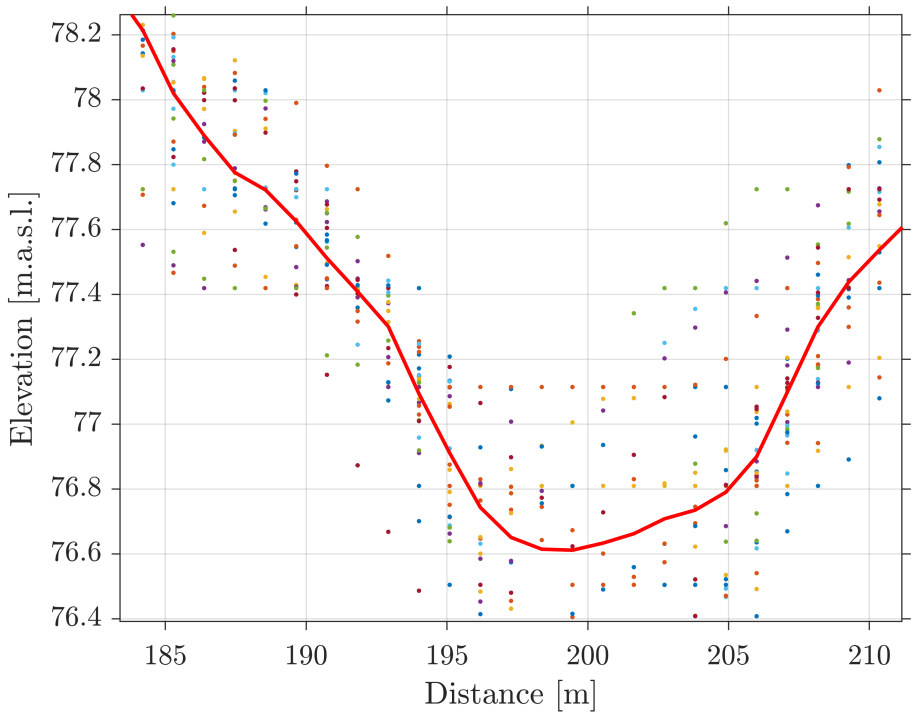

Figure A.6: Average Cross-Section Site #6

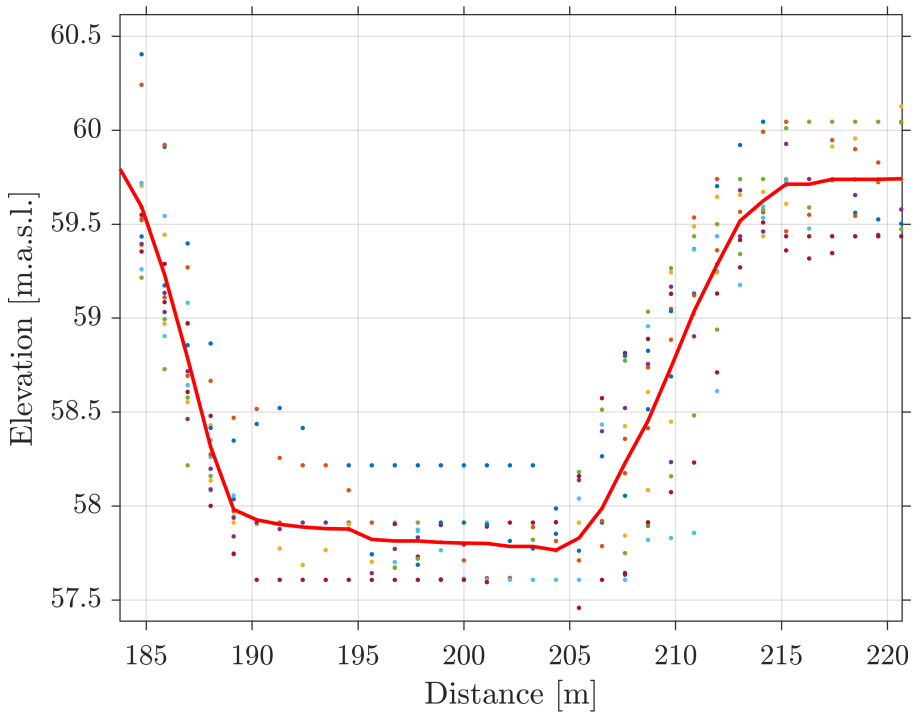

Figure A.7: Average Cross-Section Site #7

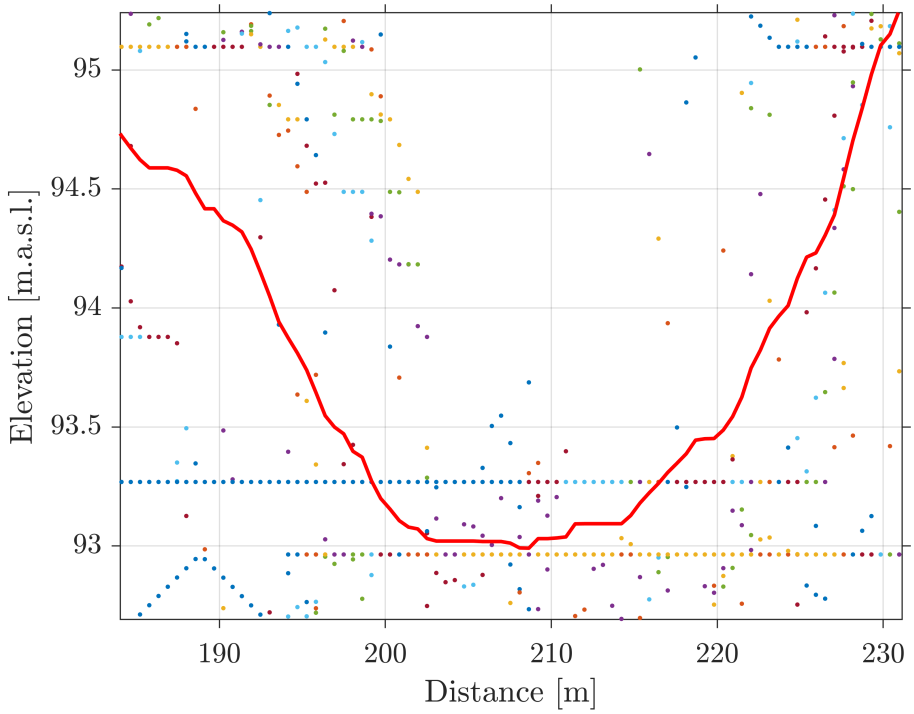

Figure A.8: Average Cross-Section Site #8

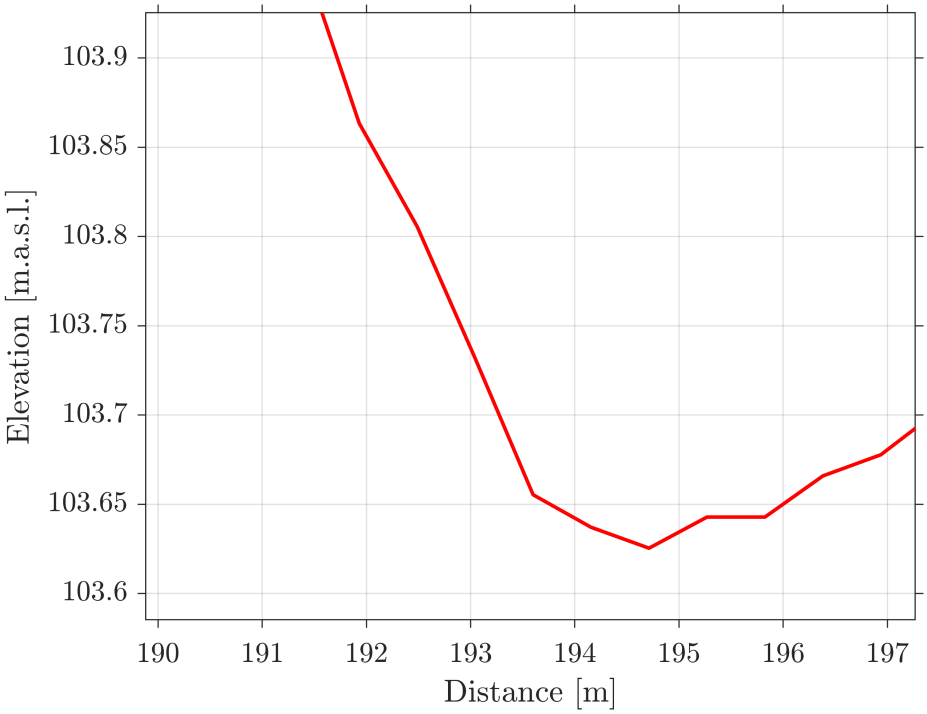

Figure A.9: Average Cross-Section Site #9

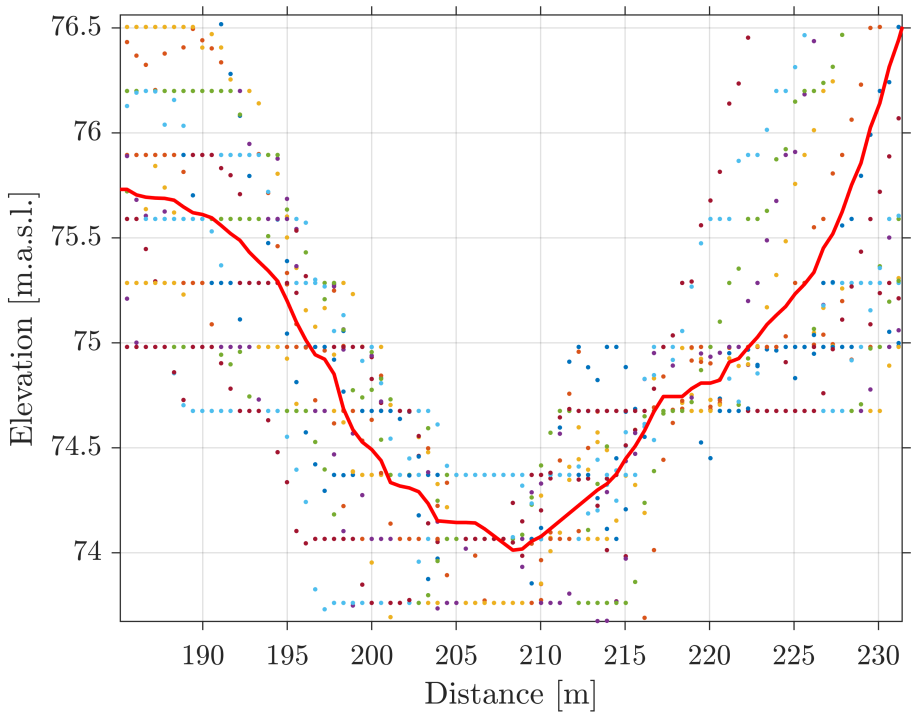

Figure A.10: Average Cross-Section Site #10

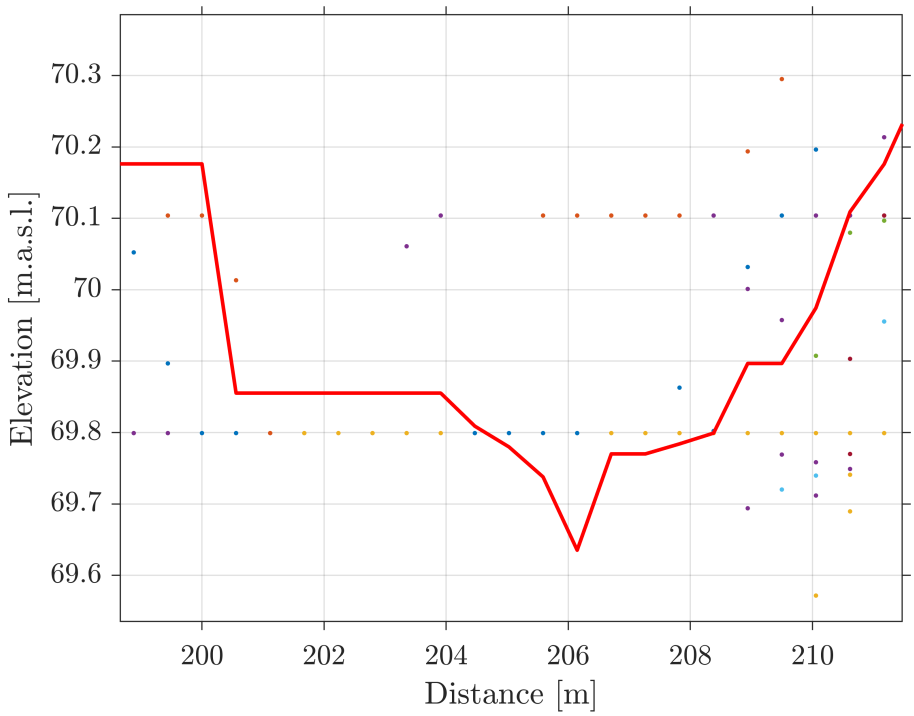

Figure A.11: Average Cross-Section Site #11

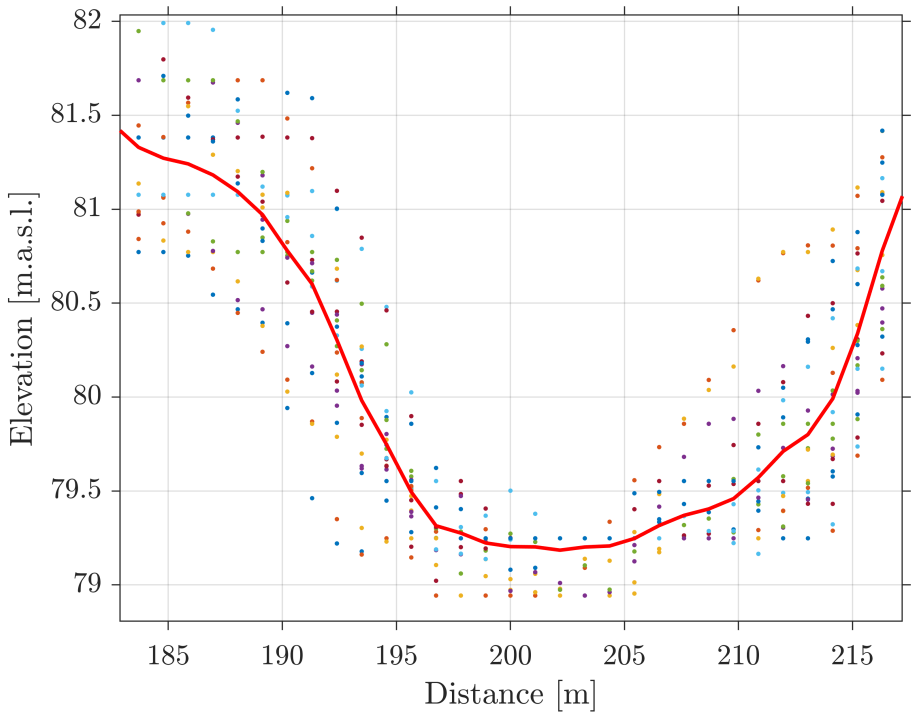

Figure A.12: Average Cross-Section Site #12

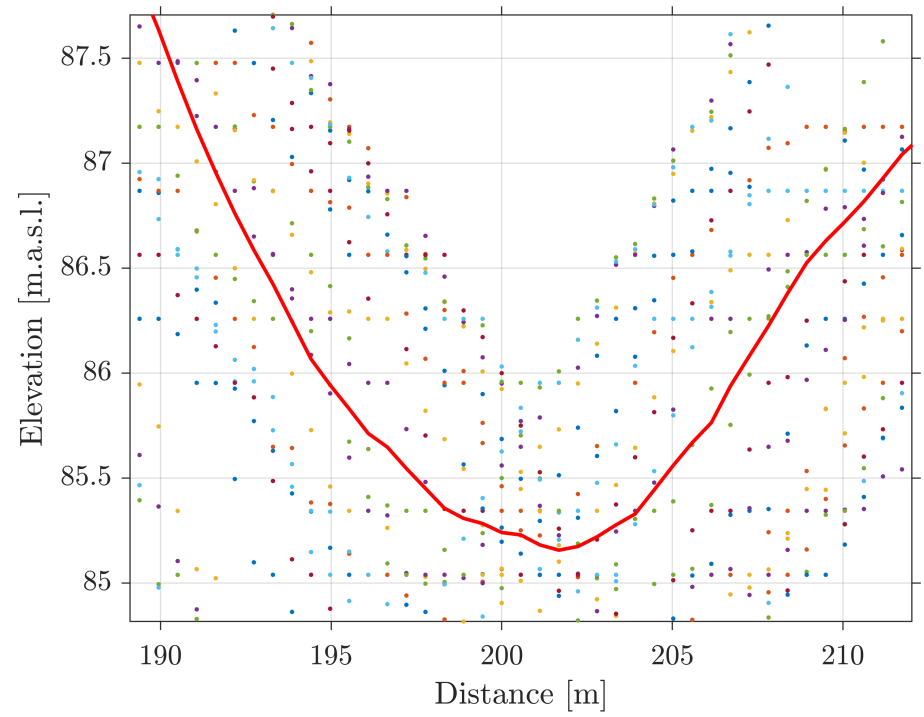

Figure A.13: Average Cross-Section Site #13

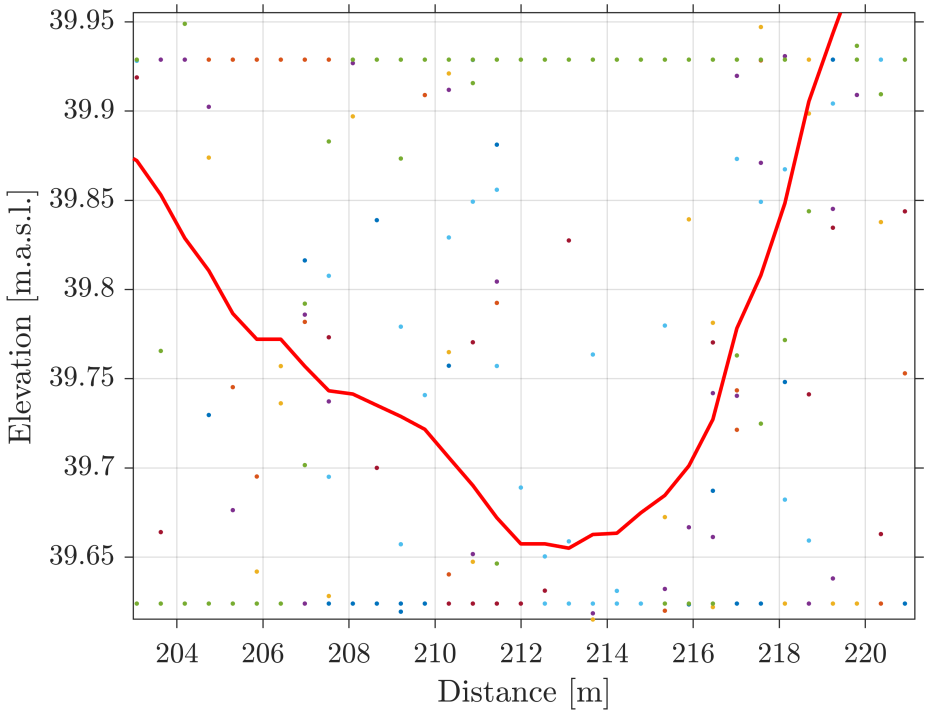

Figure A.14: Average Cross-Section Site #14

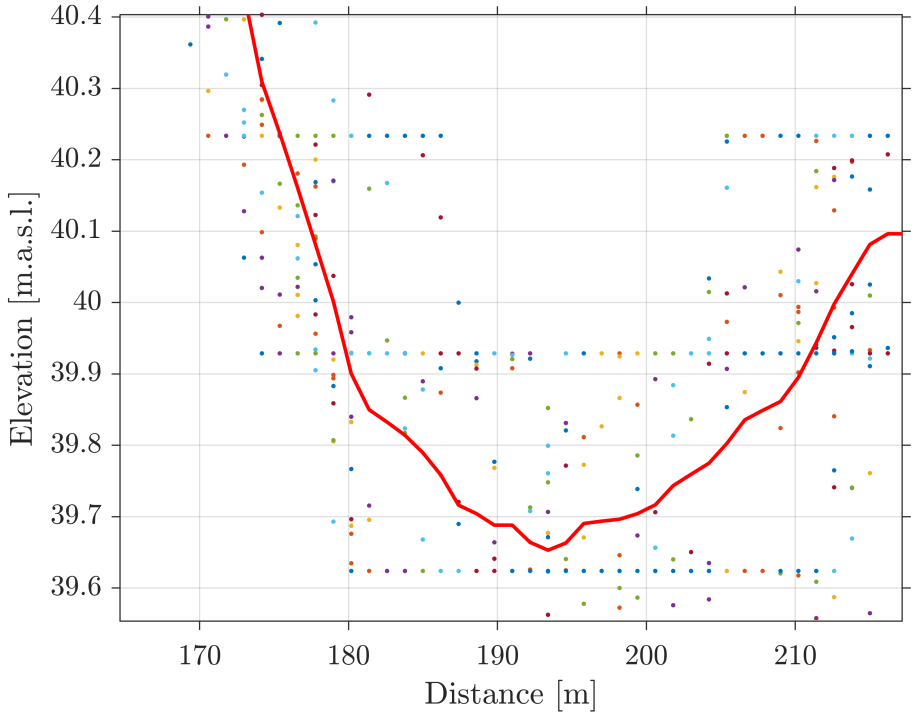

Figure A.15: Average Cross-Section Site #15

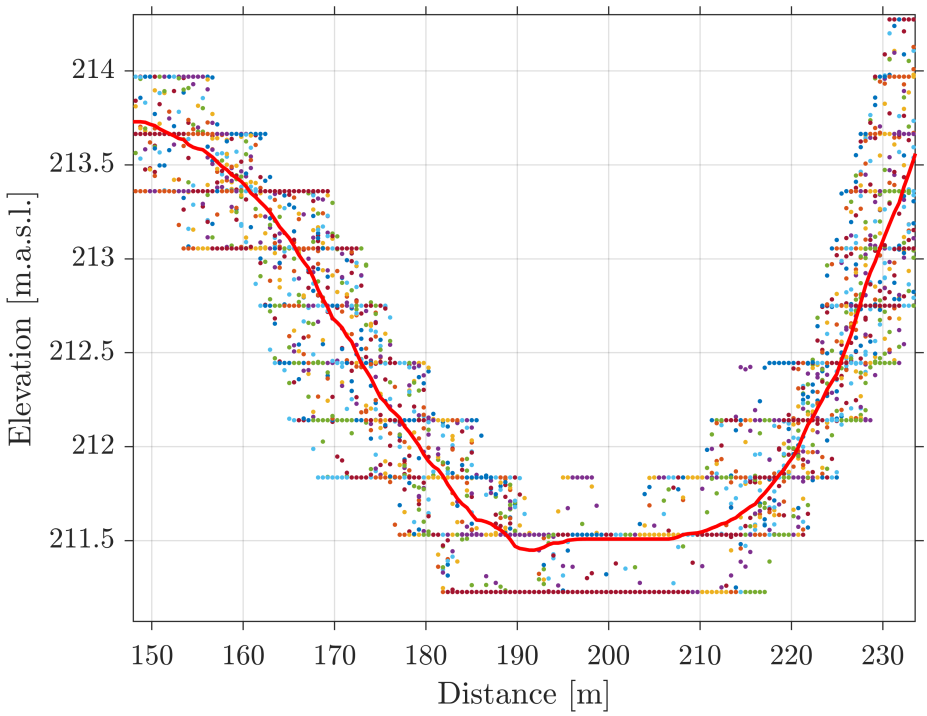

Figure A.16: Average Cross-Section Site #16

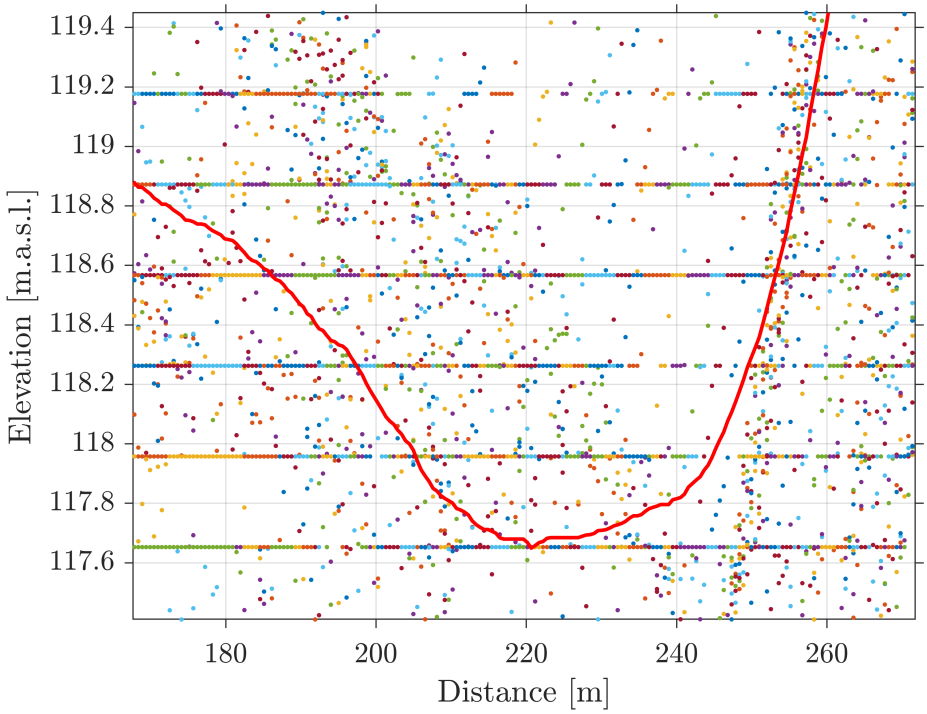

Figure A.17: Average Cross-Section Site #17

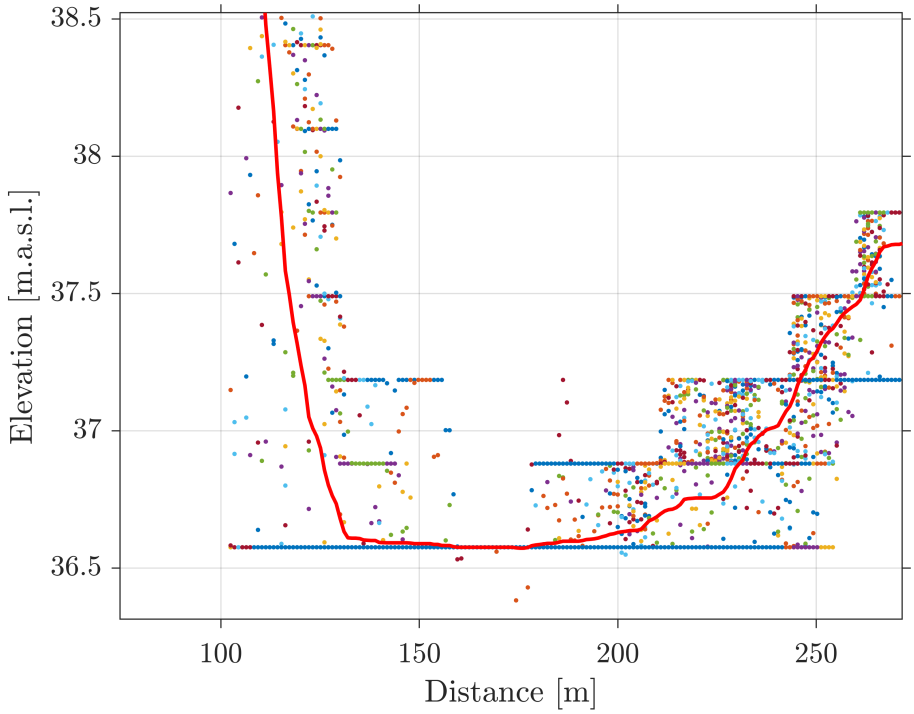

Figure A.18: Average Cross-Section Site #18

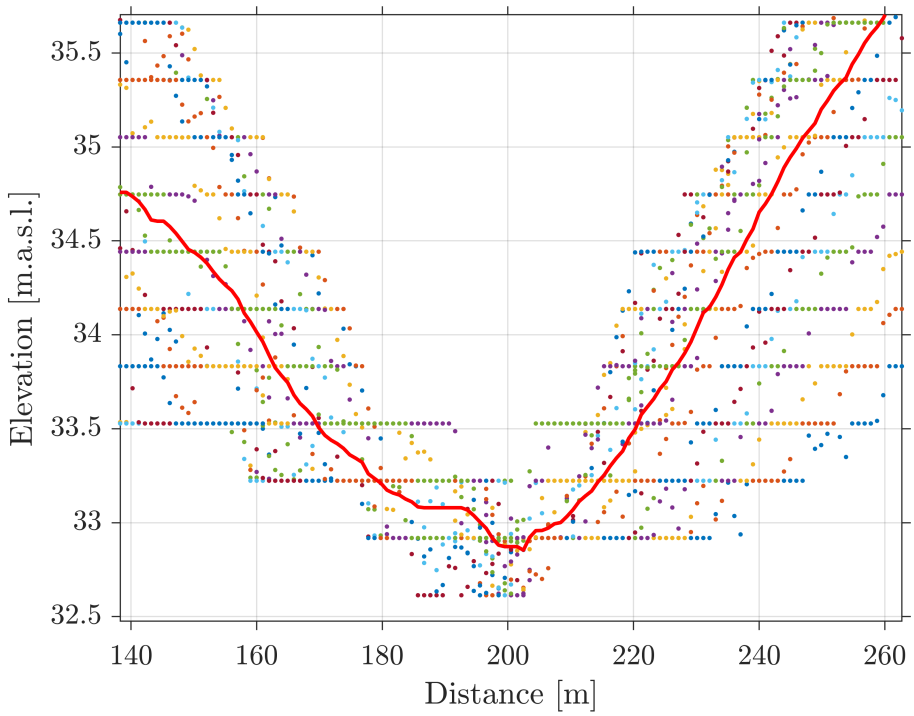

Figure A.19: Average Cross-Section Site #19

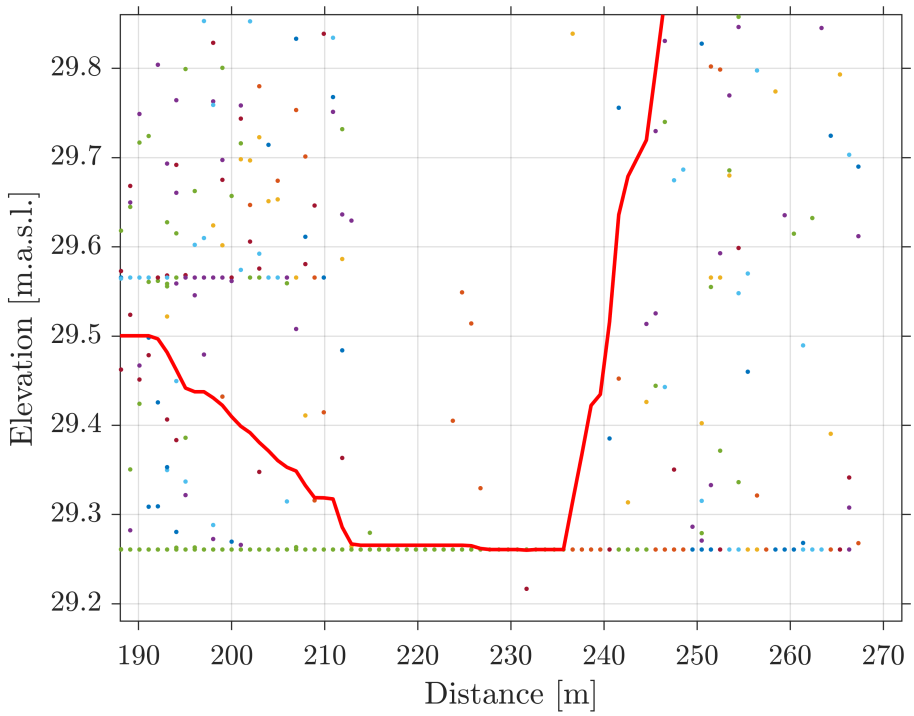

Figure A.20: Average Cross-Section Site #20

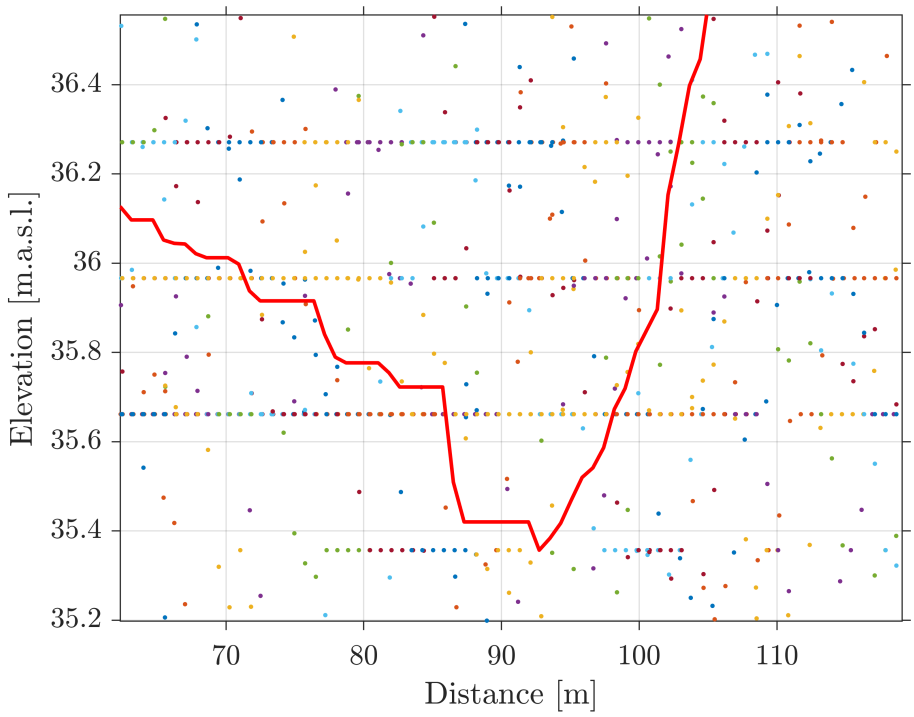

Figure A.21: Average Cross-Section Site #21

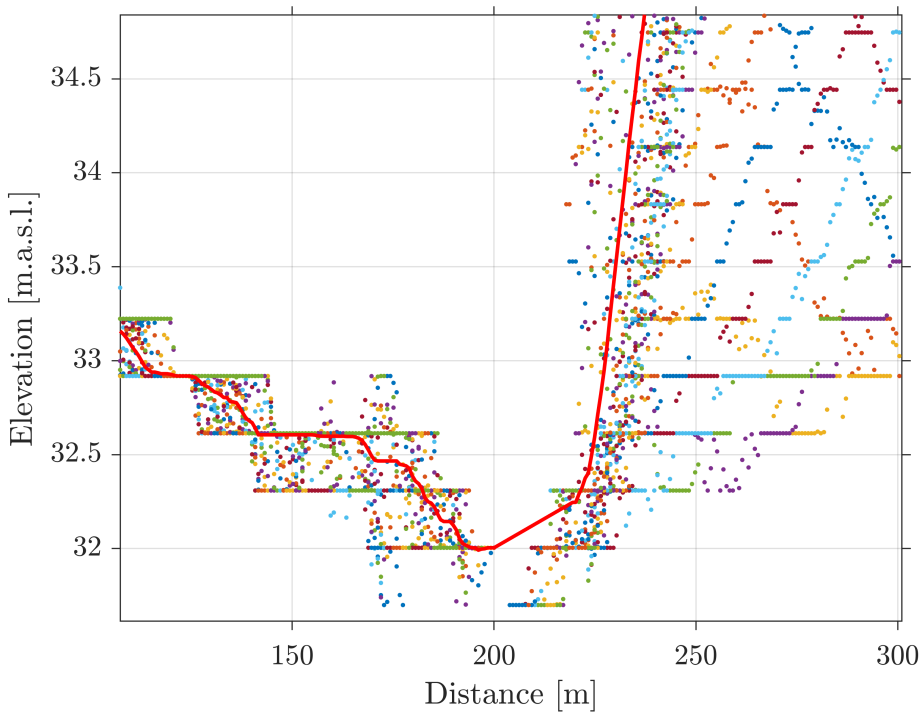

Figure A.22: Average Cross-Section Site #22

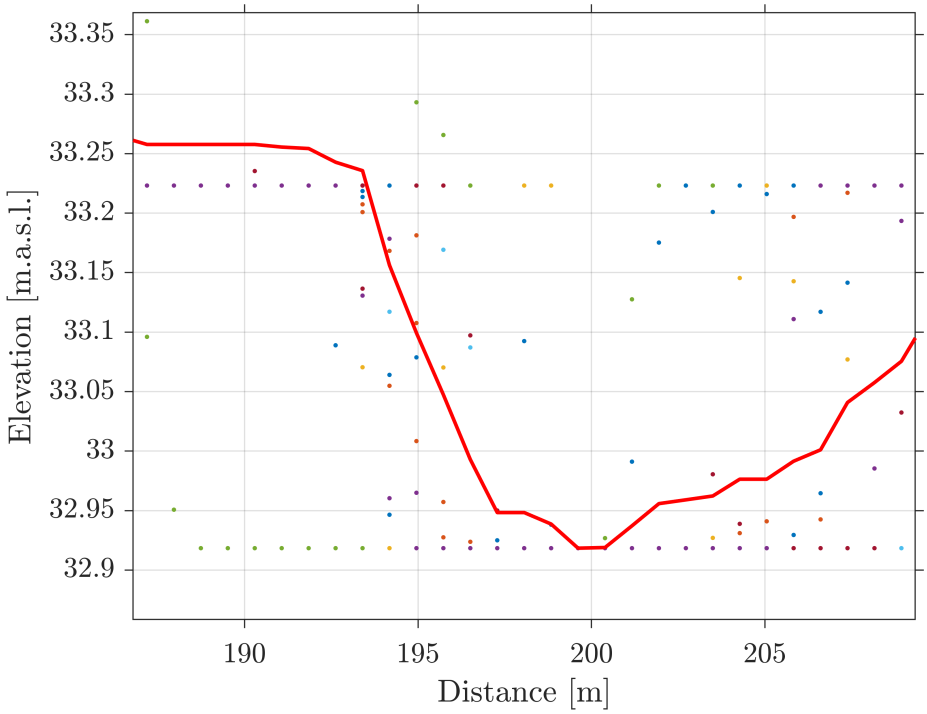

Figure A.23: Average Cross-Section Site #23

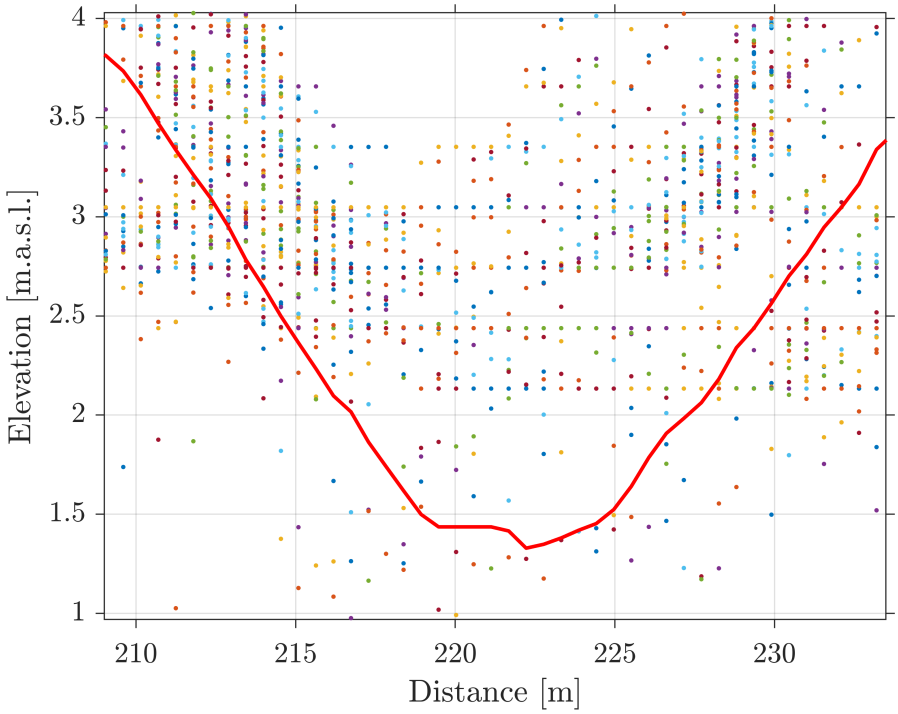

Figure A.24: Average Cross-Section Site #24

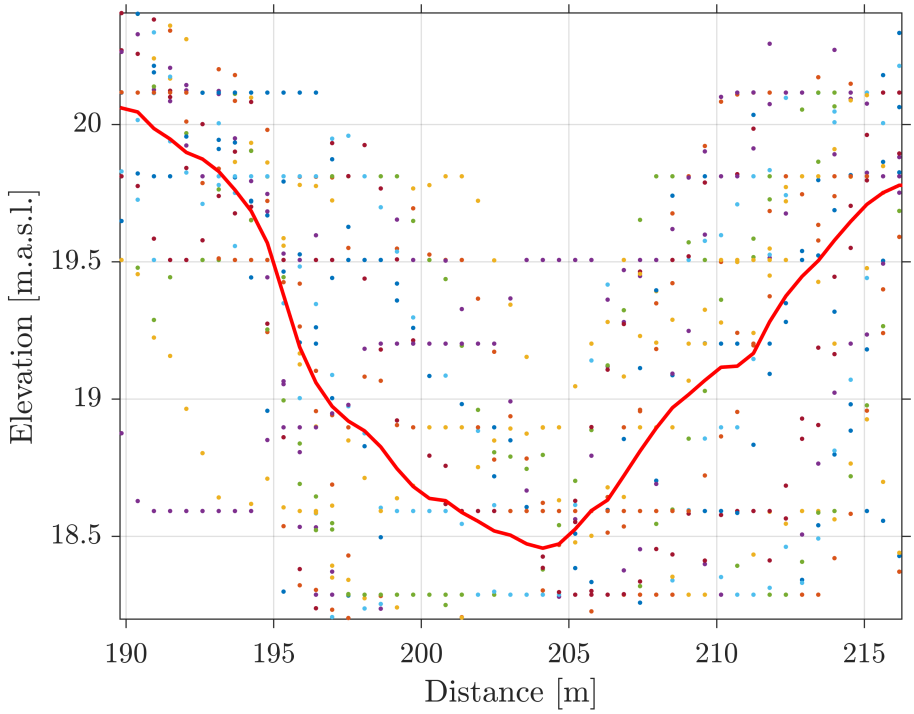

Figure A.25: Average Cross-Section Site #25

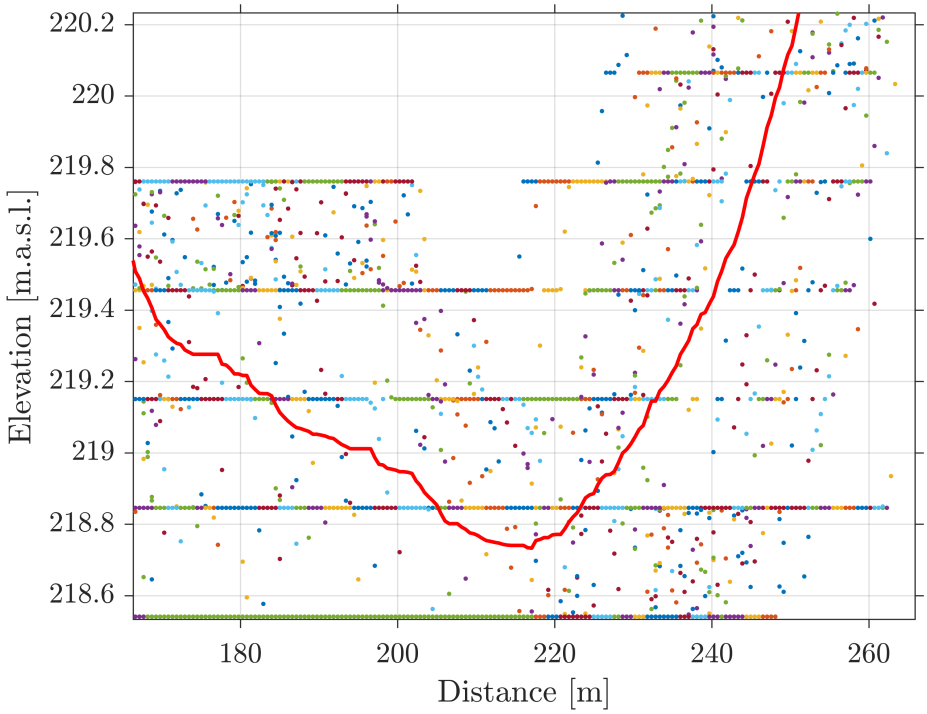

Figure A.26: Average Cross-Section Site #26

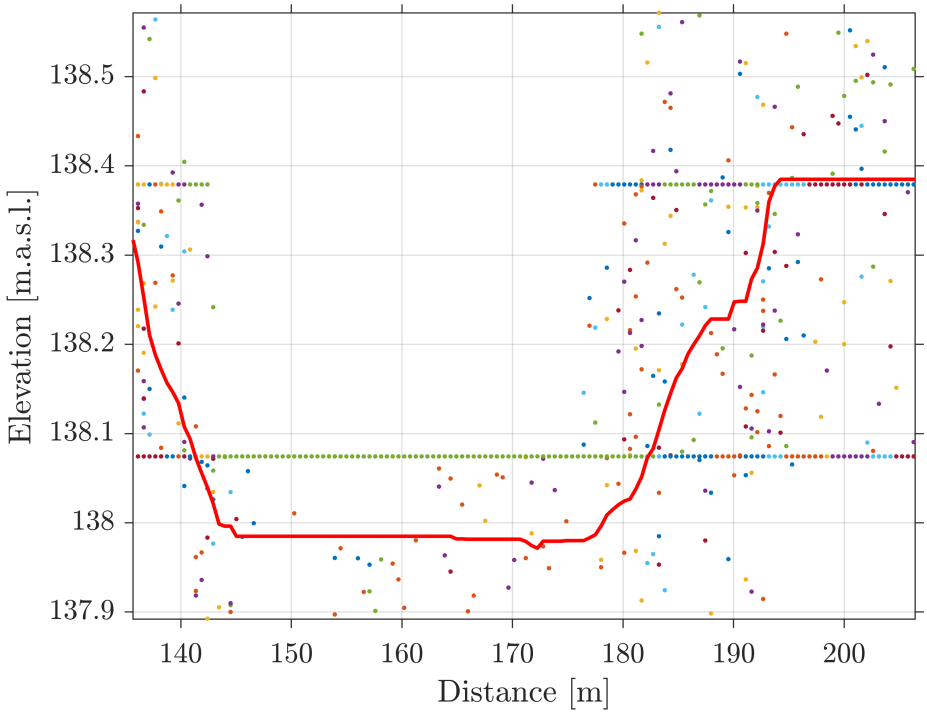

Figure A.27: Average Cross-Section Site #27

Appendix B

Theory

This chapter contains the basic theory behind the method developed in this research and the abrupt change and frequency figures for each gauge.

B.1 Hydraulic Geometry Theory

Singh (2003) explains the "hydraulic geometry" as the relationships between the mean stream channel form and discharge both at-a-station and downstream along a stream network in a hydrologically homogeneous basin. The channel form includes the mean cross-section geometry (width, depth, cross-section, meander length), and the hydraulic variables which include the mean slope, mean friction, and mean velocity for a given influx of water and sediment to the channel and the specified channel boundary conditions. Leopold and Maddock (1953) expressed the hydraulic geometry relationships for a channel in the form of power functions of discharge as

$$B = aQ^b \quad (1)$$

$$D = cQ^f \quad (2)$$

$$V = kQ^m \quad (3)$$

here B is the channel width; d is the flow hydraulic depth; V is the flow velocity;

Q is the flow discharge; and a, b, c, f, k, and m are parameters. To equations (A.1, A.2, and A.3), also added are

$$A = pQ^q \tag{4}$$

$$S = sQ^y \tag{5}$$

$$n = NQ^j \tag{6}$$

where n is Manning's roughness factor; S is slope; A is area; and N, p, q, s, j, and y are parameters. Exponents b, f, m, q, j, and y represent, respectively, the rate of change of the hydraulic variables B, d, V, A, S, and n as Q changes; and coefficients a, c, k, p, N, and s are scale factors that define the values of B, d, V, A, n, and S when Q = 1. The hydraulic variables, width, depth and velocity, satisfy for rectangular channels the continuity equation:

$$Q = BdV \tag{7}$$

Therefore, the coefficients and exponents in equations (A.1, A.2, and A.3) satisfy:

$$ack = 1 \tag{8}$$

$$b + f + m = c1 \tag{9}$$

The at-a-site hydraulic geometry entails mean values over a certain period,

such as a week, a month, a season, or a year. The concept of downstream hydraulic geometry involves spatial variation in channel form and process at a constant frequency of flow. Richard (1982) has noted that the downstream hydraulic geometry involving the channel process and form embodies two types of analyses both of which are expressed as power functions of the form (Rhoads, 1991) given by equations (1a, b). The first type of analysis is typified by the works of Leopold and Maddock (1953) and Wolman (1955) who formalized a set of relations, such as equations (A.1, A.2, A.3, A.4, and A.5), to relate the downstream changes in flow properties (width, mean depth, mean velocity, area, slope and friction) to mean discharge. This type of analysis describes the regulation of flow adjustments by channel form in response to increases in discharge downstream, and has been applied at particular cross-sections as well as in the downstream direction.

B.2 Bankfull Shields Number Theory

The Shield's number is a nondimensional number used to calculate the initiation of motion of sediment in a fluid flow, which can be related to the evolution of river cross-section toward a quasi-equilibrium stage (bankfull). The theory behind the bankfull Shield's number is outlined in Parker (1978 a,b).

B.3 Extreme Value Type-I Distribution

In probability theory and statistics, the Generalized Extreme Value distribution Type-I (Gumbel distribution) is used to model the distribution of the maximum

(or the minimum) of a number of samples of various distributions. This distribution is widely used in hydrology for its logarithmic scale properties. The cumulative distribution function of the Gumbel distribution is:

$$F(x;\alpha,\beta) = e^{-e^{(\alpha-x)\beta}} \tag{10}$$

Where the location (μ) and scale (β) parameters are:

$$\alpha = \bar{x} - \gamma\beta \tag{11}$$

$$\beta = s\frac{\sqrt{6}}{\pi} \tag{12}$$

γ is the Eulerg-Mascheroni constant nad θ is the standard deviation of the data. Therefore, to extrapolate the data the distributions parameters must be computed and the solve the distribution (where T is return period in years):

$$K(T) = -log(-log(1-1/T)) \tag{13}$$

$$Q(T) = \alpha + \beta K(T) \tag{14}$$

When the Median is known, then the parameters can be computed using the Median equation of the distribution.

$$Median = \alpha - \beta log(log(2)) \tag{15}$$

Appendix C

Graphical Results for All Sites

This chapter contains the plots used to estimate the bankfull breakpoint and the frequency curves (predictions) for each site.

C.1 Area-Coefficient Curves and Identified Bankfull Section Plots (abrupt change)

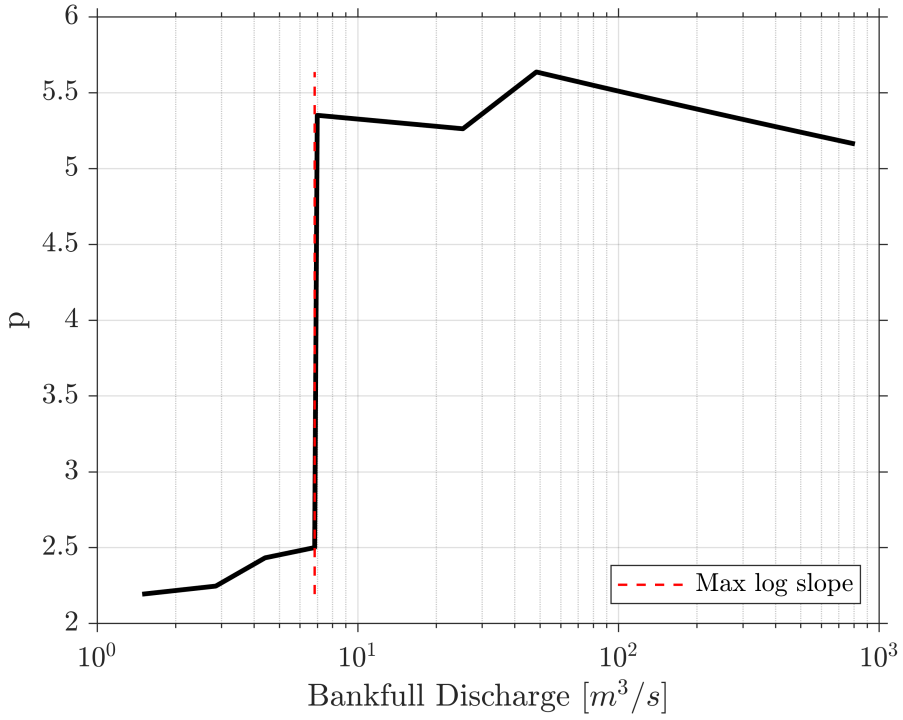

Figure 1: Area-Coefficient Curve Site #1

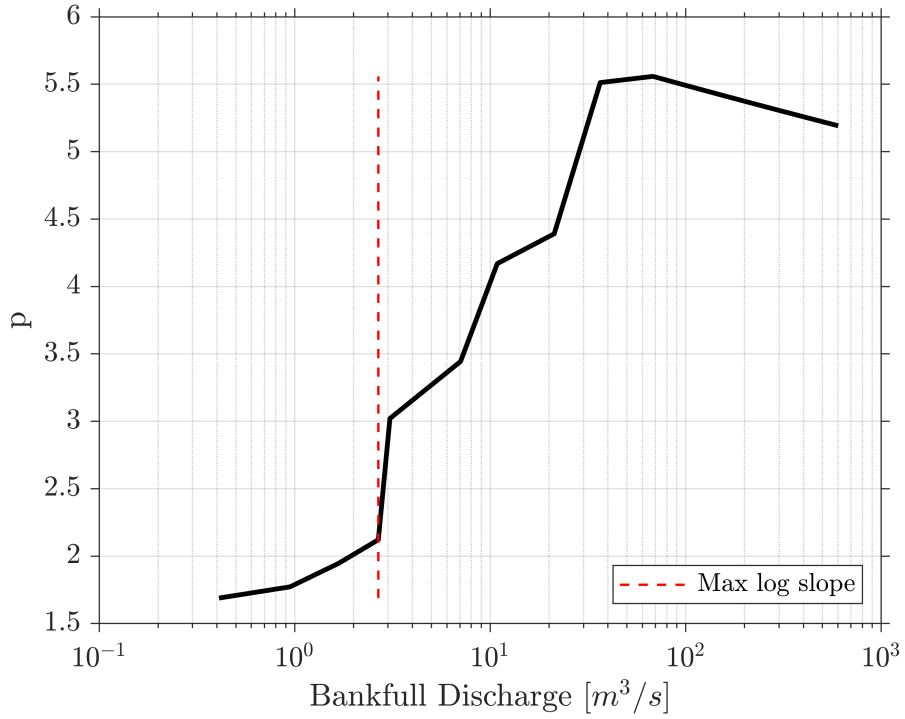

Figure 2: Area-Coefficient Curve Site #2

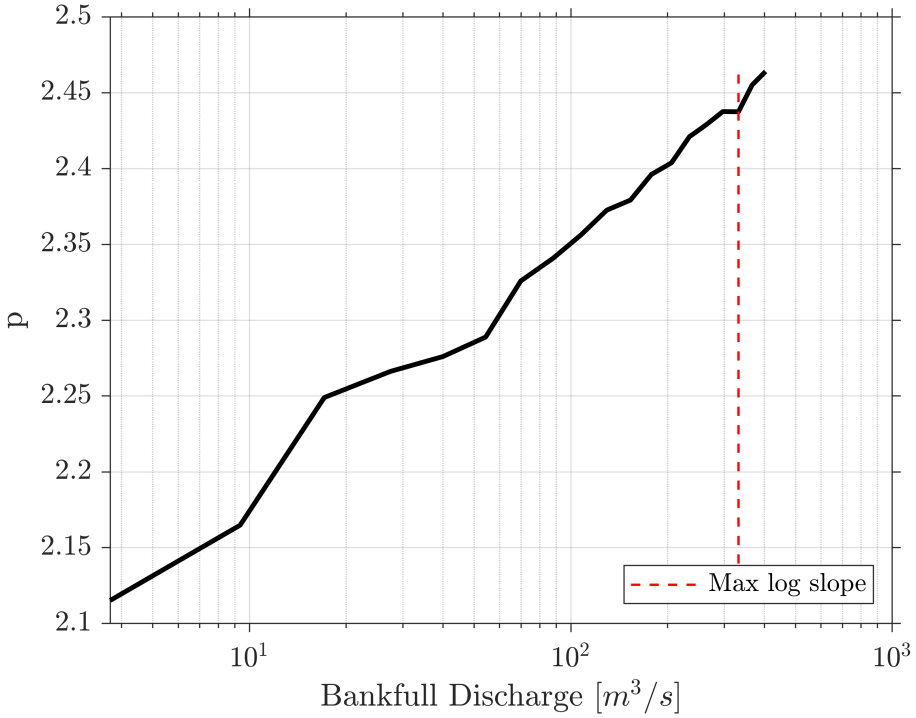

Figure 3: Area-Coefficient Curve Site #3

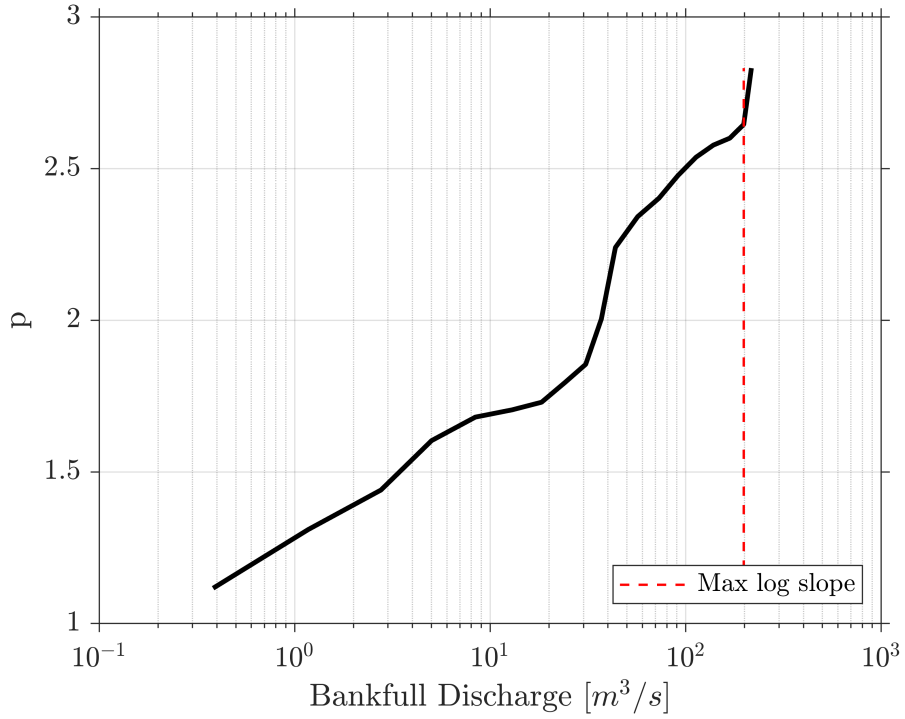

Figure 4: Area-Coefficient Curve Site #4

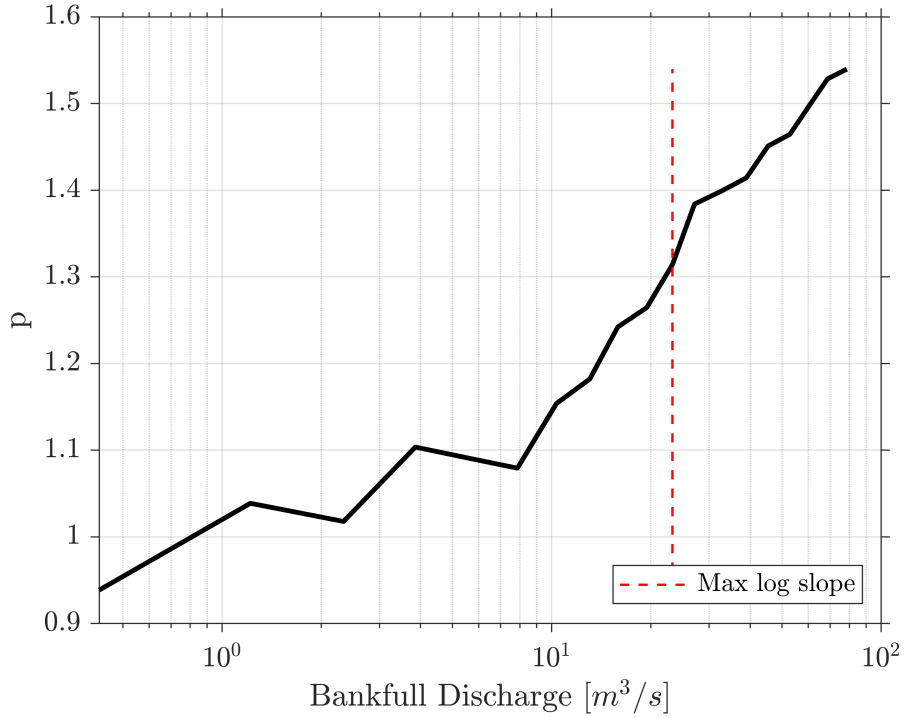

Figure 5: Area-Coefficient Curve Site #5

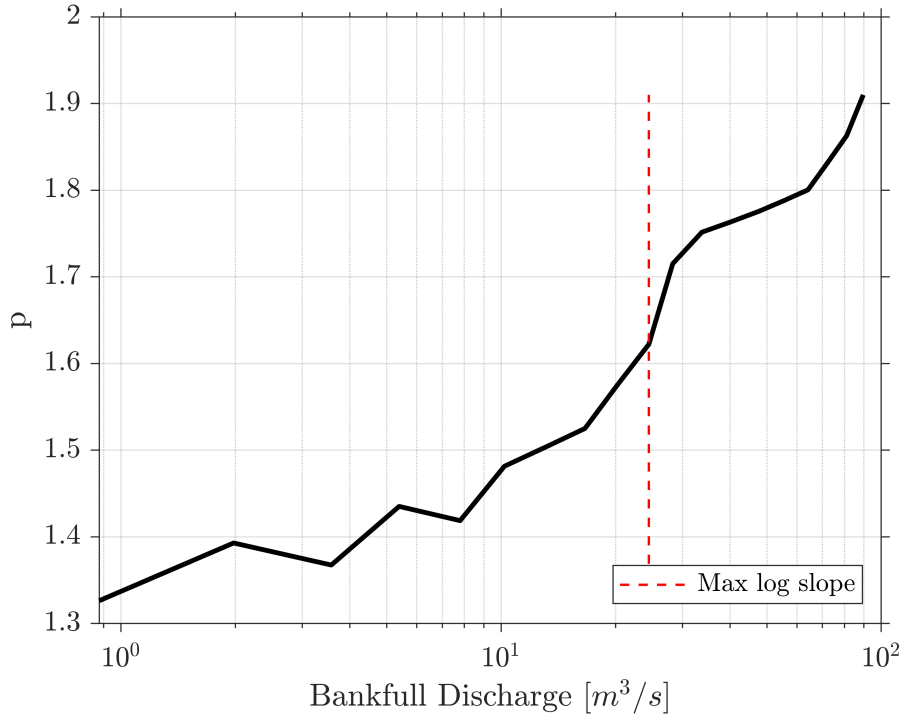

Figure 6: Area-Coefficient Curve Site #6

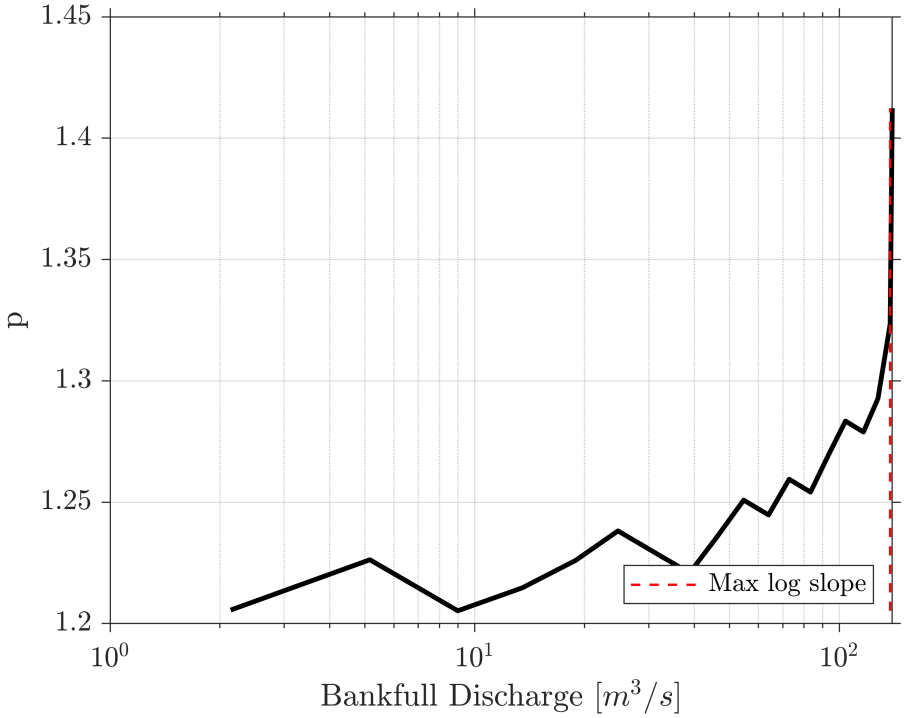

Figure 7: Area-Coefficient Curve Site #7

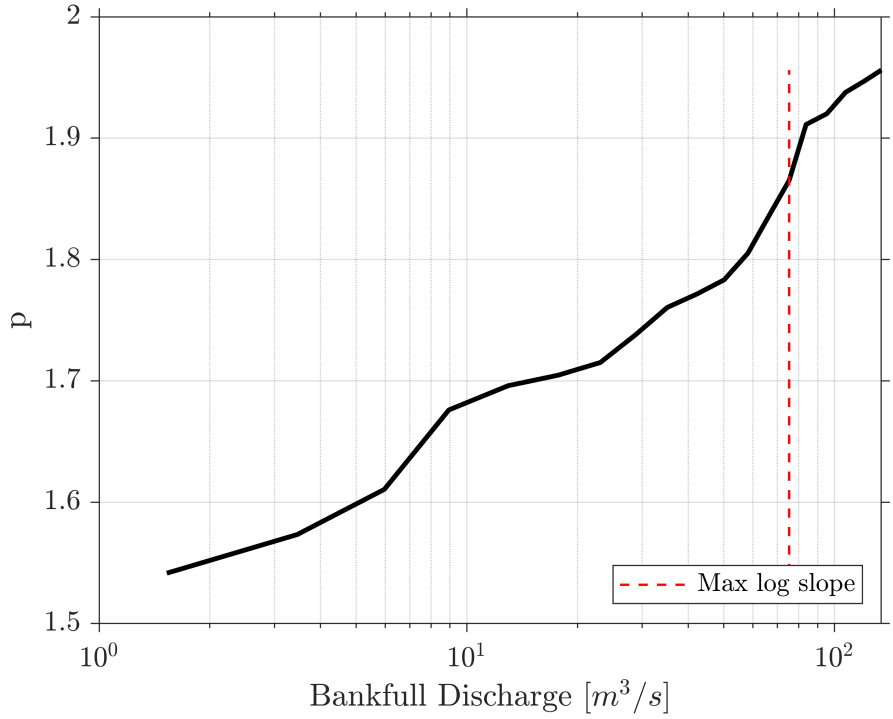

Figure 8: Area-Coefficient Curve Site #8

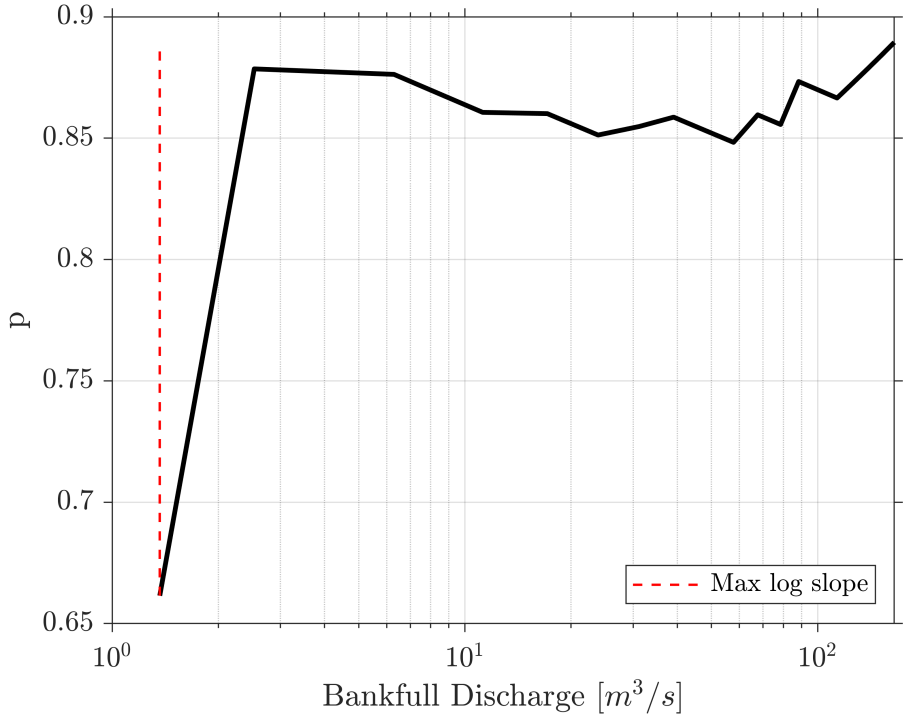

Figure 9: Area-Coefficient Curve Site #9

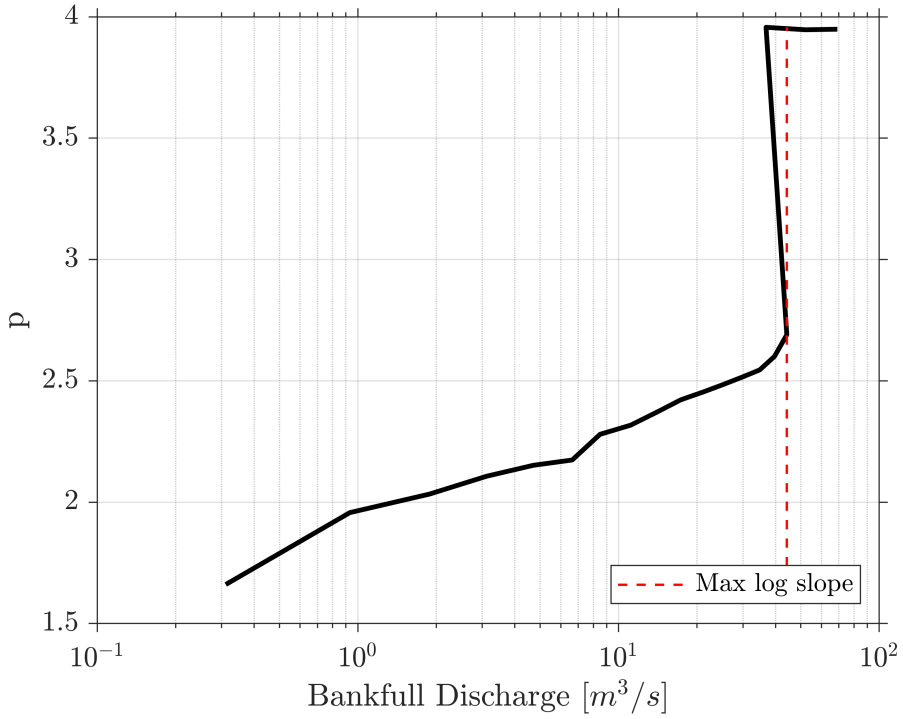

Figure 10: Area-Coefficient Curve Site #10

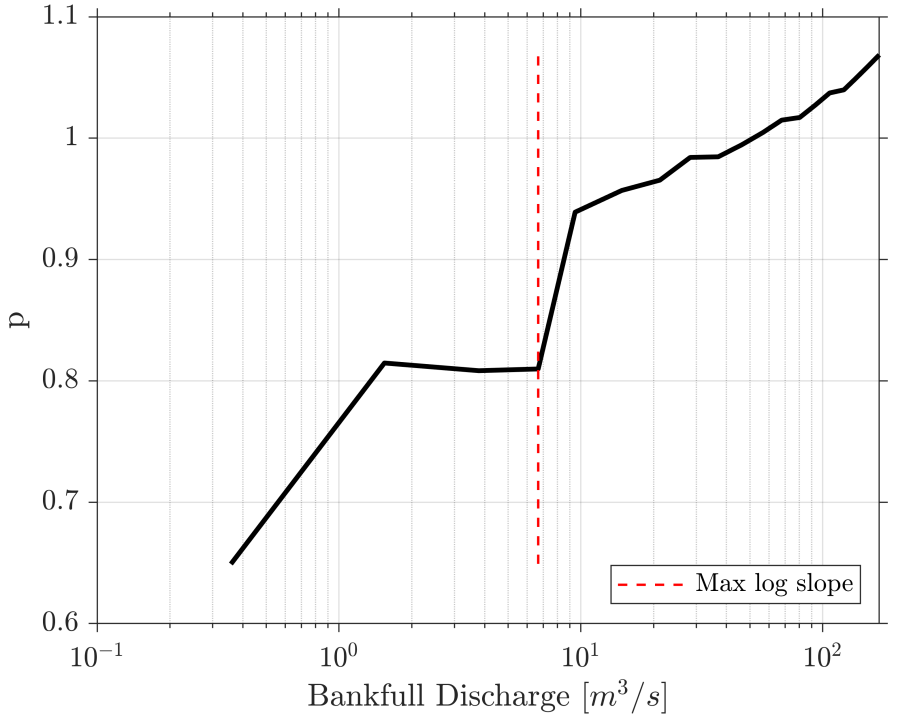

Figure 11: Area-Coefficient Curve Site #11

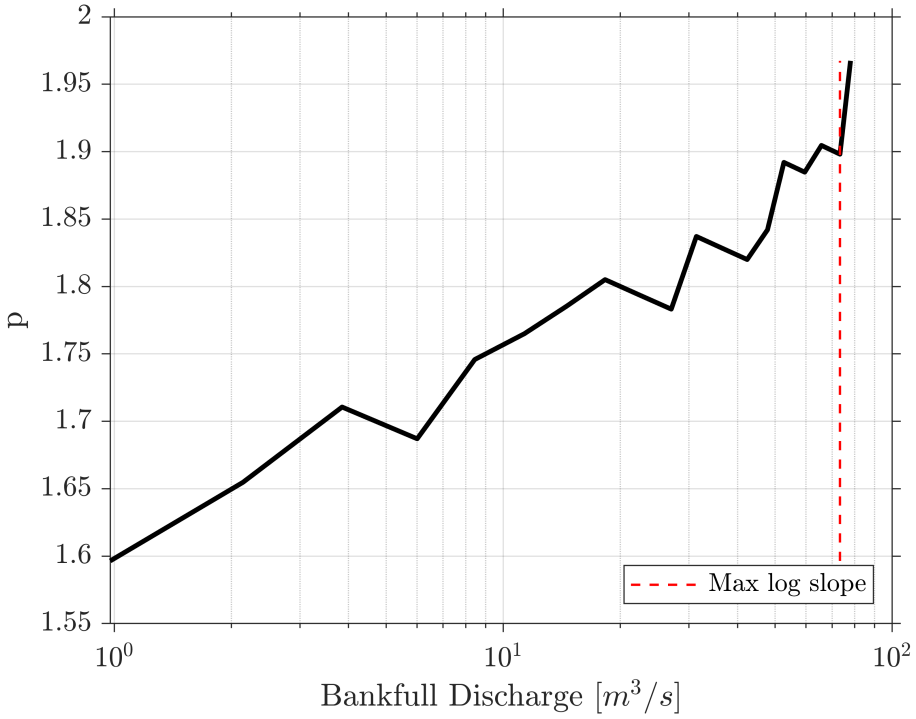

Figure 12: Area-Coefficient Curve Site #12

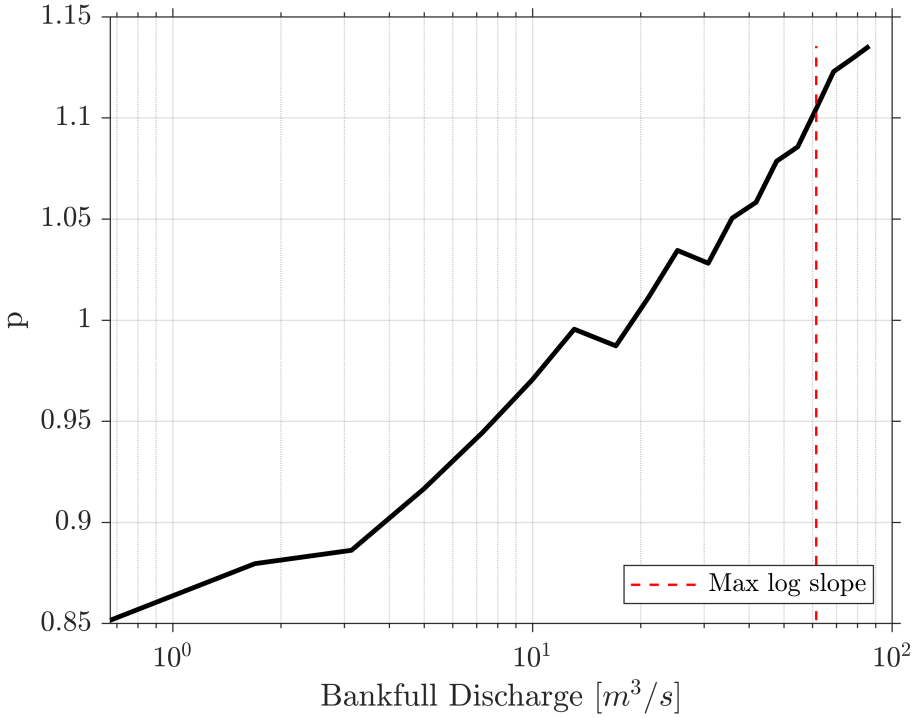

Figure 13: Area-Coefficient Curve Site #13

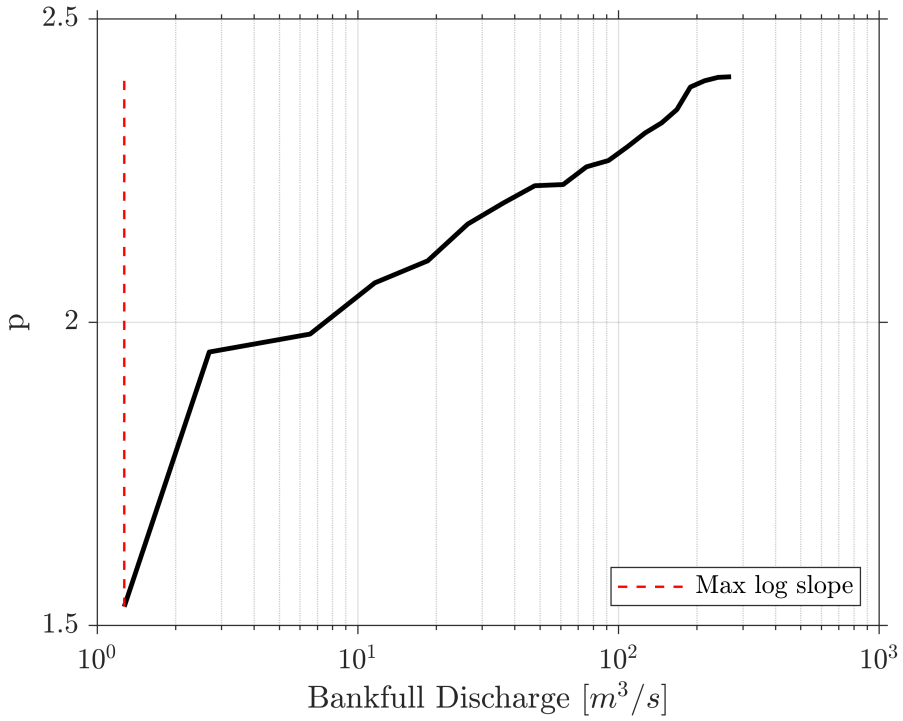

Figure 14: Area-Coefficient Curve Site #14

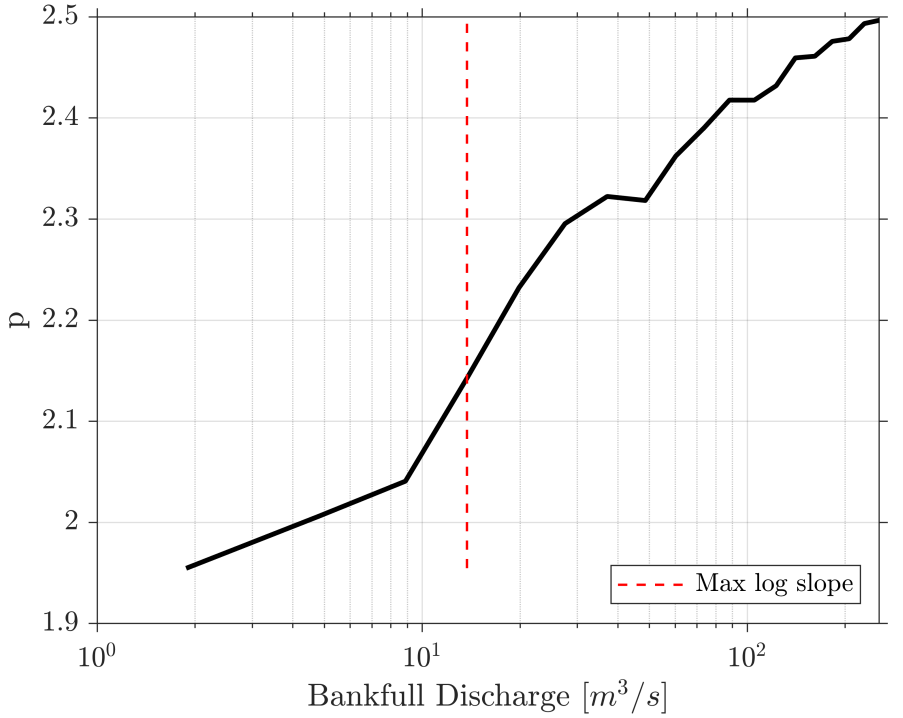

Figure 15: Area-Coefficient Curve Site #15

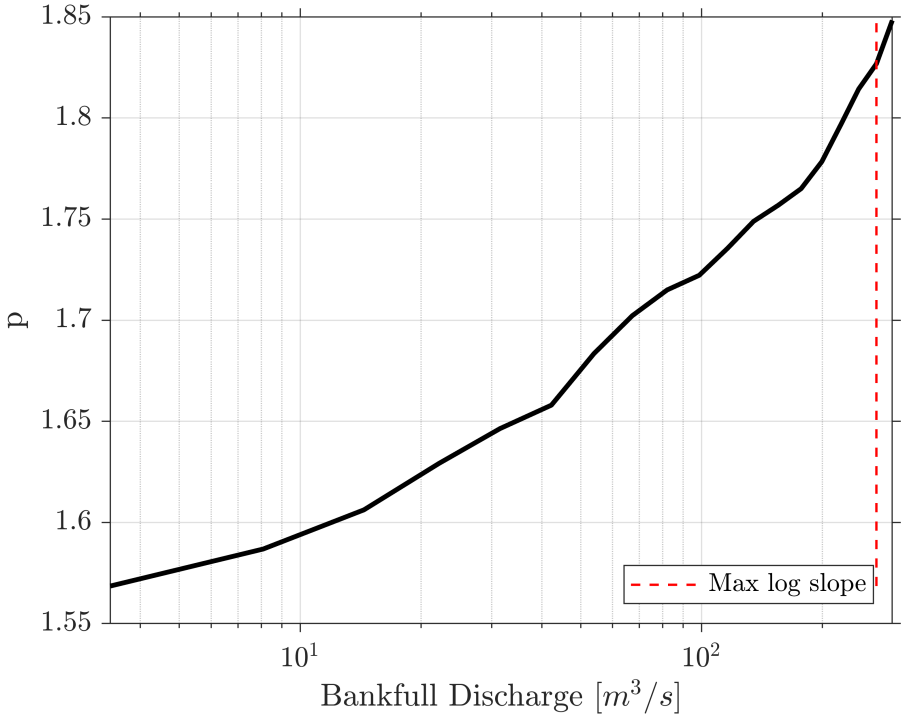

Figure 16: Area-Coefficient Curve Site #16

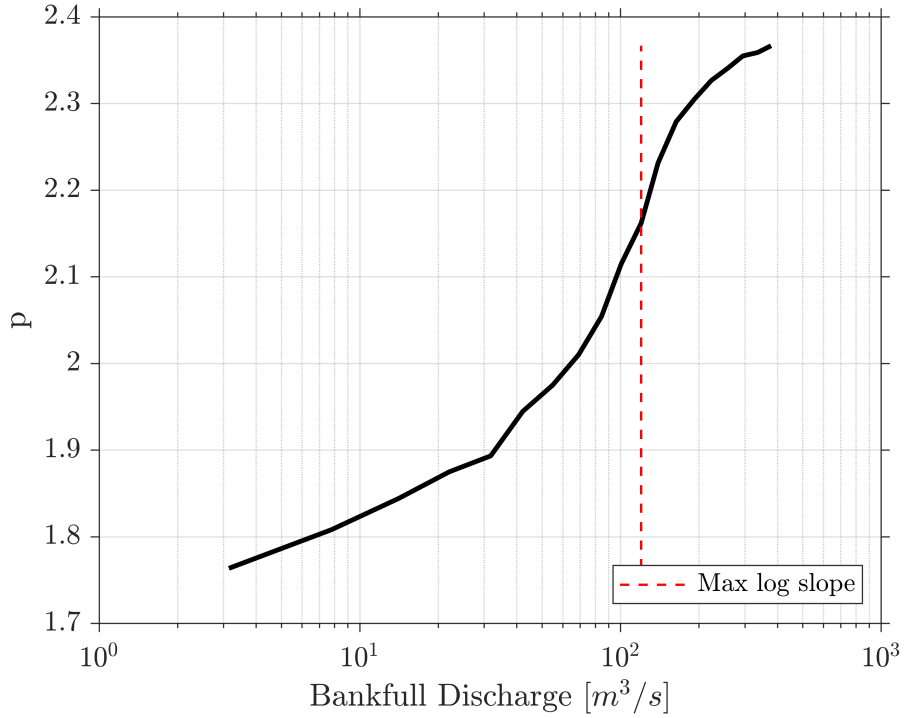

Figure 17: Area-Coefficient Curve Site #17

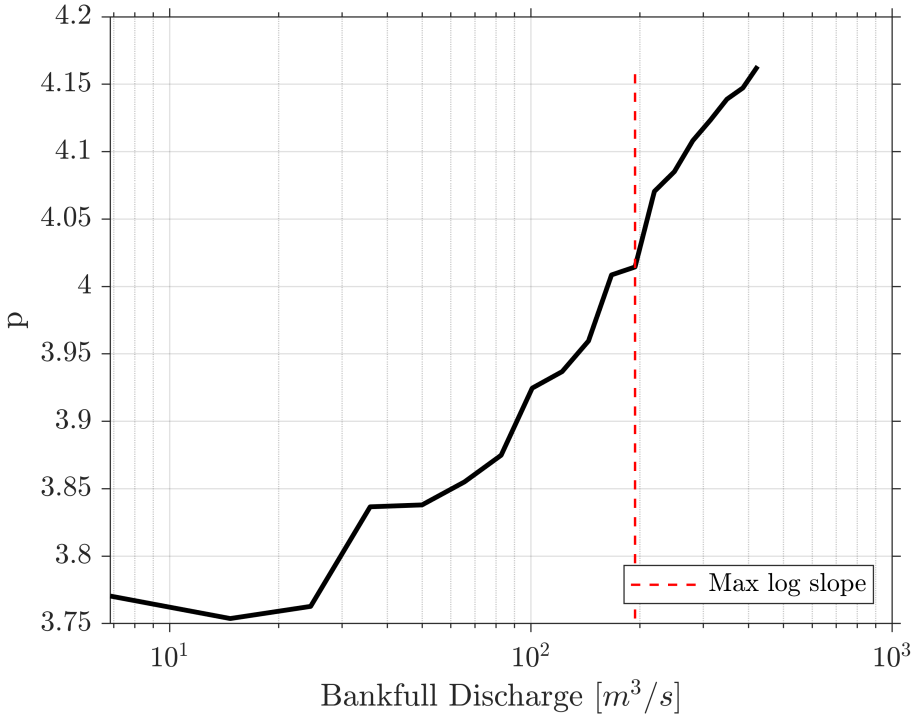

Figure 18: Area-Coefficient Curve Site #18

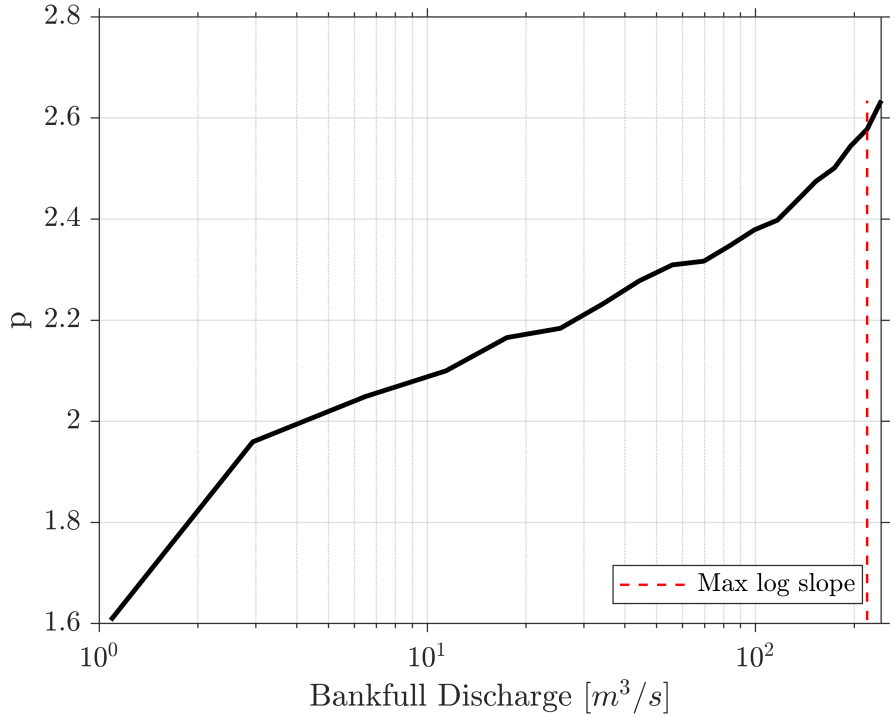

Figure 19: Area-Coefficient Curve Site #19

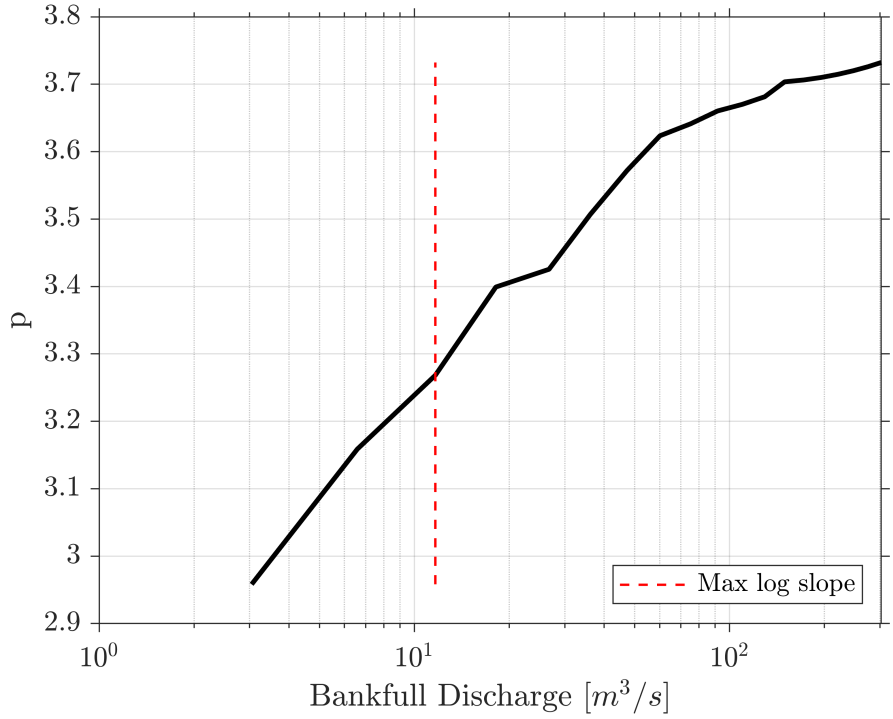

Figure 20: Area-Coefficient Curve Site #20

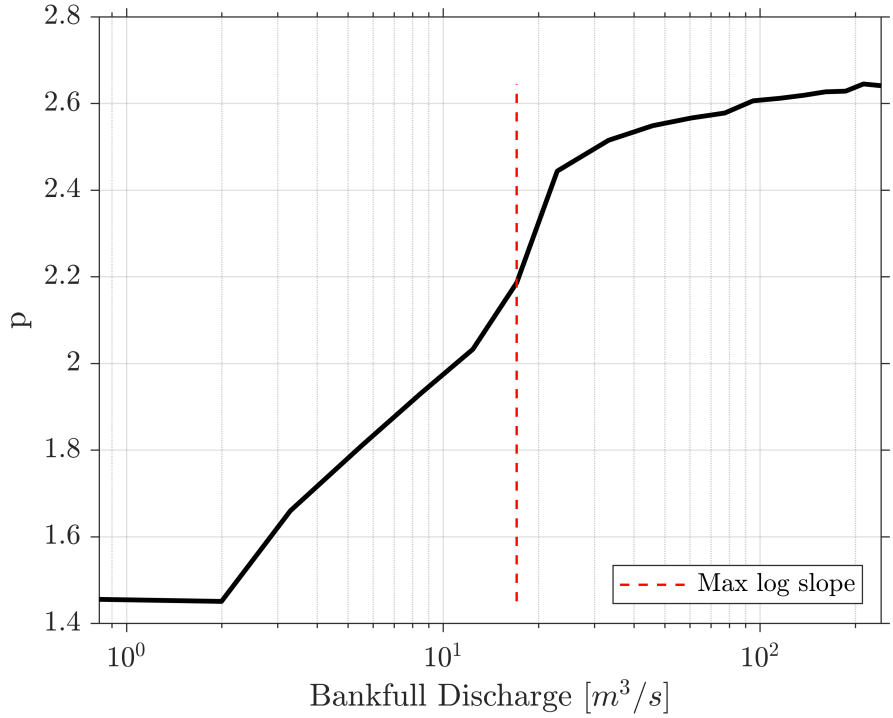

Figure 21: Area-Coefficient Curve Site #21

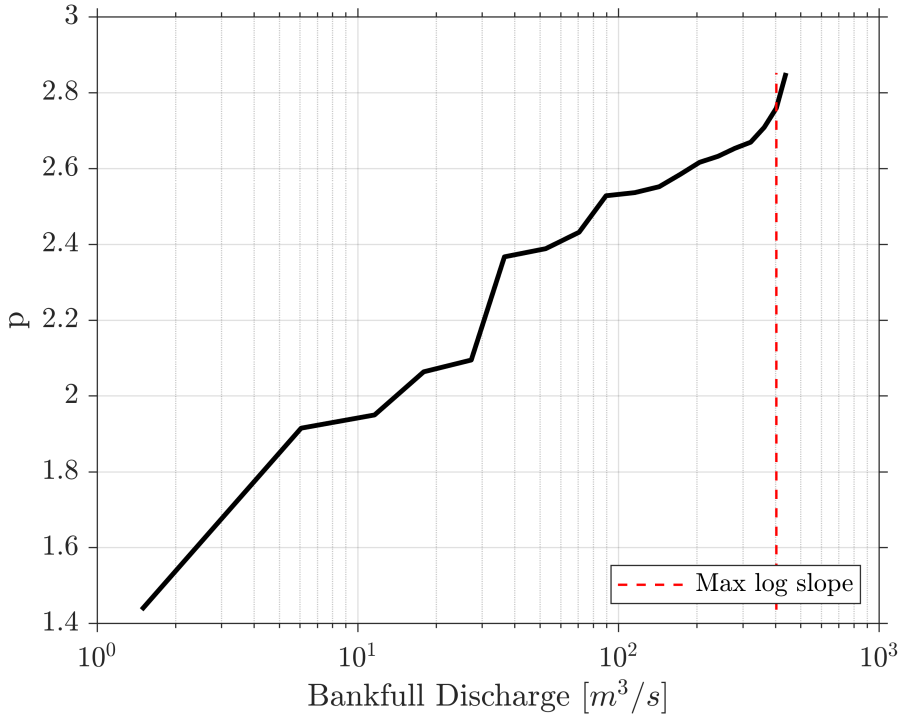

Figure 22: Area-Coefficient Curve Site #22

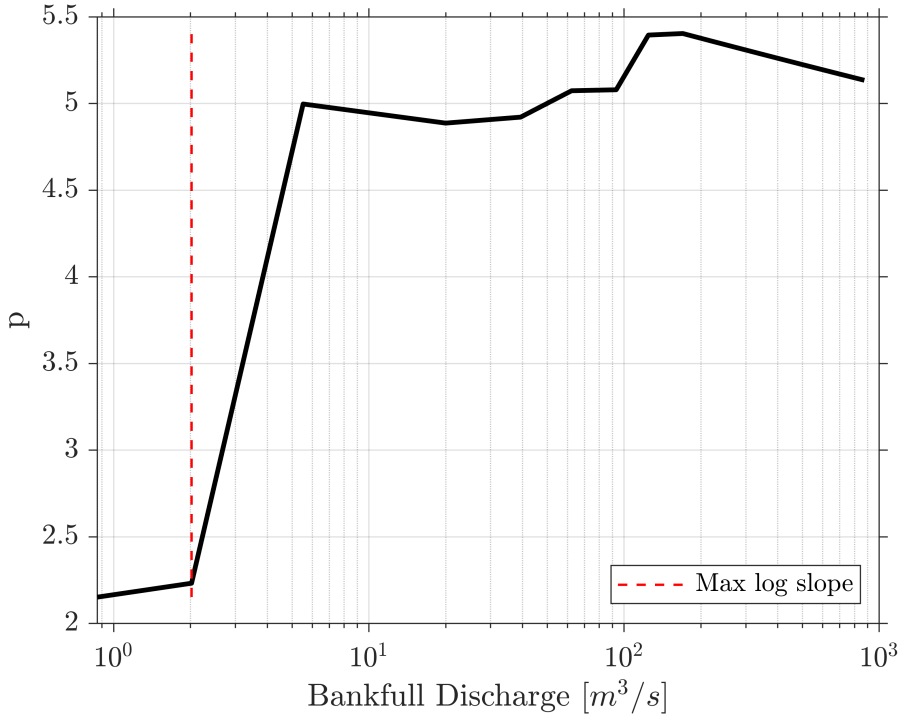

Figure 23: Area-Coefficient Curve Site #23

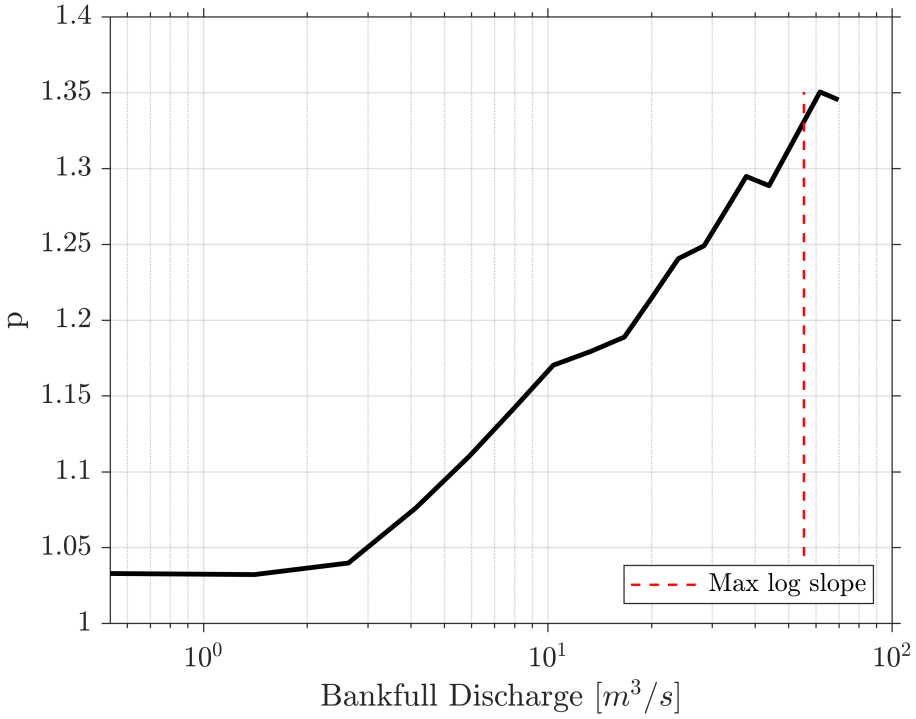

Figure 24: Area-Coefficient Curve Site #24

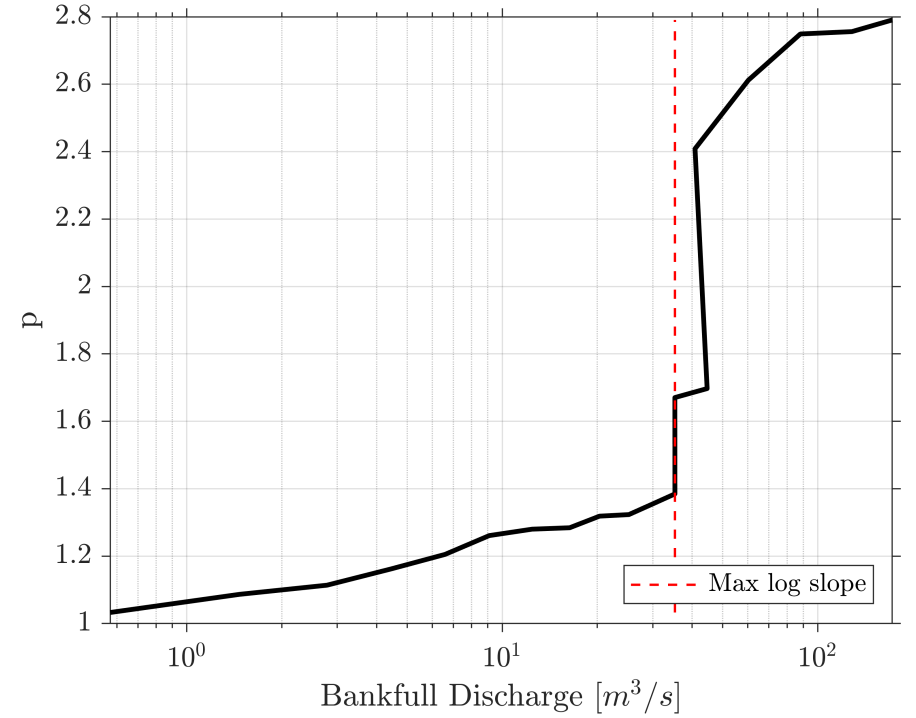

Figure 25: Area-Coefficient Curve Site #25

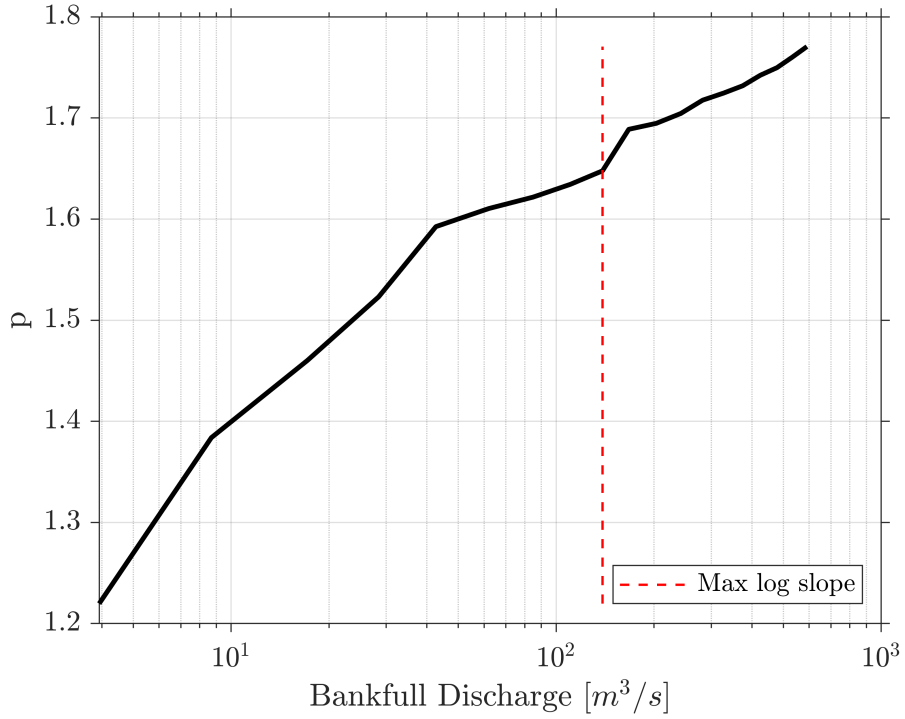

Figure 26: Area-Coefficient Curve Site #26

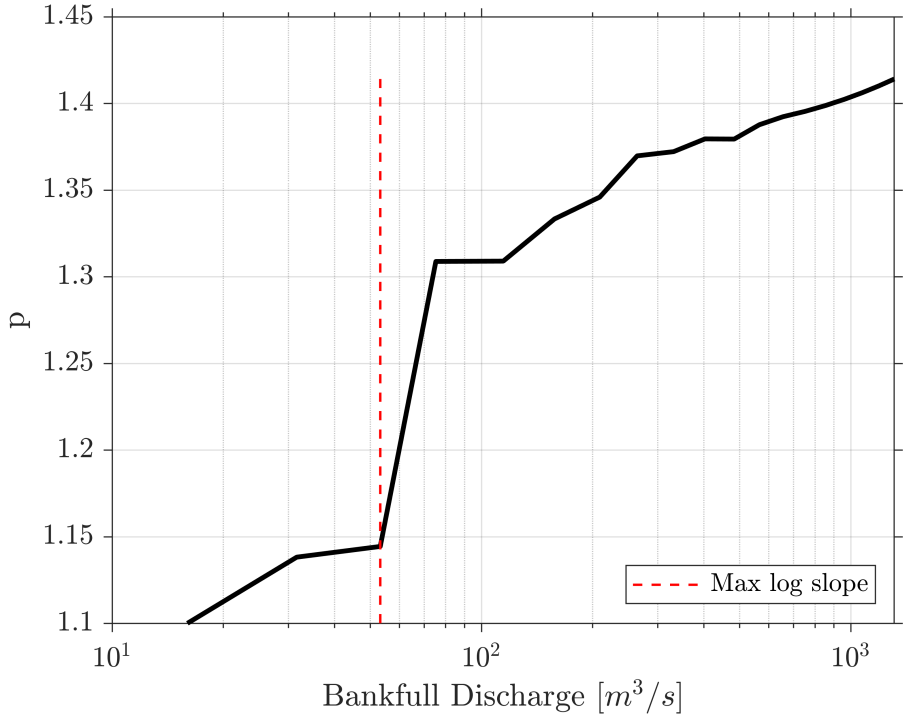

Figure 27: Area-Coefficient Curve Site #27

C.2 Frequency-Discharge Plots

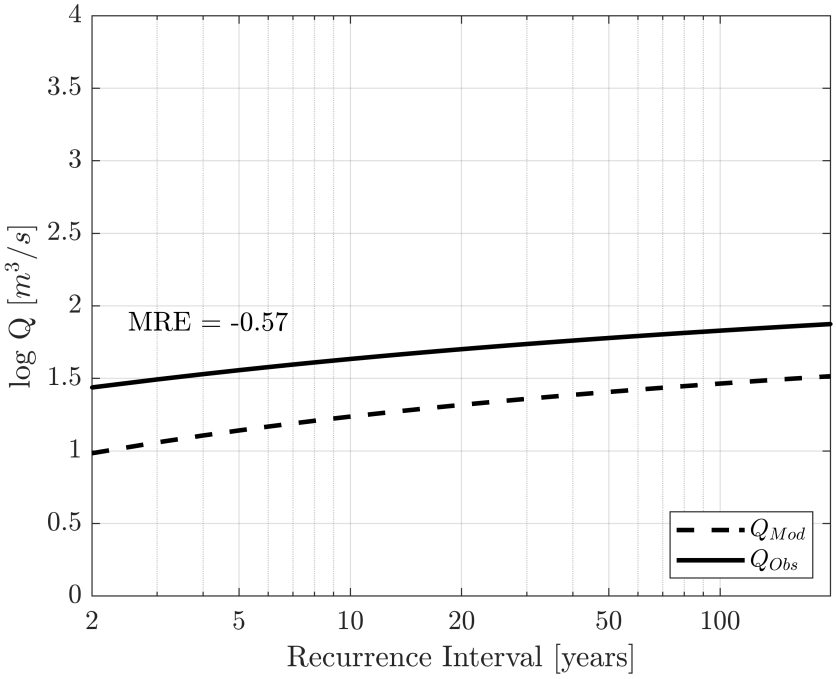

Figure 28: Frequency-Discharge Curves Site #1

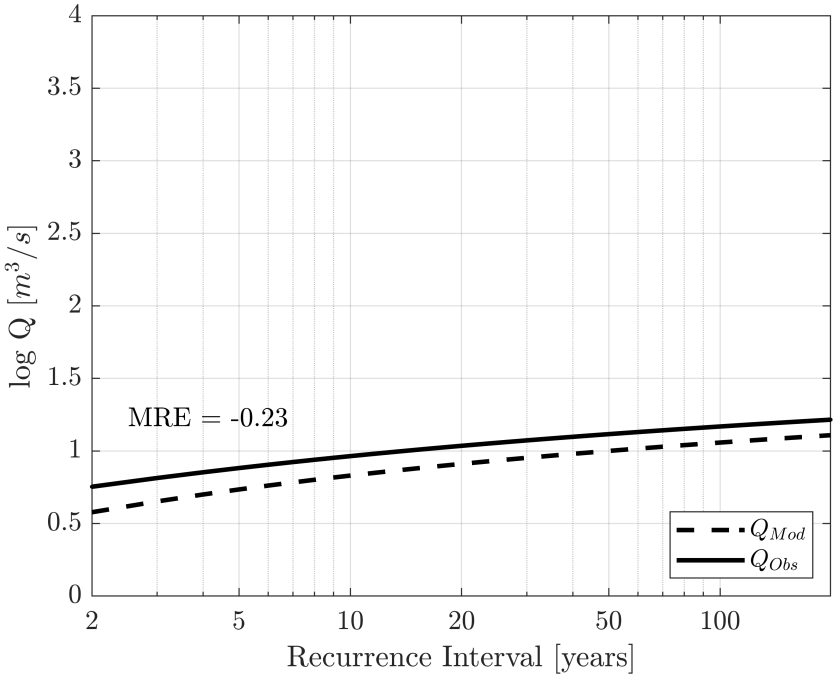

Figure 29: Frequency-Discharge Curves Site #2

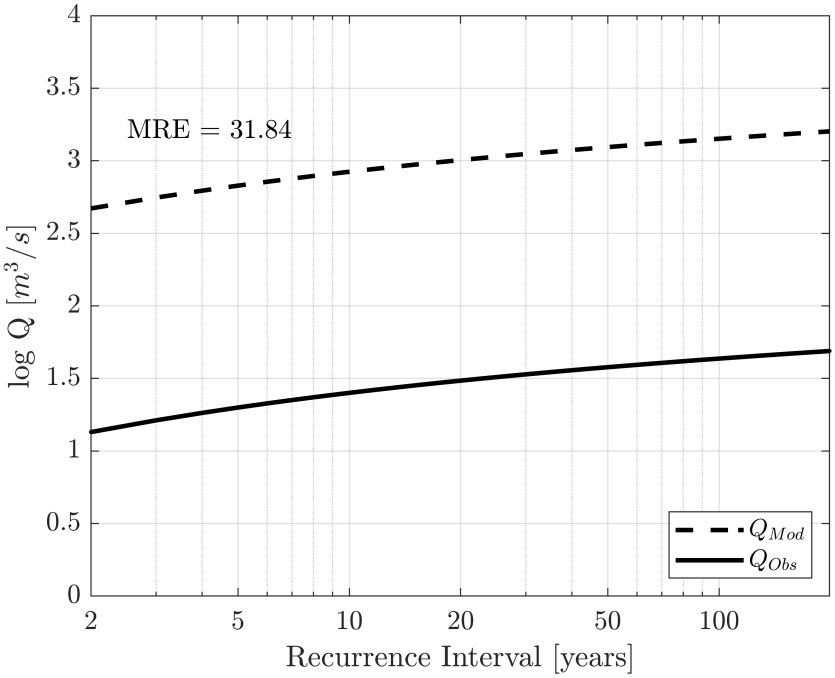

Figure 30: Frequency-Discharge Curves Site #3

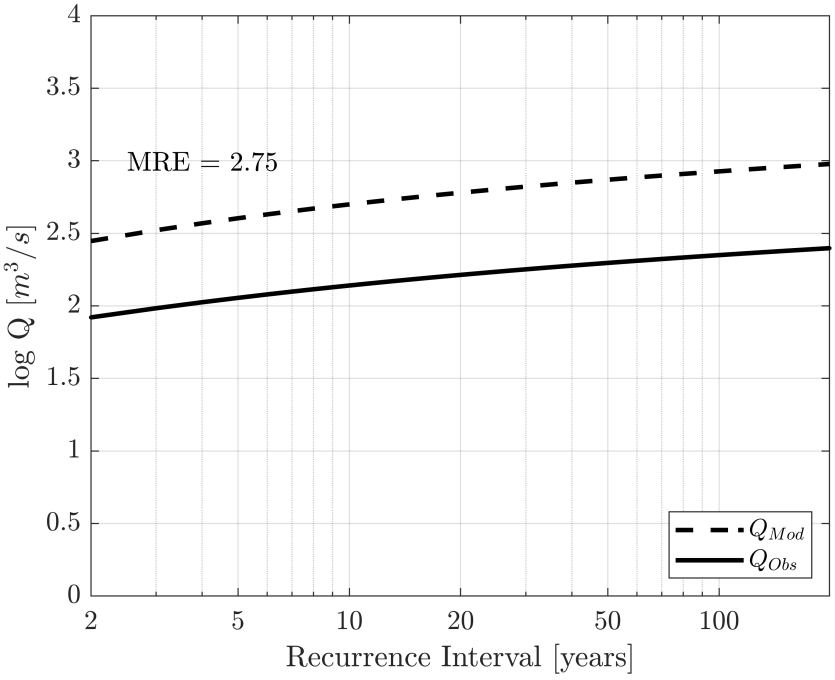

Figure 31: Frequency-Discharge Curves Site #4

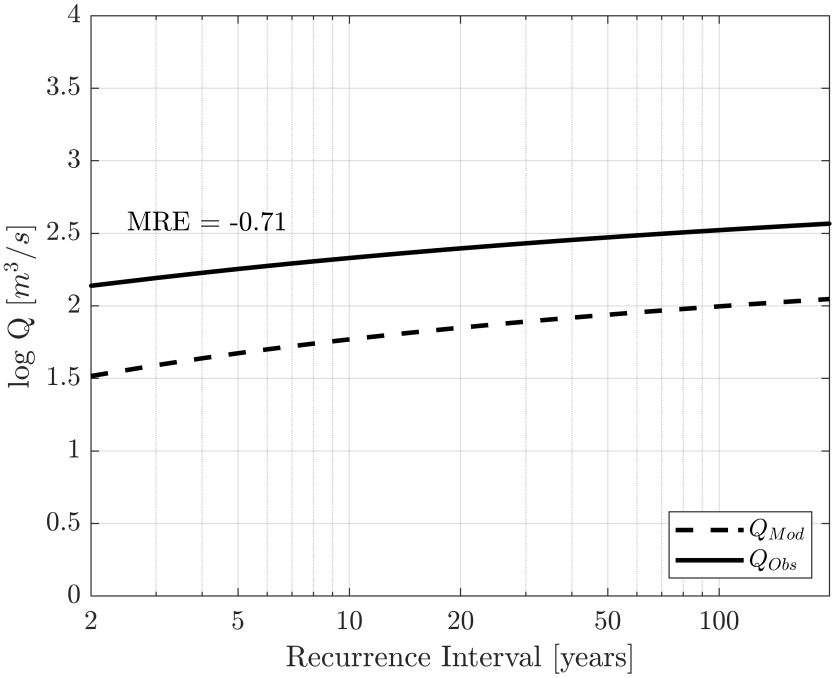

Figure 32: Frequency-Discharge Curves Site #5

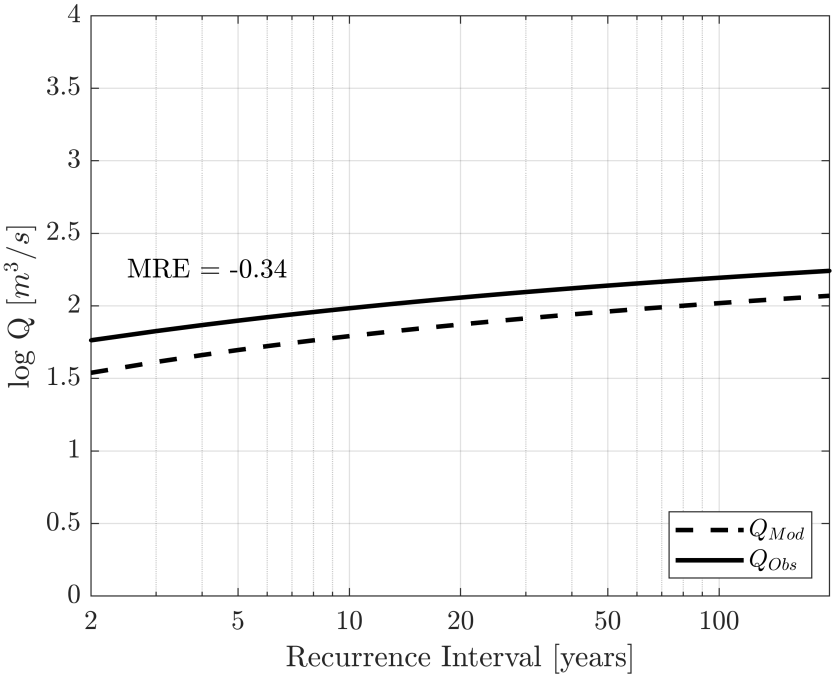

Figure 33: Frequency-Discharge Curves Site #6

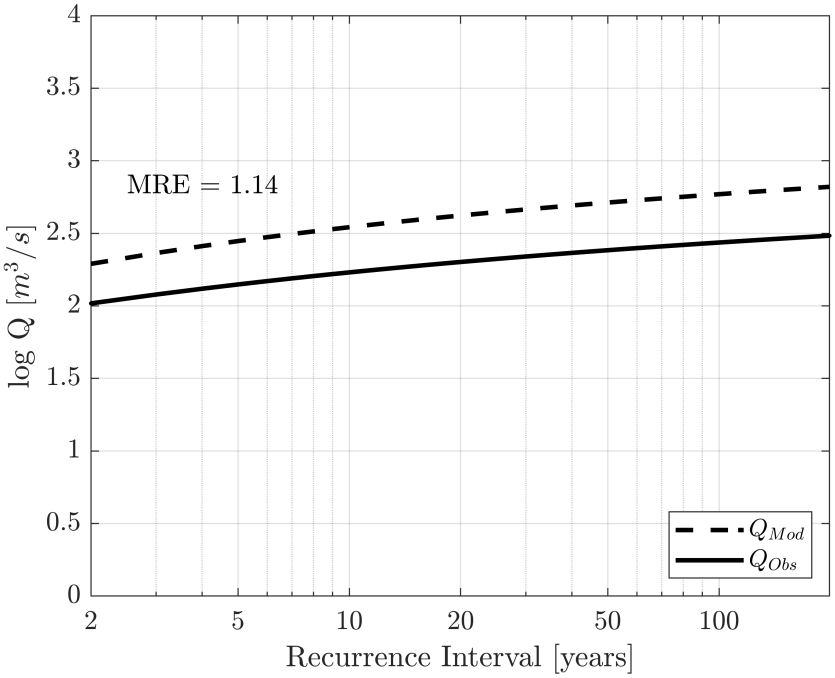

Figure 34: Frequency-Discharge Curves Site #7

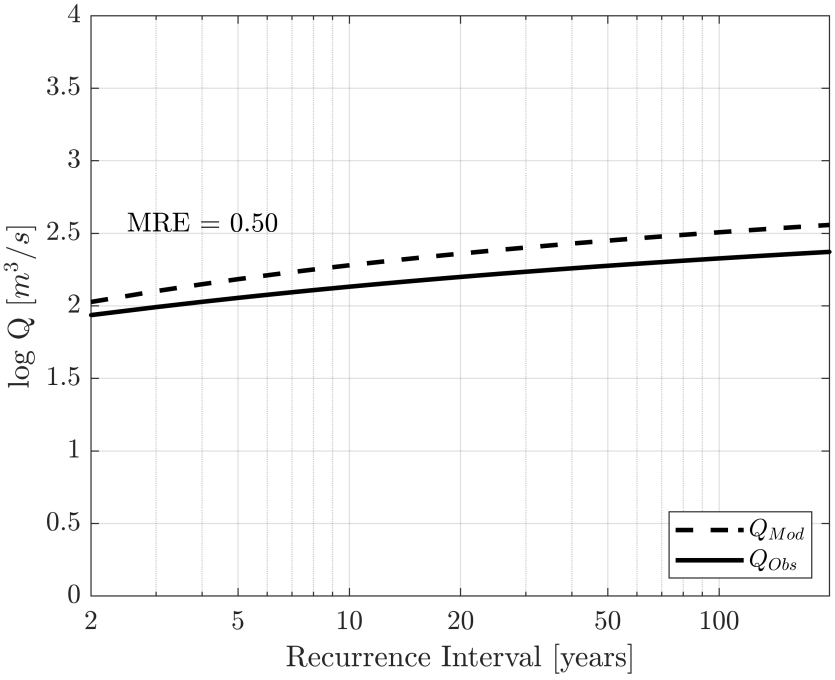

Figure 35: Frequency-Discharge Curves Site #8

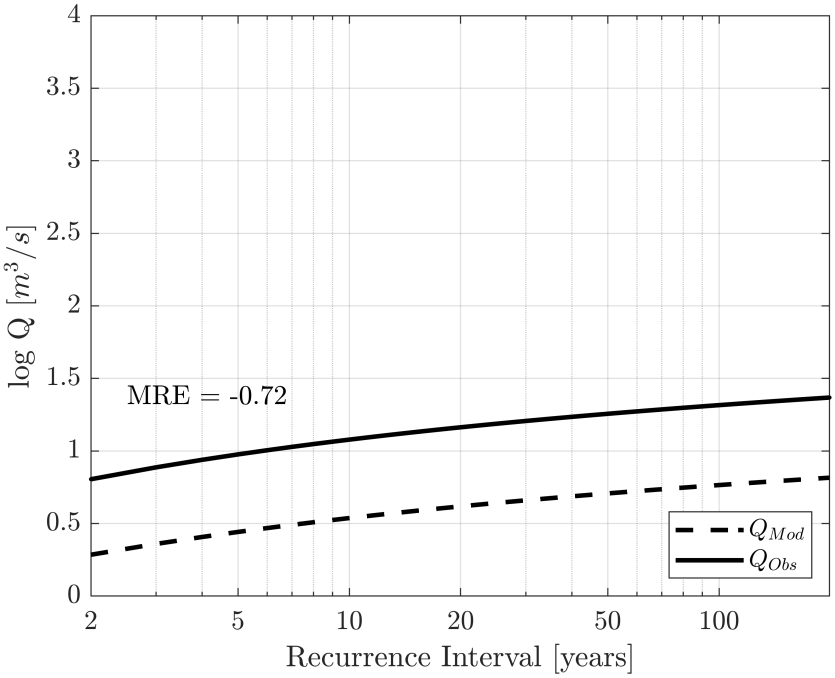

Figure 36: Frequency-Discharge Curves Site #9

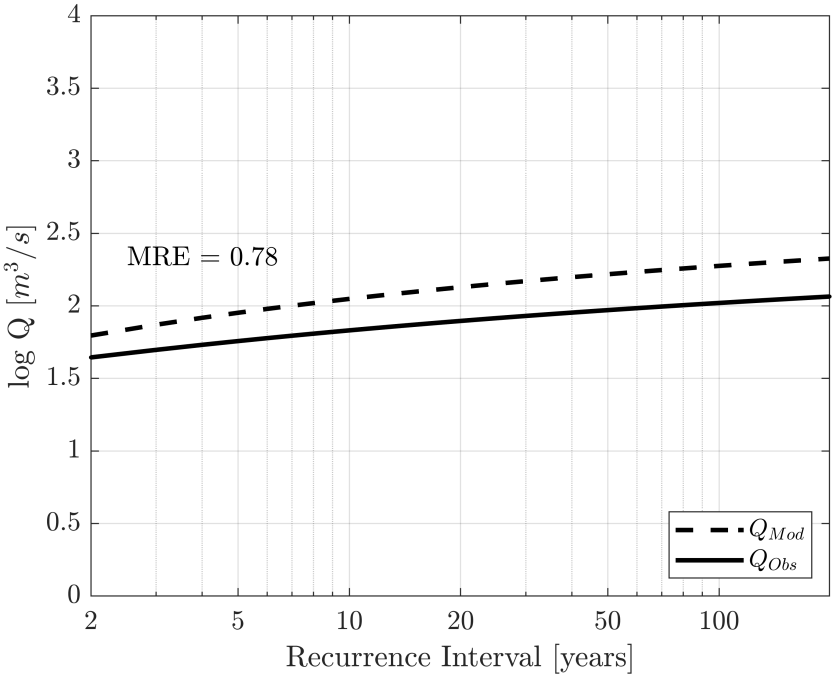

Figure 37: Frequency-Discharge Curves Site #10

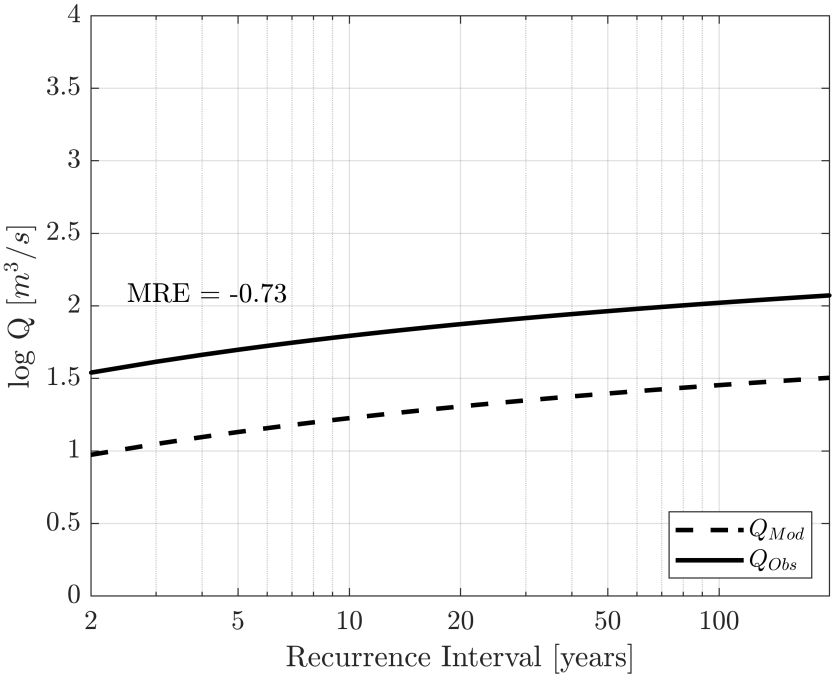

Figure 38: Frequency-Discharge Curves Site #11

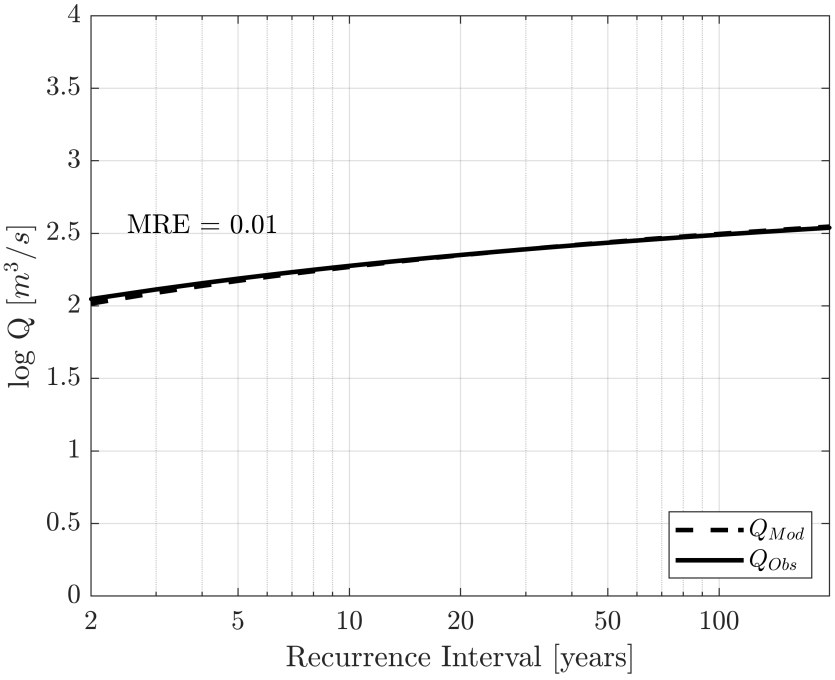

Figure 39: Frequency-Discharge Curves Site #12

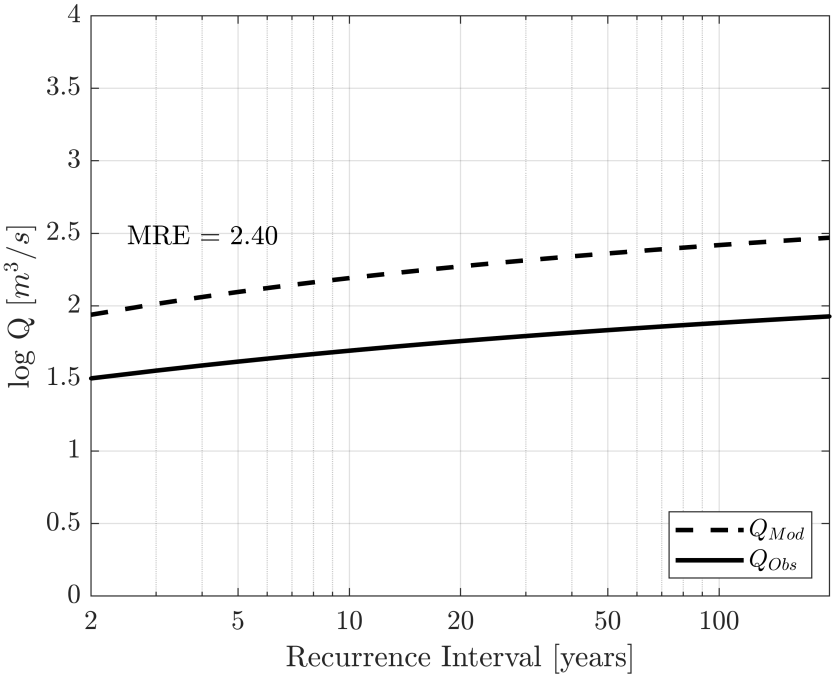

Figure 40: Frequency-Discharge Curves Site #13

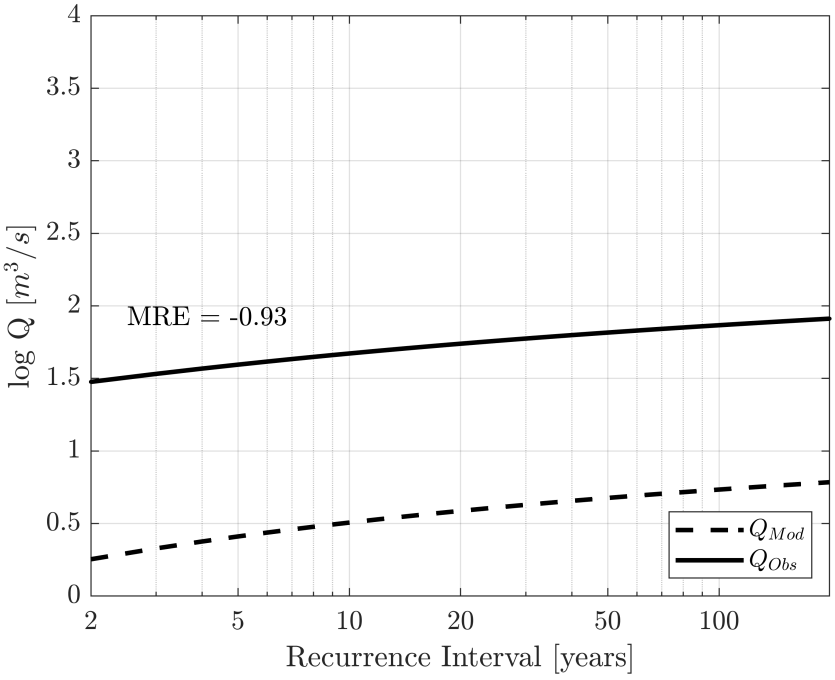

Figure 41: Frequency-Discharge Curves Site #14

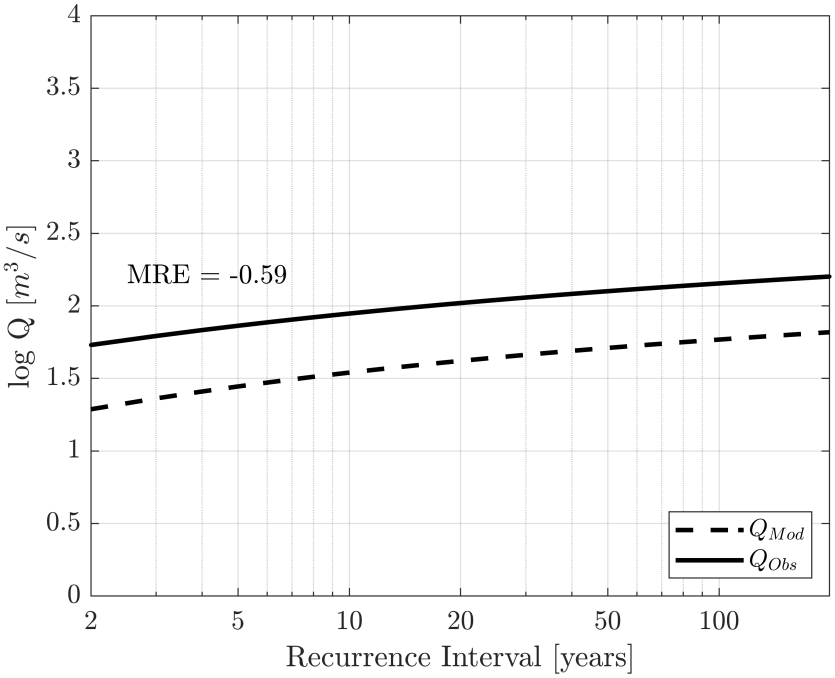

Figure 42: Frequency-Discharge Curves Site #15

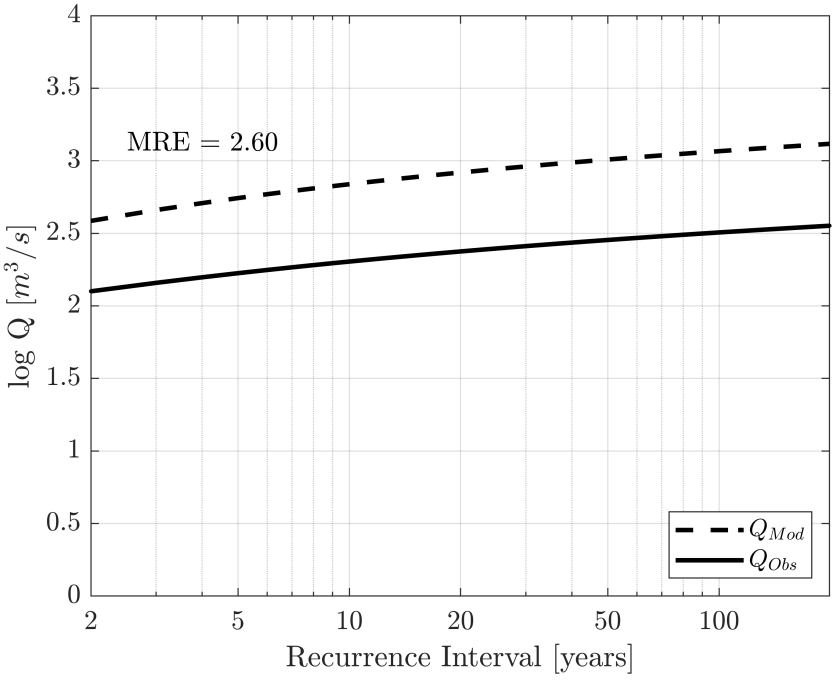

Figure 43: Frequency-Discharge Curves Site #16

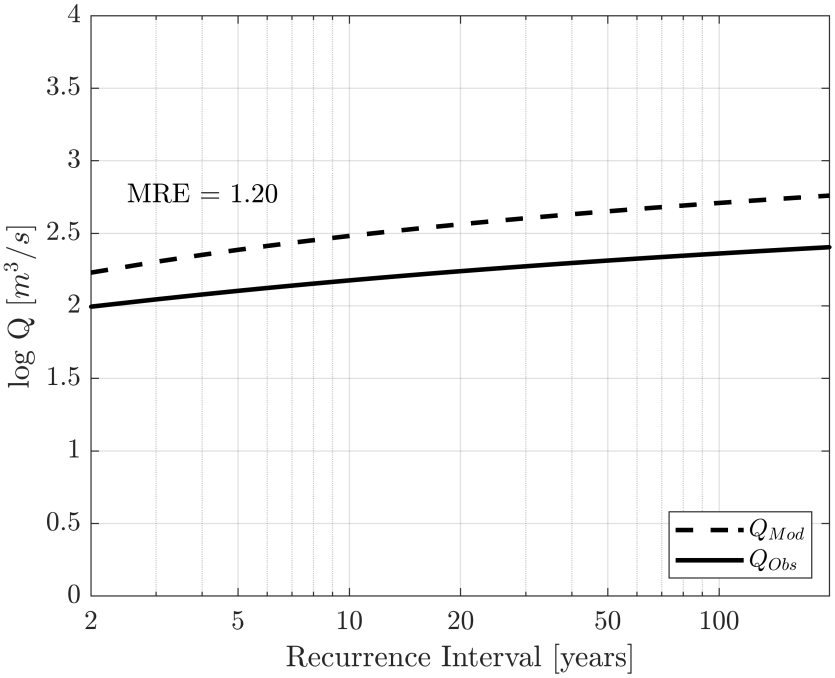

Figure 44: Frequency-Discharge Curves Site #17

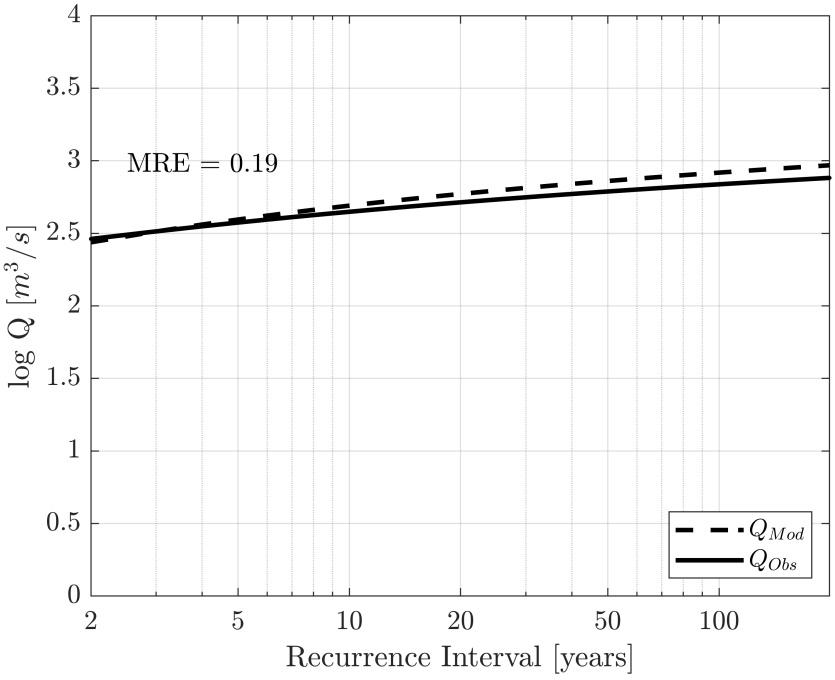

Figure 45: Frequency-Discharge Curves Site #18

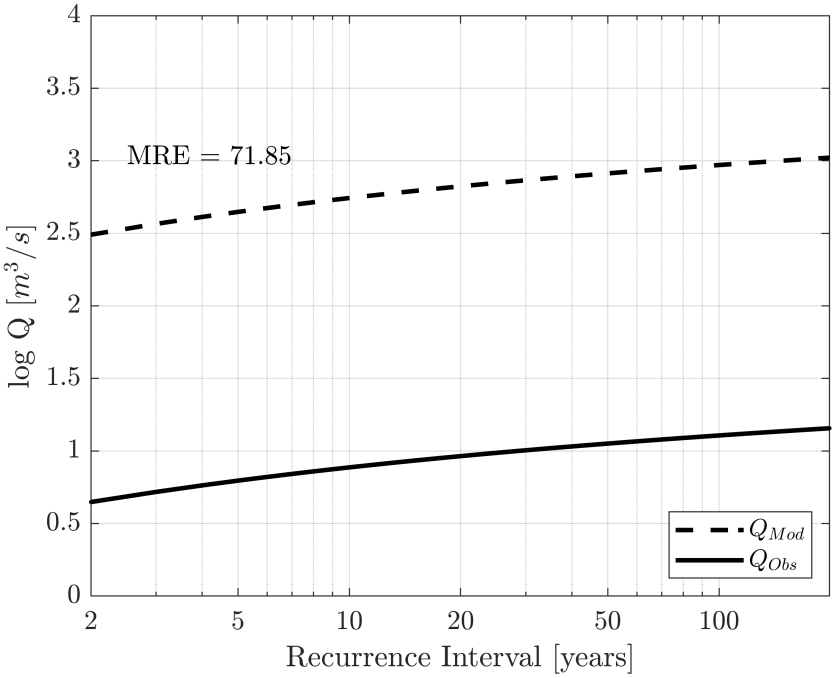

Figure 46: Frequency-Discharge Curves Site #19

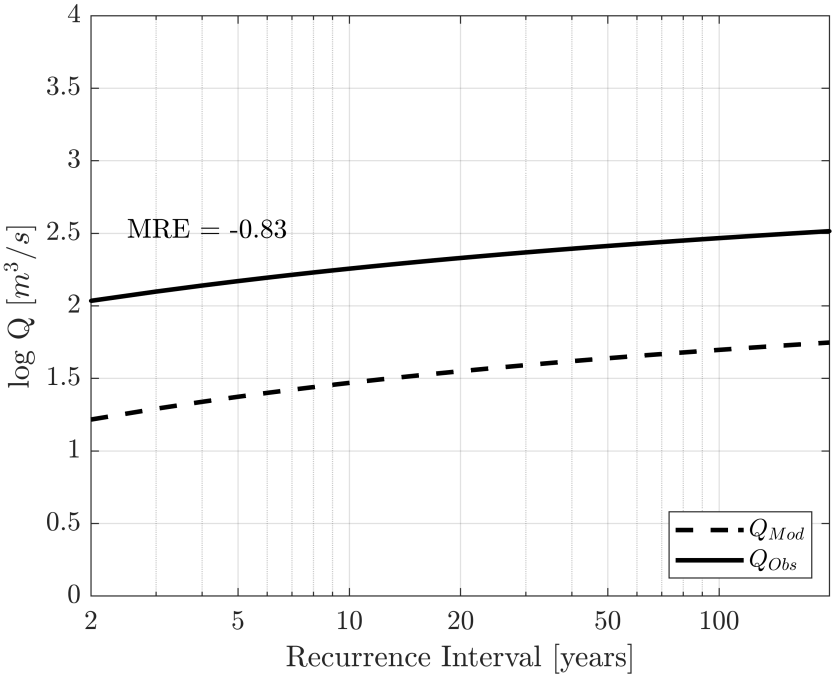

Figure 47: Frequency-Discharge Curves Site #20

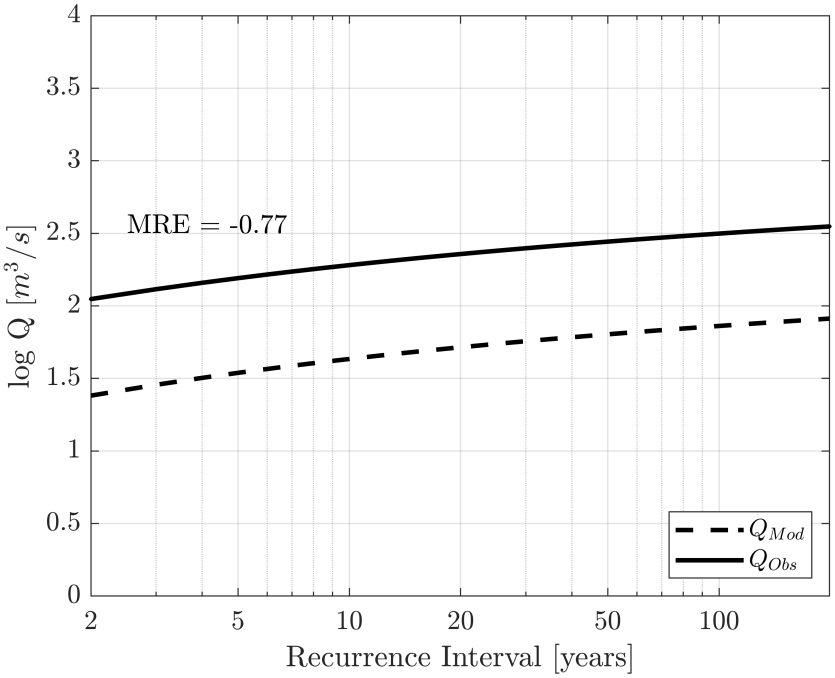

Figure 48: Frequency-Discharge Curves Site #21

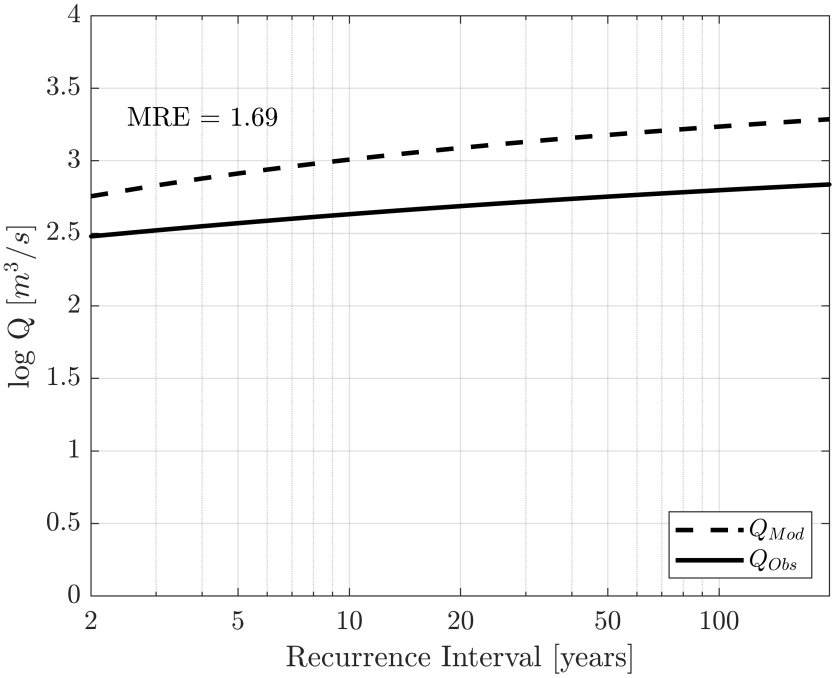

Figure 49: Frequency-Discharge Curves Site #22

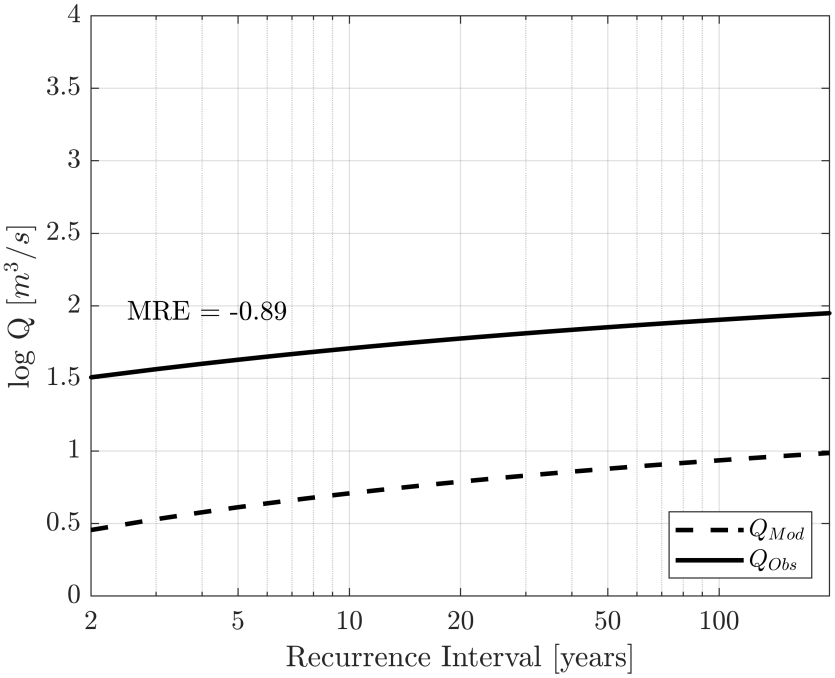

Figure 50: Frequency-Discharge Curves Site #23

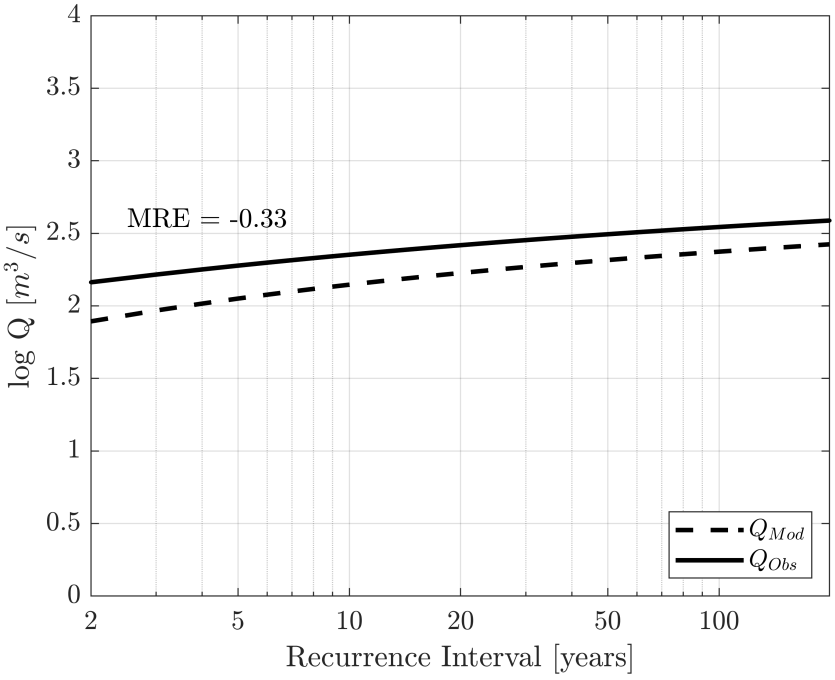

Figure 51: Frequency-Discharge Curves Site #24

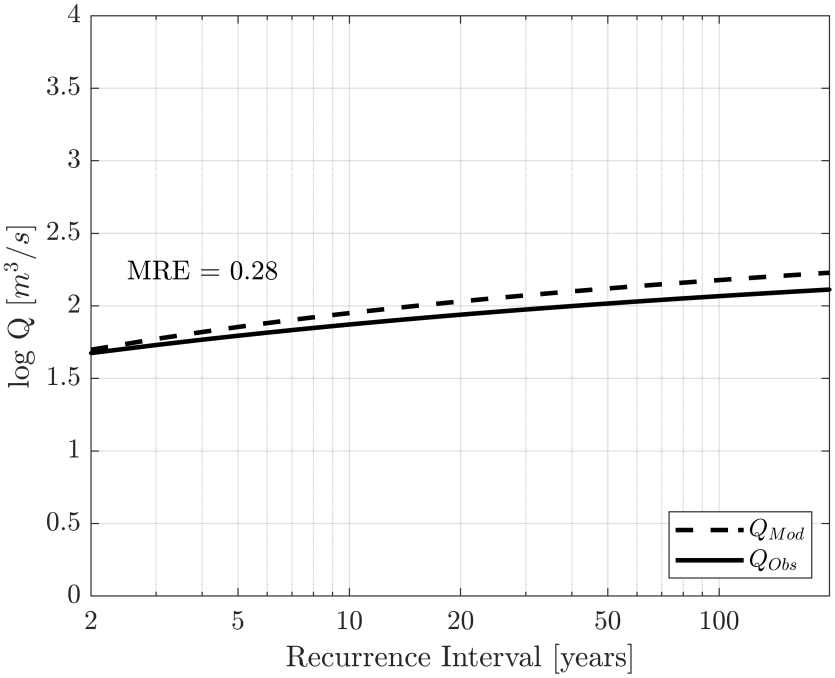

Figure 52: Frequency-Discharge Curves Site #25

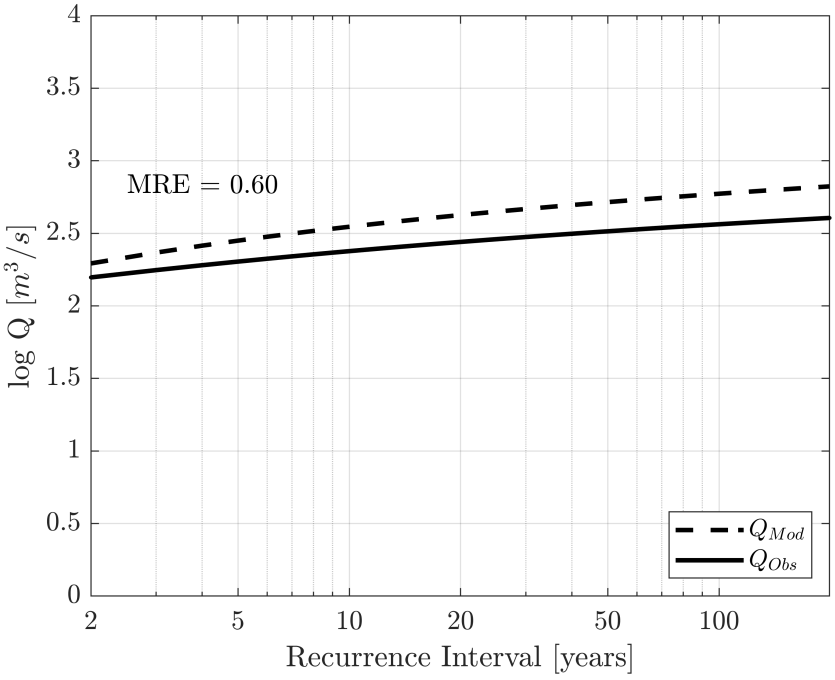

Figure 53: Frequency-Discharge Curves Site #26

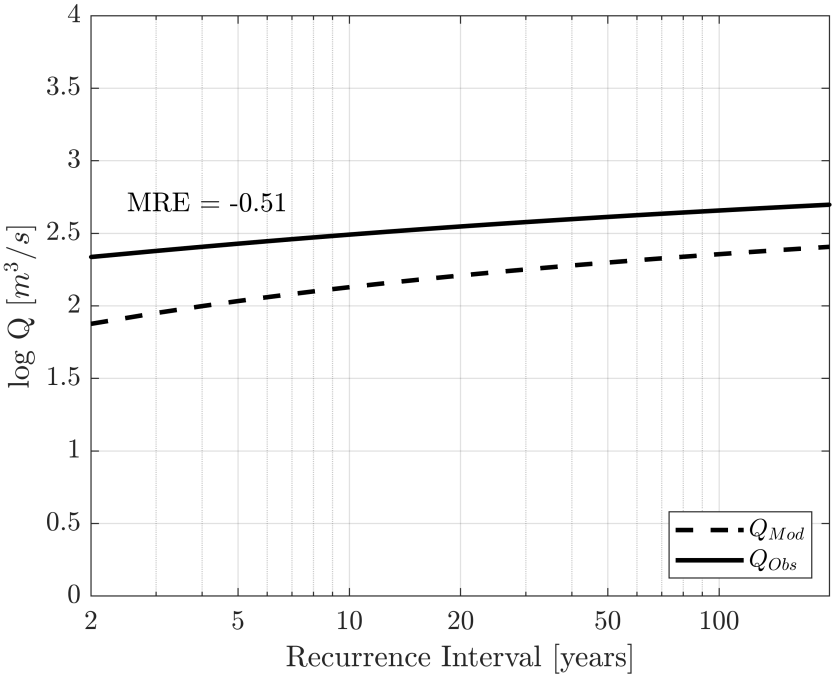

Figure 54: Frequency-Discharge Curves Site #27

References

Bailly, J.-S., Le Coarer, Y., Languille, P., Stigermark, C.-J., and Allouis, T. (2010). Geostatistical estimations of bathymetric LiDAR errors on rivers. *Earth Surface Processes and Landforms*, 35(10):1199–1210.

Beven, K. J. and Beven, K. (2001). *Rainfall-runoff modelling*. Wiley Online Library.

Bhatt, V. and Tiwari, A. (2008). Estimation of peak streamflows through channel geometry/estimation de pics de débit fluviatiles à l'aide de la géométrie des cours d'eau. *Hydrological Sciences Journal*, 53(2):401–408.

Bjerklie, D. M., Moller, D., Smith, L. C., and Dingman, S. L. (2005). Estimating discharge in rivers using remotely sensed hydraulic information. *Journal of Hydrology*, 309(1-4):191–209.

Carling, P. (1988). The concept of dominant discharge applied to two gravel-bed streams in relation to channel stability thresholds. *Earth Surface Processes and Landforms*, 13(4):355–367.

Comiti, F., Mao, L., Wilcox, A., Wohl, E. E., and Lenzi, M. A. (2007). Field-derived relationships for flow velocity and resistance in high-gradient streams. *Journal of Hydrology*, 340(1-2):48–62.

Dade, W. B. and Friend, P. F. (1998). Grain-size, sediment-transport regime, and channel slope in alluvial rivers. *The Journal of Geology*, 106(6):661–676.

Dietrich, W. E. (1982). Settling velocity of natural particles. *Water Resources Research*, 18(6):1615–1626.

Gleason, C. J. and Smith, L. C. (2014). Toward global mapping of river discharge using satellite images and at-many-stations hydraulic geometry. *Proceedings of the National Academy of Sciences*, 111(13):4788–4791.

Gupta, A. and Fox, H. (1974). Effects of high-magnitude floods on channel form: a case study in Maryland Piedmont. *Water Resources Research*, 10(3):499–509.

Hunger, M. and Döll, P. (2007). Value of river discharge data for global-scale hydrological modeling. *Hydrology and Earth System Sciences Discussions*, 4(6):4125–4173.

Huntington, T. G. (2006). Evidence for intensification of the global water cycle: review and synthesis. *Journal of Hydrology*, 319(1):83–95.

Kim, J.-S., Lee, C.-J., Kim, W., and Kim, Y.-J. (2010). Roughness coefficient and its uncertainty in gravel-bed river. *Water Science and Engineering*, 3(2):217–232.

King, T. V., Neilson, B. T., and Rasmussen, M. T. (2018). Estimating discharge in low-order rivers with high-resolution aerial imagery. *Water Resources Research*, 54(2):863–878.

Leopold, L. B. (1994). *A View of the River*. Harvard University Press.

Leopold, L. B. and Maddock, T. (1953). *The hydraulic geometry of stream channels and some physiographic implications*, volume 252. US Government Printing Office.

López, R., Barragán, J., and Colomer, M. À. (2007). Flow resistance equations without explicit estimation of the resistance coefficient for coarse-grained rivers. *Journal of Hydrology*, 338(1-2):113–121.

Manning, R. (1891). On the flow of water in open channels and pipes. *Institute of Civil Eng. Ireland*, 20:161–207.

McCandless, T. L., Annapolis, M., et al. (2003). Maryland stream survey: Bankfull discharge and channel characteristics of streams in the coastal plain hydrologic region. *US Fish and Wildlife Service, Chesapeake Bay Field Office, CBFO-S03-02*.

MD-iMAP (April 2019). Maryland's mapping and gis data portal: Lidar. `https://imap.maryland.gov/Pages/lidar.aspx`. Accessed: February 2019.

Nathanson, M., Kean, J. W., Grabs, T. J., Seibert, J., Laudon, H., and Lyon, S. W. (2012). Modelling rating curves using remotely sensed LiDAR data. *Hydrological Processes*, 26(9):1427–1434.

Olsen, D., Whitaker, A., and Potts, D. F. (1997). Assessing stream channel stability thresholds using flow competence estimates at bankfull stage 1. *JAWRA Journal of the American Water Resources Association*, 33(6):1197–1207.

Paola, C., Parker, G., Seal, R., Sinha, S. K., Southard, J. B., and Wilcock, P. R. (1992). Downstream fining by selective deposition in a laboratory flume. *Science*, 258(5089):1757–1760.

Parker, G. (1978a). Self-formed straight rivers with equilibrium banks and mobile bed. part 1. the sand-silt river. *Journal of Fluid Mechanics*, 89(1):109–125.

Parker, G. (1978b). Self-formed straight rivers with equilibrium banks and mobile bed. Part 2. The gravel river. *Journal of Fluid Mechanics*, 89(1):127–146.

Parker, G. (2004). 1d sediment transport morphodynamics with applications to rivers and turbidity currents. *E-book available from http://vtchl. uiuc. edu/people/parkerg/morphodynamics_e-book. htm (last accessed 23 February 2010)*.

Parker, G., Wilcock, P. R., Paola, C., Dietrich, W. E., and Pitlick, J. (2007). Physical basis for quasi-universal relations describing bankfull hydraulic geometry of single-thread gravel bed rivers. *Journal of Geophysical Research: Earth Surface*, 112(F4).

Pavelsky, T. M. (2014). Using width-based rating curves from spatially discontinuous satellite imagery to monitor river discharge. *Hydrological Processes*, 28(6):3035–3040.

Rhoads, B. L. (1991). A continuously varying parameter model of downstream hydraulic geometry. *Water Resources Research*, 27(8):1865–1872.

Richard, K. (1982). *Rivers: Form and Process in Alluvial Channels*. Metheun, London.

Rossi, F., Fiorentino, M., and Versace, P. (1984). Two-component extreme value distribution for flood frequency analysis. *Water Resources Research*, 20(7):847–856.

Sichangi, A. W., Wang, L., Yang, K., Chen, D., Wang, Z., Li, X., Zhou, J., Liu, W., and Kuria, D. (2016). Estimating continental river basin discharges using multiple remote sensing data sets. *Remote Sensing of Environment*, 179:36–53.

Singh, V. P. (2003). On the theories of hydraulic geometry. *International journal of sediment research*, 18(3):196–218.

Smith, L. C., Isacks, B. L., Bloom, A. L., and Murray, A. B. (1996). Estimation of discharge from three braided rivers using synthetic aperture radar satellite imagery: Potential application to ungaged basins. *Water Resources Research*, 32(7):2021–2034.

Smith, L. C. and Pavelsky, T. M. (2008). Estimation of river discharge, propagation speed, and hydraulic geometry from space: Lena River, Siberia. *Water Resources Research*, 44(3).

Snyder, N. P. (2009). Studying stream morphology with airborne laser elevation data. *Eos, Transactions American Geophysical Union*, 90(6):45–46.

Stahl, K., Tallaksen, L. M., Hannaford, J., and Van Lanen, H. (2012). Filling the white space on maps of european runoff trends: estimates from a multi-model ensemble. *Hydrology and Earth System Sciences*, 16(7):2035–2047.

USGS (April 2019). U.S. Geological Survey Water Data for USA. `https://waterdata.usgs.gov/nwis`. Accessed: February 2019.

Wharton, G. and Tomlinson, J. (1999). Flood discharge estimation from river channel dimensions: results of applications in Java, Burundi, Ghana and Tanzania. *Hydrological Sciences Journal*, 44(1):97–111.

Wobus, C., Whipple, K. X., Kirby, E., Snyder, N., Johnson, J., Spyropolou, K., Crosby, B., Sheehan, D., and Willett, S. (2006). Tectonics from topography: Procedures, promise, and pitfalls. *Special papers-geological society of america*, 398:55.

Wolman, M. G. (1955). *The natural channel of Brandywine creek, Pennsylvania*, volume 271. US Government Printing Office.

Yen, B. C. (1992). *Channel flow resistance: Centennial of Manning's formula*. Water Resources Publication.